A microsecond time-resolved spectroscopic study of laser induced plasmas and their interaction with solid materials

by

Walter F. Casper IV

A dissertation submitted to the Graduate Faculty of
Auburn University
in partial fulfillment of the
requirements for the Degree of
Doctor of Philosophy
Auburn, Alabama

August 1, 2015

[Laser induced plasmas, energetic materials, optical emission spectroscopy]

Copyright 2015 by Walter F. Casper IV

Approved by

Rik Blumenthal, Chair, Associate Professor, Department of Chemistry
Vincenzo Cammarata, Associate Professor, Department of Chemistry
German Mills, Professor, Department of Chemistry
Konrad Patkowski, Assistant Professor, Department of Chemistry

Abstract

Photon-material interactions are driven by fast chemical and physical phenomena. With enough incident energy, photons are capable of inducing photoionization processes converting the solid material to a plasma. The highly energetic resulting electrons and ionic species undergo rapid transformation with the underlying material and themselves in the nano-second to micro-second time scale before the decay back to a gaseous state occurs. These actions drive the many interesting interactions that take place in a laser induced plasma event. Study of the plasma emission can give insight into the mechanisms of interaction, and the resulting samples after irradiation can provide information on how the plasma formed.

Chapter 1 gives an overview of the current state of energetics materials with a history of the current methods and techniques of initiation and testing. The fundamental operation of lasers is discussed, along with their interaction mechanisms with materials. An overview of the resulting analytical techniques to study laser induced plasmas is given.

Chapter 2 discusses the experimental processes employed during each experiment. A description of sample preparation is given. The design and construction of the driving electronics, optical set-up, and spectroscopy are detailed. The custom programming for data collection and analysis is discussed.

Chapter 3 discusses the time-resolved spectroscopic study of the laser induced plasma and the decay process that was evident from the resulting spectra. The plasma decay process as observed is believed to be that of a phase transition from a plasma to a gaseous state.

Chapter 4 details the mechanisms of material removal from the molecular solid RDX. Experiments were done at various lens to sample distances to understand how the fluence influenced the plasma plume formation. The results are interpreted in terms of four different mechanisms of material removal dependent upon the laser fluence.

Chapter 5 is a study of the laser ablation of polycarbonate covered RDX samples. The mechanisms and amounts of material removal in PC and RDX differ at constant laser fluence. However, when coating the RDX samples in PC, the increase in depth of material removal is 8x that of RDX alone. These results suggested that the mechanism of removal involves a chemical process driven by the PC laser induced plasma interaction with the underlying RDX material.

Chapter 6 gives an overview of the cumulative understanding of the laser induced plasma plume formation process as related to these studies. There are fundamental processes that are unique to these laser material interactions and they are discussed. Suggested future work is outlined.

Acknowledgments

First and foremost, I must express my complete gratitude to my advisor, Dr. Rik Blumenthal. His guidance, ideas, ingenuity, and direction are the reasons I was able to complete this work. He not only was a great example of a scientist, but taught me how to think and solve problems. Many thanks are also given to my committee members: Dr. Vincenzo Cammarata, Dr. German Mills, and Dr. Konrad Patkowski, for their comments and suggestions throughout my tenure as a student and in preparation of this manuscript. Thank you to my outside reader, Dr. Hulya Kirkici, for her participation in review of this work and examination. Thank you to all of the staff in the Chemistry Department for help on a daily basis. To my fellow graduate students, thank you for support with my work and the friendships I have made. Thank you to Drs. Harold Zallen and Eugenia Malone for generous contribution through the Malone – Zallen Fellowship that I was awarded 2012 and helped fund these projects.

Most significantly, thank you to my wife, Nina. She has been my biggest supporter, my best friend, and a constant blessing. Her support and dedication allowed me to complete this journey in life and I am beyond thankful to have her by my side. Throughout my childhood my mom served as the best example of what it meant to be selfless, strong, and giving. Her legacy shaped the person I am today. My family instilled values of hard work, integrity, and perseverance in me at a young age. Those contributions helped form the drive I have had throughout my life and education. And, my dog Chester, he always extended his positive attitude, companionship, and constantly reminded me to be play, be happy, and have fun.

Table of Contents

Abstract ii

Acknowledgments iv

List of Tables x

List of Figures xi

List of Abbreviations xv

Chapter 1 Introduction 1

1.1 Energetic Materials 1

1.1.1 Historical development 1

1.1.2 Classification of explosives 2

1.1.3 Ignition techniques and ETC 4

1.1.4 Standoff detection 6

1.2 Lasers 6

1.2.1 Fundamental operation 6

1.2.2 Laser beam profile and fluence 10

1.3 Laser interactions with materials 12

1.3.1 Processes of ablation and observation of threshold fluences 12

1.3.2 Fluence dependence on plasma 15

1.4 Lasers as an analytical technique 17

1.4.1 The emission spectrum 17

1.4.2 Spectroscopy instrumentation 17
1.4.3 Collection optics 19
1.4.4 Spectrum analysis 21
1.4.5 Lasers for use with explosive ignition 23
1.6 References 25
Chapter 2 Experimental Design 36
2.1 Wafer translation 36
2.2 Experimental programming 38
2.3 Sample preparation 38
2.3.1Drop cast films 38
2.3.2 Spray deposition 39
2.3.3 Spin coating 41
2.4 RDX analysis 42
2.5 Laser pulse control 44
2.6 Fast-switching spectrometer 46
2.7 Instrument calibration 50
2.8 Photodiode plasma lifetime experiments 57
2.9 Plasma emission spectra collection 57
2.10 Data processing 63
2.11 References 64
Chapter 3 Spectroscopic study of UV laser induced plasma decay 66
3.1 Introduction 66
3.1.1 Laser induced plasma formation 66

3.1.2 Plasma decay process 68
3.2 Experimental 68
3.2.1 Sample preparation 68
3.2.2 Spectroscopy 68
3.2.3 Photographic imaging of plasma plumes 69
3.3 Results and Discussion 70
3.3.1 Spectra analysis 70
3.3.2 Polycarbonate spectra 71
3.3.3 Ammonium nitrate spectra 73
3.3.4 Polyethylene spectra 74
3.3.5 Sucrose spectra 76
3.3.6 Continuum radiation 77
3.3.7 Blackbody radiation model 79
3.3.8 Plasma density 82
3.3.9 Decay in plasma shape 83
3.4 Conclusion 86
3.5 References 88
Chapter 4 Mechanisms of material removal from a molecular solid as a function of lens to sample distance 92
4.1 Introduction 92
4.1.1 Lasers as a scientific tool 92
4.1.2 Laser interaction with materials 93
4.2 Experimental 95

4.2.1 Sample preparation 95
4.2.2 Sample translation 96
4.2.3 Spectroscopy 97
4.2.4 Experimental timing 97
4.3 Results 100
4.3.1 Ablated film images and still frame evidence from videos 100
4.4 Discussion 104
4.4.1 Images of laser paper 104
4.4.2 Polycarbonate results 104
4.4.3 Polyethylene results 106
4.4.4 RDX results 108
4.5 Conclusion 112
4.6 References 113
Chapter 5 Laser ablation of polycarbonate covered thin films of RDX 116
5.1 Introduction 116
5.1.1 Energetic materials ignition 116
5.1.2 Laser ablation 117
5.2 Experimental 122
5.2.1 Sample preparation 122
5.2.2 Thin film diagnostics 125
5.2.3 Instrumentation 127
5.3 Results 128
5.3.1 Optical images of wafers after laser ablation 128

5.3.2 Mass loss from laser ablation 130
5.3.3 3D laser scanning microscopy 131
5.4 Discussion 133
5.4.1 Primary material loss mechanisms 133
5.4.2 Secondary material loss mechanisms 135
5.4.3 Non-energetic sucrose samples 139
5.5 Conclusion 141
5.6 References 142
Chapter 6 Summary and Conclusions 146
6.1 A more complete understanding of the laser induced plasma plume expansion process 146
6.2 Optically dense plasma phase transition 150
6.3 Fluence dependent material removal 151
6.4 Using laser induced plasmas as an energetic material initiation source 151
6.5 Conclusions 152
6.6 Future work 152
6.7 References 154
Appendix 1 155

List of Tables

Table 5.1 Material removed as a function of mass loss 130

Table 5.2 Plasma composition 148

List of Figures

Figure 1.1 Molecular structure of RDX 2

Figure 1.2 Schematic of conventional and ETC ignition 5

Figure 1.3 Schematic of Nd:YAG laser head 8

Figure 1.4 Schematic of 4-level laser system 9

Figure 1.5 Fluence dependence and beam diameter 11

Figure 1.6 Multiphoton excitation process 14

Figure 1.7 Influence of laser pulse on plasma heating 16

Figure 1.8 Design of diffraction based grating spectrometer 18

Figure 1.9 Diagram of ball lens 20

Figure 1.10 Diagram of fiber optic cable 20

Figure 1.11 Laser induced breakdown spectrometer 22

Figure 1.12 Laser induced plasma ignition 24

Figure 2.1Sample holder 37

Figure 2.2 Experimental set up of large area nebulizing spray deposition 40

Figure 2.3 Image measuring thickness of RDX on glass 42

Figure 2.4 Optical microscopy images of porosity of RDX deposition 43

Figure 2.5 Laser power measurements 45

Figure 2.6 Schematic of image intensifier 48

Figure 2.7 Circuit designed for driving electronics of detector 49

Figure 2.8 Oscilloscope trace of 300 to 0V switching on 1μs 50
Figure 2.9 Image intensifier turn on/off response 51
Figure 2.10 Linearity of detector response 52
Figure 2.11 Calibration lamps on detector 54
Figure 2.12 Wavelength calibration curve 55
Figure 2.13 Intensity calibration of detector 56
Figure 2.14 Experimental set up 59
Figure 2.15 Timing scheme 62
Figure 3.1 Plasma plume expansion schematic 67
Figure 3.2 Plasma ablation process 70
Figure 3.3 Polycarbonate spectra over time 72
Figure 3.4 Ammonium nitrate spectra over time 73
Figure 3.5 Polyethylene spectra over time 75
Figure 3.6 Sucrose spectra over time 76
Figure 3.7 Still frame images from video of plasma plume 77
Figure 3.8 Blackbody fit of polycarbonate spectra 79
Figure 3.9 Linear plot of polycarbonate spectra 81
Figure 3.10 Normalized polycarbonate spectra 84
Figure 3.11 Normalized ammonium nitrate spectra 84
Figure 3.12 Normalized polyethylene spectra 85
Figure 3.13 Normalized sucrose spectra 85
Figure 3.14 Schematic of optically dense plasma phase transition 87
Figure 4.1 Wafer layout 96

Figure 4.2 Experimental set up 98
Figure 4.3 Timing scheme 99
Figure 4.4 Images of samples after laser irradiation at various LSD 101
Figure 4.5 Ablation area as a function of LSD 102
Figure 4.6 Evolution of plasma formation at various LSD 103
Figure 4.7 Spectroscopic evidence for polyethylene 107
Figure 4.8 3D laser scanning microscopy of RDX 109
Figure 4.9 Spectroscopic evidence for RDX 110
Figure 5.1 Time delay comparison of ETC to traditional methods 117
Figure 5.2 Model of laser ablation 119
Figure 5.3 Laser induced plasma plume images 121
Figure 5.4 Nebulizing spraying technique 123
Figure 5.5 Prepared samples of RDX thin films 124
Figure 5.6 Spin coated polycarbonate on RDX 124
Figure 5.7 Optical microscopy of RDX films 125
Figure 5.8 Photograph showing RDX film thickness 126
Figure 5.9 Samples before and after laser irradiation 129
Figure 5.10 Microscope images of ablation pits 129
Figure 5.11 3D Laser scanning microscope images of PC, RDX, and PC/RDX 132
Figure 5.12 Detailed 3D images of PC/RDX pit 133
Figure 5.13 Pit geometry between RDX and PC/RDX pits 134
Figure 5.14 Sublimation contribution due to plume radiation 136
Figure 5.15 Sublimation estimate over wafer surface 137

Figure 6.1 LIP expansion timeline 146

Figure 6.2 Vaporized material expansion in LIP 147

Figure 6.3 Shockwave formation 148

Figure 6.4 Laser induced plasma heating 149

Figure 6.5 Plasma heating and expansion 149

Figure 6.6 Propagation of LIP 161

List of Abbreviations

AN	Ammonium Nitrate
CCD	Charge coupled device
DC	Direct current
EM	Energetic material
ETC	Electrothermal Chemical Ignition
FG	Function generator
HE	High Explosive
HMX	Octahydro-1,3,5,7-tetranitro-1,3,5,7-tetrazocine or High-velocity Military eXplosive
II	Image Intensifier
IR	Infrared
LASER	Light Amplification by Stimulated Emission of Radiation
LE	Low Explosive
LIBS	Laser Induced Breakdown Spectroscopy
LIP	Laser induced plasma
LSD	Lens to Sample Distance
MCP	Microchannel plate
Nd:YAG	Neodymium-doped yttrium aluminum garnet
OES	Optical Emission Spectrometer
PFN	Pulse forming network

PC	Polycarbonate
PC/RDX	Polycarbonate coated RDX
PE	Polyethylene
PP	Polypropylene
RDX	Cyclotrimethylenetrinitramine or Research Department Formula X
SEM	Scanning Electron Microscopy
TNT	Trinitrotoluene
UV	Ultraviolet
VIS	Visible

Chapter 1

Introduction

1.1 Energetic materials

1.1.1 Historical development

An explosive is a chemical compound which has the potential to release large amounts of heat and/or pressure upon initiation of decomposition.[1, 2] The Chinese first developed gun powder, a formulation of sulfur, charcoal, and potassium nitrate, in the 9th century during the Tang dynasty. It would be hundreds of years until the next significant advance in explosives was made. First synthesized by Ascanio Sobrero in 1847, nitroglycerin was not brought to its full potential until 1867 when Alfred Nobel figured out how to stabilize it, producing dynamite a few years later with its commercial production.[3] The production was dangerous, and the blasting oil mixture of nitroglycerin and black powder was unstable. Eventually the nitroglycerin was made safe by Nobel through the mixture of nitroglycerin with clay like material that stabilized it. This is the first example of the importance of stabilizing energetic materials (EMs) and to this day the balance between safety[4] and performance is an issue, and the end product was known as a formulation. More formulations were made in the coming years to improve this balance but it was not until World War I that trinitrotoluene (TNT) was developed. World War II saw the advent of even more powerful and common explosives such as cyclotrimethylenetrinitramine (RDX) (Figure 1.1) and octahydro-1,3,5,7-tetranitro-1,3,5,7-tetrazocine (HMX).

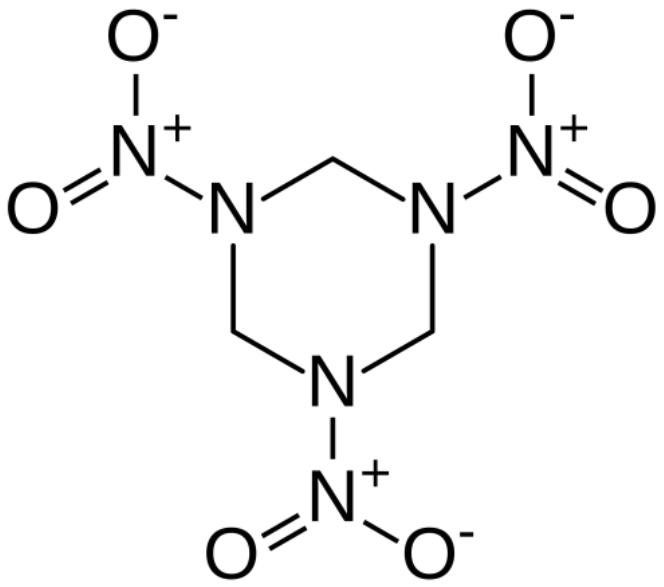

Figure 1.1. Cyclotrimethylenetrinitramine (RDX)

The explosives discovered and used during this era were the most powerful and many are still used in various formulations today. Since then the most notable contributions have been the discovery of HMX, PETN, and CL-20.[5] However most modern day explosives still use those already discovered in certain combination with one another and stabilizing materials.

1.1.2 Classification of explosives

The need for new explosives is still great[6, 7] and much work is going into the synthesis and discovery of new materials. But with every explosive there is a need for classification based upon its performance and ultimate use. The classification of these chemicals as explosives is divided first into high explosives (HEs) and low explosives (LEs). A chemical compound is classified as a HE when the chemical reaction front moves faster than the speed of sound. Conversely, the LE combustion is subsonic. Supersonic combustion in HEs, known as detonation, also results in a significant pressure gradient in the form of a shock wave.[8, 9] The LE

combustion is known as deflagration, a burning process without the associated high pressure shock waves.

Within the high explosive category there are also further classifications based on sensitivity: primary, secondary, and tertiary[10] explosives which are classified based on the amount of energy required to detonate it. Primary explosives require very little energy to initiate and are quite sensitive to heat, friction, impact, and pressure.[11] Primary explosives such as black powder or lead azide are often used to then initiate secondary explosives due to their extreme sensitivity. The secondary explosives such as RDX or TNT are much more powerful than primary explosives.[12, 13] Secondary explosives however are quite stable and require a large amount of energy to initiate which is why they must be used with a form of a detonator. Tertiary explosives such as ammonium nitrate (AN)[10] or various bulk explosives used in mining are even more stable than secondary explosives. They are cheap to produce and their stability is important for the safety considerations as used in their practical blasting applications. The initiation of all explosives is of great concern; the goal is to provide the best balance of performance and safety in any given application.

The behavior of explosives on a large scale[14] is rooted in their molecular structure.[15, 16] Therefore, during the design of new explosives[17, 18] great care must be taken to understand their application and whether they will be used for deflagration such as in flares, or a large detonation front for military use are significant factors. In order to define the use, much must be known about the performance. It is easier, cheaper, and safer to test these on a small scale when their characteristics are unknown. Currently, there is great interest in the development of small-scale testing of already synthesized compounds that hold promise as new explosives but whose properties are not well known. This area of research is ever growing as the search for a reliable

and safe testing technique that can easily scan and identify promising compounds is important. A lot of progress has been made in benchtop energetics experiments[2, 19-21] by inducing small shock waves from laser driven flyer plates.[22-29] Additionally, new methods aim at investigating laser beam interactions with explosives to determine their performance based upon expanding shock waves[30, 31] imaged with high-speed photography.[32-35]

1.1.3 Ignition techniques and ETC

In a typical artillery shell, the bulk of the main charge is a secondary explosive such as RDX or some combination or formulation of stabilizers, plasticizers, metal particulate, or other explosives.[36] Since the secondary explosive is relatively stable, it needs to be brought to the point of detonation by introduction of enough energy. Historically, primary explosives, since they are sensitive, have been used for this application. But this higher sensitivity increase safety concerns. Other options include various electrical detonators, blasting caps, and igniters. One form of ignition that has been pursued as a safe and reliable form is electrothermal chemical ignition (ETC) which is depicted in Figure 1.2.[37-40] This uses the capacitive discharge of a polymer to create a high energy plasma and a gaseous burst that, upon contacting the secondary explosive, ignites it.[41, 42]

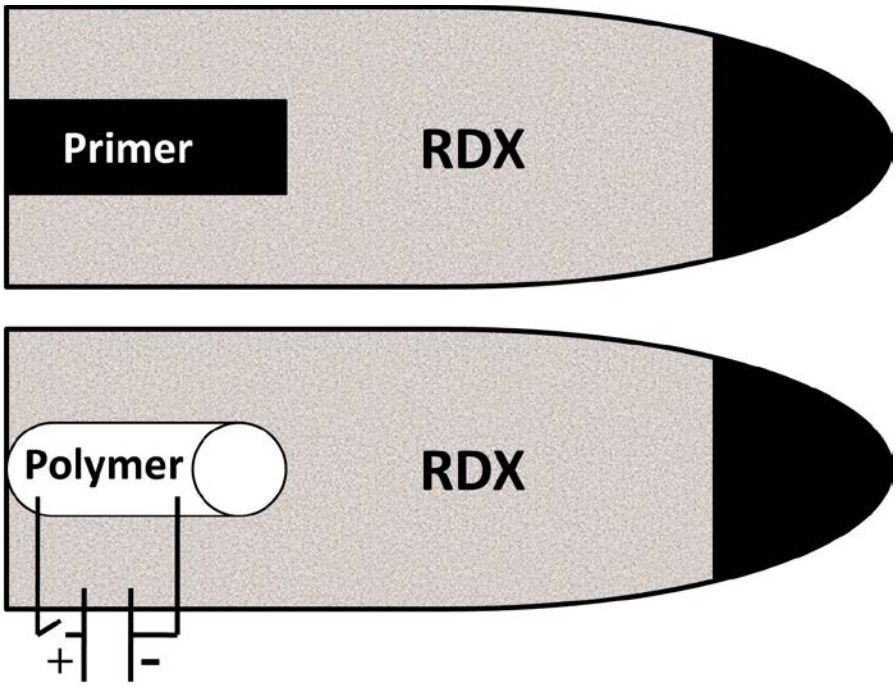

Figure 1.2. Conventional (top) and ETC (bottom) ignition

The advantage of this method is that it removes the unstable primary explosive from the equation by replacing it with an inert material. Unfortunately the practical concern then becomes the need for and size of a power supply to convert this polymer to a plasma and the large capacitor to generate the current.

ETC ignition of energetic materials has been well studied.[41, 43, 44] It has been shown that the initiation time in ETC is extremely reproducible on a microsecond time scale as compared to the millisecond irreproducibility of conventional methods.[45] Experimental modeling studies have identified hydrogen as the species responsible for the chemical interaction between plasma and propellant. *Blumenthal et. al.*[46] has shown that the hydrogen ion implantation into the energetic material is responsible for the initiation of the chemical processes leading to detonation through a process related to the HONO thermal decomposition mechanism. Therefore, an important aspect is to have a source of hydrogen ions for implantation in the EM.[47]

Additionally, it has been shown that lasers, when incident upon polymers, can also form plasmas.[48-52] This laser ignition of explosives has been investigated as an alternative form of ignition for a long time.[53] It could serve as a promising and safe alternative to traditional methods by replacing the sensitive igniters with an inert material and using the advantages of ETC but without the need for a large capacitor. In this design, an embedded polymer could be selectively irradiated with the laser pulse to ignite the explosive directly.[54]

1.1.4 Standoff detection

Dissimilarly, instead of using lasers to ignite the explosive as described, Laser induced breakdown spectroscopy (LIBS) can be used as a standoff detection method for explosives. This analytical technique ablates the explosive or residue to obtain emission spectra that can then identify the chemical compound present. The technique is advantageous due to its purely optical nature and the ability to identify the specific type of explosive even at a faraway distance. [55-57] In the energetic materials community there are large areas devoted to the safe creation and optimization of explosives, but there is also a large field devoted to the detection and identification of explosives.[58, 59]

1.2 Lasers

1.2.1 Fundamental operation

The acronym LASER comes from **l**ight **a**mplification by **s**timulated **e**mission of **r**adiation. The fundamental operation centers on a few main parts depicted in Figure 1.3. Contained inside of an enclosed cavity is the crystal, the determining factor of wavelength of emission. The lasing medium typically emits light somewhere in the ultraviolet (UV), visible (VIS) or infrared (IR). The work described herein uses a neodymium-doped yttrium aluminum garnet (Nd:YAG) laser upon which this description will be focused. A rod of a Nd:YAG crystals

is placed between two powerful bulbs known as flash lamps that emit white light. These lamps are driven by a high DC voltage. The crystal rod absorbs this light exciting the atoms. In a simple example of stimulated emission, when an atom is excited to a higher energy state, there is a related decay to a lower state releasing a photon. In order for lasing to occur, more photons have to be emitted than attenuated in the medium, and the rate of emission must be greater than that of the absorption. In a simple two level system, thermal equilibrium dictates that there will be more atoms lying in the ground state than the excited, so a stimulated emission cannot be achieved for use in a laser. Most systems are therefore 4-level lasers as the efficiency of emission is greater in this case. The process is depicted in Figure 1.4 where the excited states lie significantly higher than the ground state. The relaxation therefore does not occur directly back to the ground state but first to a metastable state through a fast non-radiative transition. It is from this high metastable state that a relaxation occurs to a lower metastable state, with emission of a photon. This separation between two states due to the intersystem crossing is what allows a population inversion, and thus lasing, to occur. From the low metastable state, further slow relaxation occurs back to the ground state. The four electronic levels and the two steps of non-radiative transition allow a population inversion to be achieved. Once a population inversion has been reached, the crystal rod emits photons at a wavelength of 1064 nm. This 1064 nm light resonates back and forth around the laser head cavity which has mirrors to focus the light in one direction toward the output. When a high enough amount of energy is present, the pockels cell, which acts like a fast electronic shutter, is opened. This is known as q-switching, which allows high-energy, short pulses to be created. The 1064 nm light exits the laser head to (to the left) where it then travels through pulse shaping, harmonic optics. These specialized optics have the ability to frequency double the photons so that the 1064 nm photons are generated with twice the energy at 532 nm.

This process can happen more than once generating photons at 266 nm also. To achieve high energy UV photons, Nd:YAG lasers are often operated in a pulsed mode which is operated by the use of a q-switch. In this set-up, the light resonates through the cavity and is only allowed to exit once a threshold amount of energy is achieved. Once that energy is achieved, the q-switch lets a pulse of light out for a short duration, typically in the nano-second time scale. This pulse of light is then focused to a point at some distance away from the laser head.

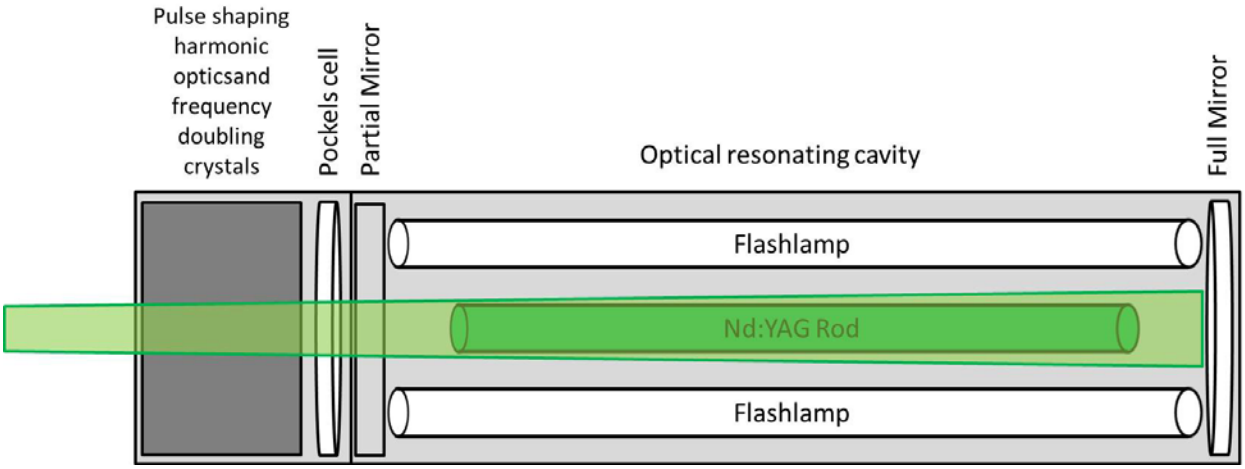

Figure 1.3. Simplified schematic diagram of a Nd:YAG laser head

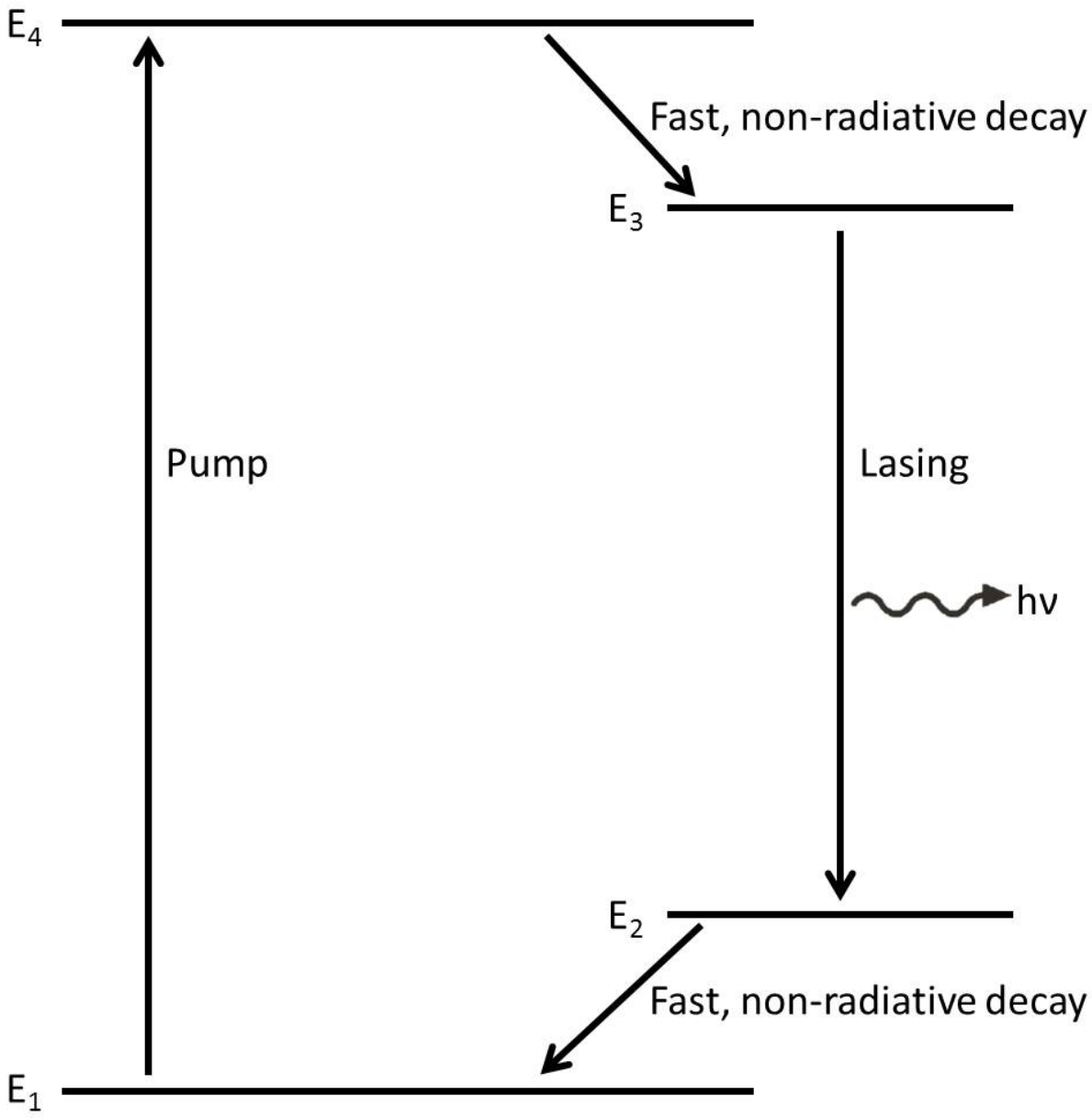

Figure 1.4. Schematic of 4 – level laser system that allows population inversion to occur

1.2.2 Laser beam profile and fluence

Laser fluence is described as the energy delivered over an area per unit time. In a 266 nm Nd:YAG nano-second laser, fluences can reach values of tens to hundreds of millijoules per pulse. So there is a delivery of a pulse of photons with given energy over the surface of a material for the few nanoseconds of the laser pulse. The unfocused light exiting the laser head is a beam that can be a few millimeters in diameter that is related to the diameter of the rods. But the energy distribution through the width of light exiting the laser is usually not linear, but in most cases considered to exhibit a Gaussian distribution. The irradiance distribution of the beam is defined by the optics in the pulse forming network (PFN). Most commonly there is a Gaussian distribution that exits the head in a large diameter beam and then is focused to an appropriate spot size ahead of the sample or behind by the lens as shown in Figure 1.5.

The Gaussian beam is focused to a point which is determined by the focal length of the lens. The sample is situated at some point along the path of the beam typically between the lens and the focal point of the lens. This distance, known as the lens to sample distance (LSD) along with the unfocused beam diameter defines the spot size of the laser beam. Depending on how close or far away the sample is placed from the lens; the spot size will be either large or small respectively. Within this large or small spot size then, the density of energy will be either smaller or greater because the energy is being deposited over a larger or smaller area. The fluence is therefore defined as the power density incident upon the material:

$$Fluence = \frac{energy}{area} \text{ (J/cm}^2\text{/s)} \qquad (1.1)$$

This then is how the laser fluence is adjusted, by changing the lens to sample distance, adjusting the spot size which changes the energy per area, the fluence.

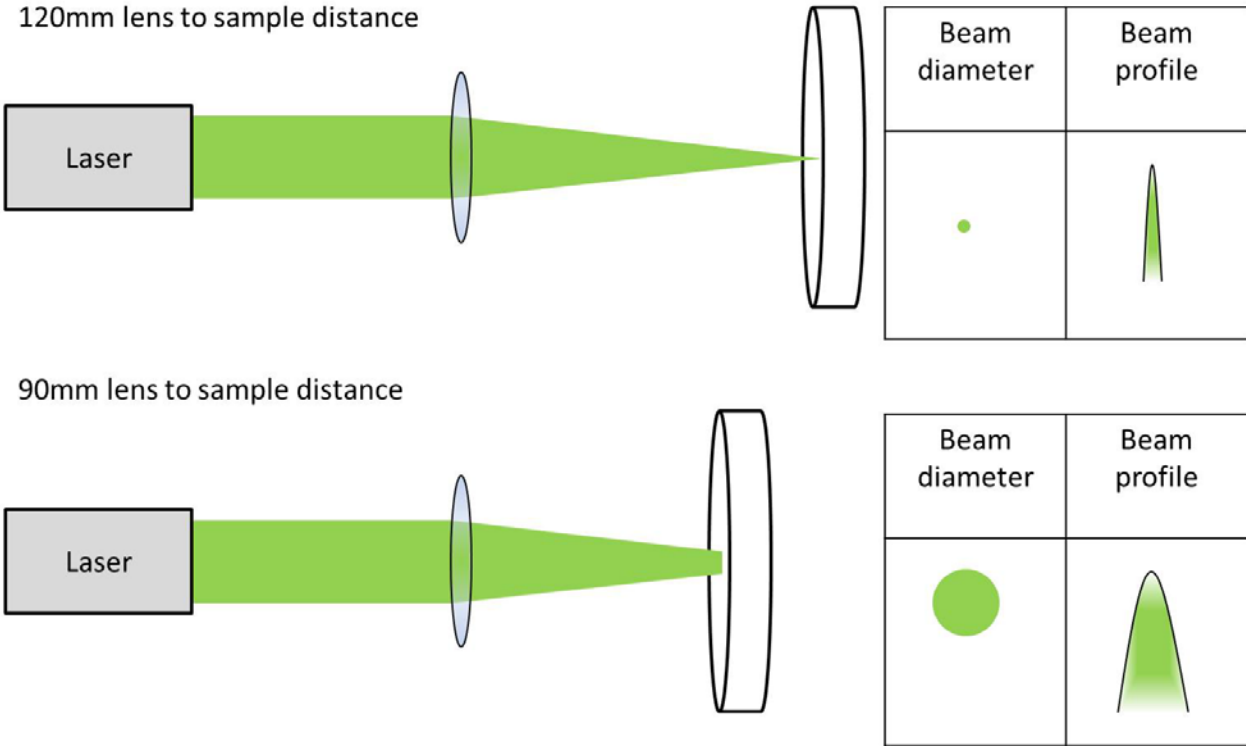

Figure 1.5. Fluence dependence on focused beam diameter, and the energy distribution throughout the beam profile

1.3 Laser interactions with materials

1.3.1 Processes of ablation and observation of threshold fluences

The laser pulse interaction with a material depends most strongly upon the absorption coefficient of the given material.[60, 61] For example, a UV laser pulse will pass through a quartz lens due to the transmission properties of the SiO_2 lattice. A UV laser pulse impinging on a metal however will not pass through. Instead the UV laser light will excite the electrons in the metal to a higher state through direct absorption. If the energy of the UV photons are higher than the binding energy of the electrons then the metal will be photo-ionized. If an IR laser beam interacts with quartz, again the beam would transmit through. But, in the case of the metal, the IR beam will not act through a photoionization process because the energy per photon is smaller. The IR laser ablation process thus takes place through an interaction with the molecular vibrations resulting in an increase in temperature, rapid thermal heating forming an electron gas, followed by generation of an ionized plasma state.[62] This linear absorption process is a difference between the multi-photon UV interactions.[63-65] Here, the infrared laser wavelength must be in resonance with the molecular bonds present in the material in order for ablation to occur. And the energy of those photons must be able to transmit enough energy to those bonds resulting in a significant increase in motion causing a rapid heating in a short amount of time. This makes the ablation threshold subject to the absorption and thermal characteristics of the material. UV laser pulses however interact through an electronic process. The UV photons are of significant enough energy to be greater than most all atomic bonds. Therefore, the energy deposited depends not on the resonance of the bonds or their strength in thermal characteristics. Metals have allowed states to which an electron can be promoted to, insulators do not. The work described throughout was done with a UV laser so that interaction will be described in detail.

Intense UV laser light interacting with an insulating or semiconducting material is directly absorbed through a multi-photon ionization process as depicted in Figure 1.6.[66, 67] In the absence of allowed unoccupied states, when $E = E_{occupied} + h\upsilon$, there are only higher order interactions that explain the absorption of light. The multi-photon nature of the UV process defines the absorption mechanism as non-linear or second order, unlike the IR process previously described. With an incident UV photon of enough energy, an electron will be promoted to a virtual state. If another photon is incident before the decay time, this electron is promoted to a continuum of states. If the second photon is absorbed after the decay, relaxation will occur. This sets a threshold to ablation that is based upon the number of photons interacting with the material in a given area at a certain time, not the thermal properties of the material.

If the photon flux is greater than the threshold to ablation, the laser irradiation creates ions and free electrons, along with neutral species in a plasma once the promotion to a continuum of states has been established. At some electron density, once the plasma formation has been established, it becomes optically thick in that the outer skin is not transparent to the hotter inner core. The ionization is a second order process but the heating however is first order. The energy of the laser pulse that does not go into creating this plasma is responsible for further heating the plasma to a higher temperature. Below the threshold, the UV pulse will heat the material but not evaporate or ionize it. If above the threshold, the laser pulse will remove material from the surface as it is volatized and brought to an ionized state. This threshold then is material dependent since the amount of energy required to excite an electron differs as the electronic configuration and molecular bonding structure of each material is different. And, ultimately, these materials can be studied by examining the resulting laser induced plasma (LIP) plume and the characteristic features that surround the formation and propagation of it. The

ionization means that there is a removal of electrons from a bonding orbital in the molecule. It is the point at which the second electron is removed from the orbital that bond breaking occurs.

The wavelength of interaction is not the only consideration to forming the laser induced plasma.[68,69] Significant work has been done to illustrate the effects of backgrounds gas,[70, 71] showing contributions from chemical species[72] and plasma shielding.[73] This work has shown that the background gas (nitrogen) plays a role in product formation and the rates of reaction in air versus argon.[74, 75]

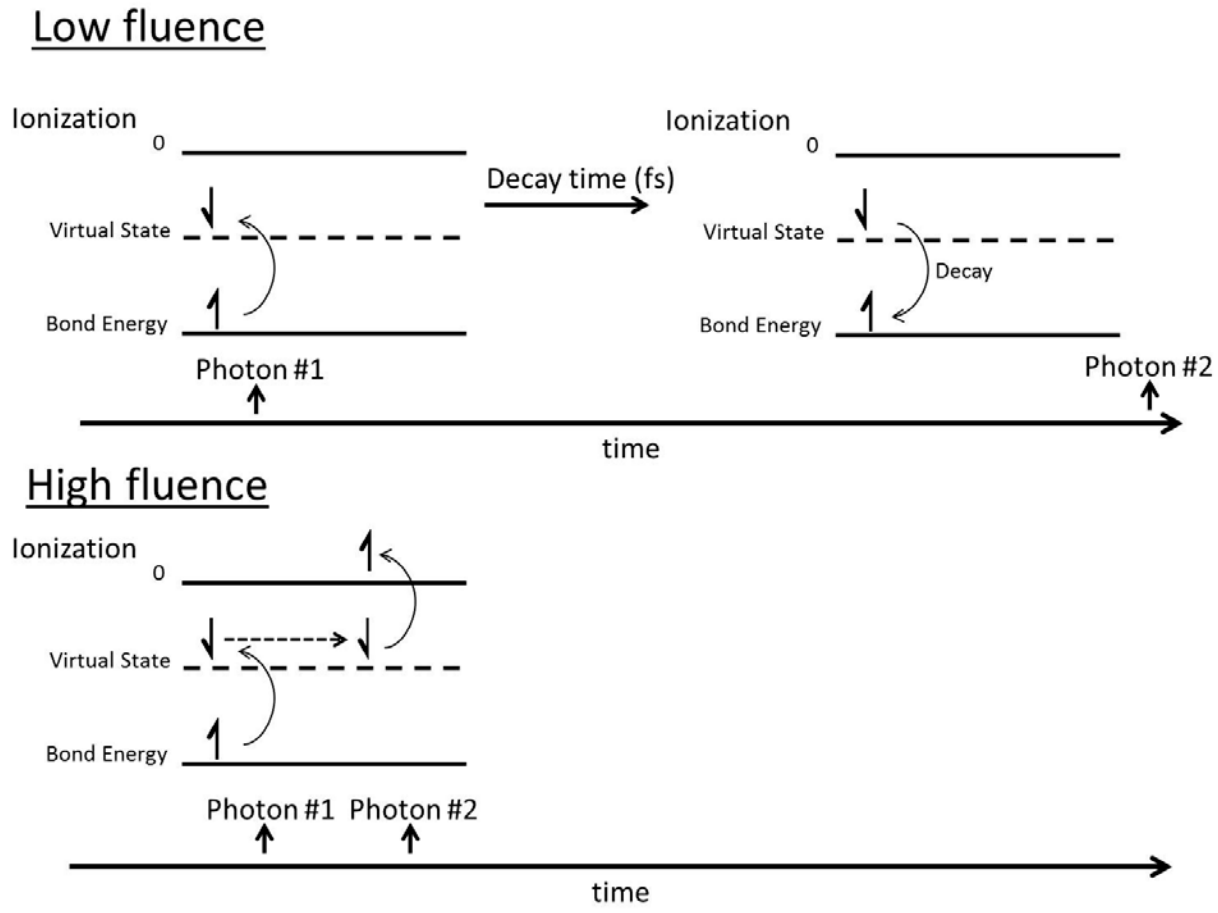

Figure 1.6. Multiphoton excitation process of ultraviolet laser ablation

1.3.2 Fluence dependence on plasma

Changes in fluence affect all aspects of plasma features.[76, 77] At low fluence, a larger portion of the available energy must be used to ionize and form the plasma because there is a larger probability of decay before ionization. Higher fluences have a higher photon flux thus decreasing the portion of the pulse required for plasma formation. After plasma formation, the remaining photons go into heating and further ionization of the plasma. The plasmas metal-like properties make it a strong absorber at all wavelengths. So when there is high fluence, higher degrees of ionization and temperatures.[78-81] Conversely at lower fluences the opposite is the case. Trends in fluence dependence can be established through the comparison of experiments as fluence is adjusted on the samples.

At lower fluences, the duration of the laser pulse that goes into forming the plasma versus heating the plasma will directly affect the duration of the plasma emission.[80] The ablation threshold requires more photons to be absorbed by the solid material at low fluences due to the inefficiency in ionization. In the higher fluence case, the ionization process is more efficient and the rest of the laser pulse energy can further heat and excite the species present already in the plasma state. It has been shown that the fluence of the beam is directly responsible for various chemical phenomena taking place.[82]

Two consequences of fluence dependence on the ablation process are shown in Figure 1.7. When the laser pulse is highly focused (high fluence) the photon density is greater. Therefore the time of the laser pulse, the fraction of photons necessary to ionize the plasma is small and the rest of the photons in the laser pulse can go to heating the plasma. When the laser pulse is less focused (low fluence) the photon density is lower, resulting in more photons being used to create the plasma and less contributing to heating. The fluence dependence therefore also

directly affects the volume of material ablation. A tightly focused beam will have a smaller diameter spot size on the material and a higher fluence. With higher fluence therefore, a smaller fraction of light will be used for the removal and more for heating, but the depth at which the beam will penetrate the material will be greater. A widely focused beam will therefore be spread out farther on the surface, not penetrate as deep, but have a wider diameter. The spot size, pit area, and volume of material removed are directly related to the fluence. A non-linear relationship in fluence dependence on ablation represents a multi-photon adsorption process. When the increase in area is not linear, the $A = \pi r^2$ dependence on the ablation process means that ablation depth will be lost faster than any gain in ablation width. The deeper penetration depth of the pulse does not mean that it is proportional to the volume removed.

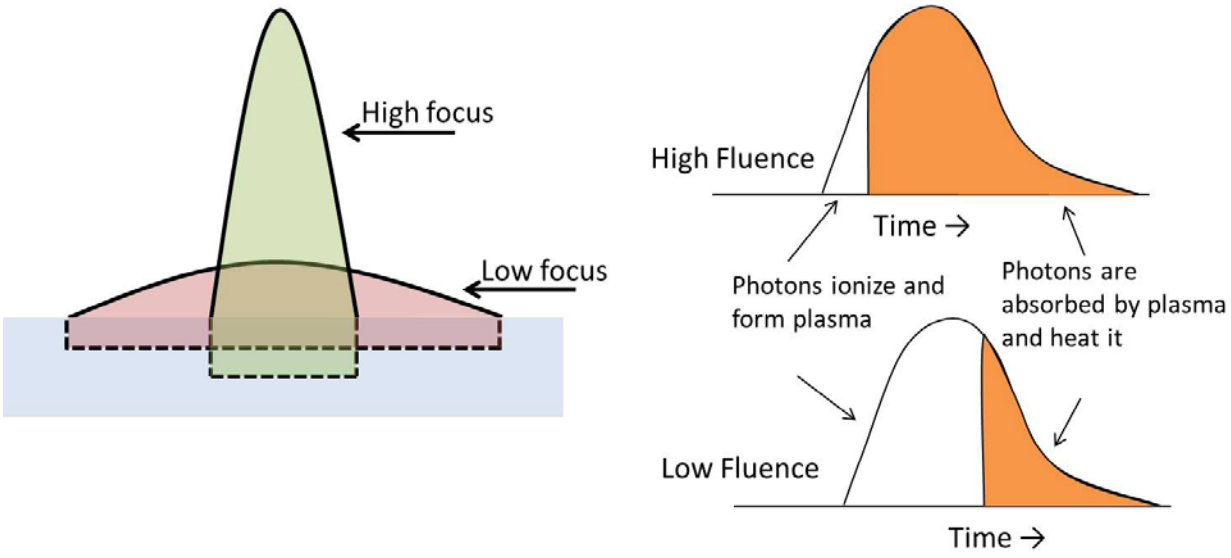

Figure 1.7. The influence of laser fluence dictates the surface area and volume of the laser ablation process, and the amount of the laser pulse that goes into ionization and plasma formation versus continued plasma heating

1.4 Lasers as an analytical technique

1.4.1 The emission spectrum

Optical emission spectroscopy (OES)[83] is an analytical technique that is often paired with laser induced plasma events which is frequently referred to as laser induced breakdown spectroscopy (LIBS).[84-88] The ionization of the solid sample, as previously described, creates a plasma. This plasma strongly emits a large amount of electromagnetic radiation through the ultraviolet (UV), visible (VIS), and infrared (IR) regions. An emission spectra can contain a lot of valuable information about the emitting species in the form of spectral lines[72], or continuum emission.[89-91] Sharp spectral lines,[92] give information about specific transitions, broadband continuum emission can give information about temperature,[93] and ratios[94] of features in the spectrum can give insight into electron densities.

1.4.2 Spectroscopy instrumentation

The emitted photon from an excited species spans the electromagnetic spectrum in the form of short to long wavelengths, high to low energy. The information of interest must therefore be measured by use of a detector suited to look at that specific region. Different types of radiation require different methods of detection. For the laser induced plasma events, a good degree of the chemical information is contained from the UV to IR regions, including the VIS. Therefore the methods of detection contained herein will focus on working with visible light in the 300-800 nm region.

The emission from laser induced plasmas is made up of all wavelengths, when light of different wavelengths encounters different materials it will bend and refract to different degrees depending on the specific wavelength of light and the refractive index of the diffraction grating. Spectroscopic instrumentation takes advantage of these properties of light by use of various

optics and lenses that diffract the light to different angles, thus separating it by wavelength into physically different positions in space. A schematic of the spectrometer is shown in Figure 1.8.

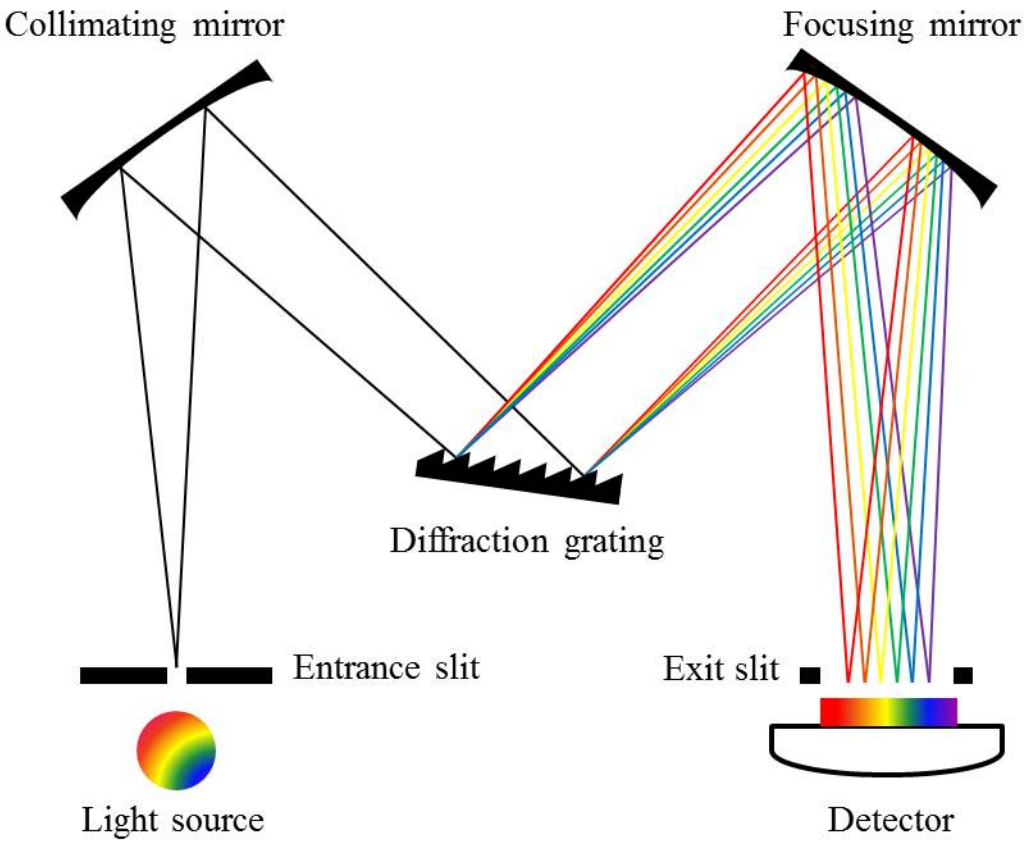

Figure 1.8. Schematic design of diffraction based spectrometer, where detector can be a camera

1.4.3 Collection optics

Various optics are often employed in efficiently coupling the electromagnetic radiation into the spectrometer. Typically various collection lenses and fiber optic cables (Figures 1.9 and 1.10) are employed to increase the efficiency of collection. Coupling light into the fiber is just as important because the efficiency of the spectrometer is dependent upon the amount of light collected. To collect the light, a ball lens is often employed to effectively capture light over a wider angular range than the fiber. The exit of the light from the ball lens is focused precisely behind it. A fiber optic cable is often employed to carry the light from the ball lens to the entrance of the spectrometer. This effectively acts as a “light pipe” carrying the light from one end to the other. The multimode nature of the fiber, due to interior diameters and coating thicknesses allows the light to travel from one end to another in the same polychromatic fashion.

.

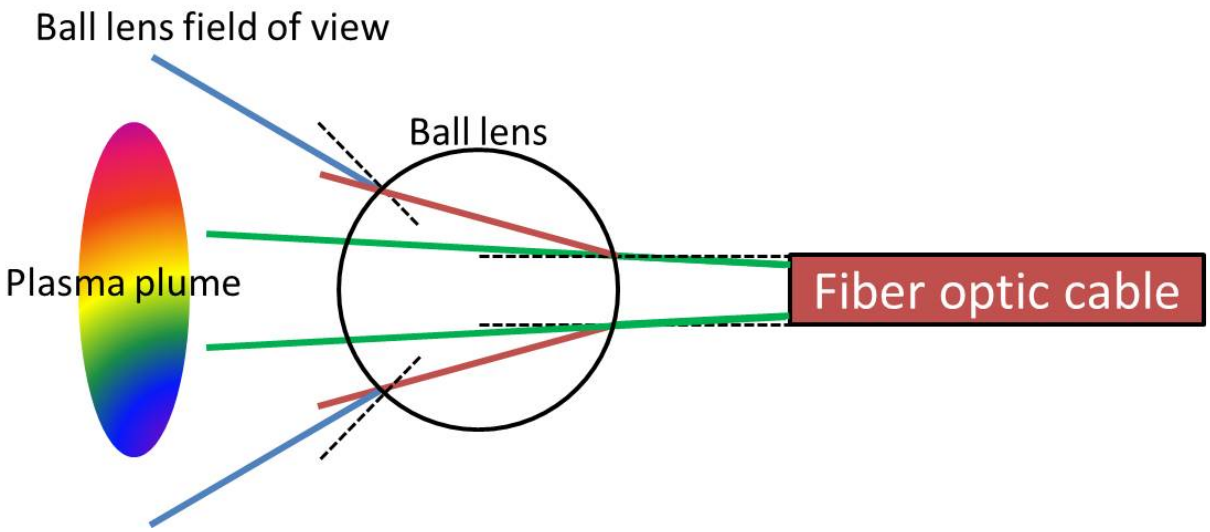

Figure 1.9. Ball lens increases the angle of acceptance of the fiber optic cable

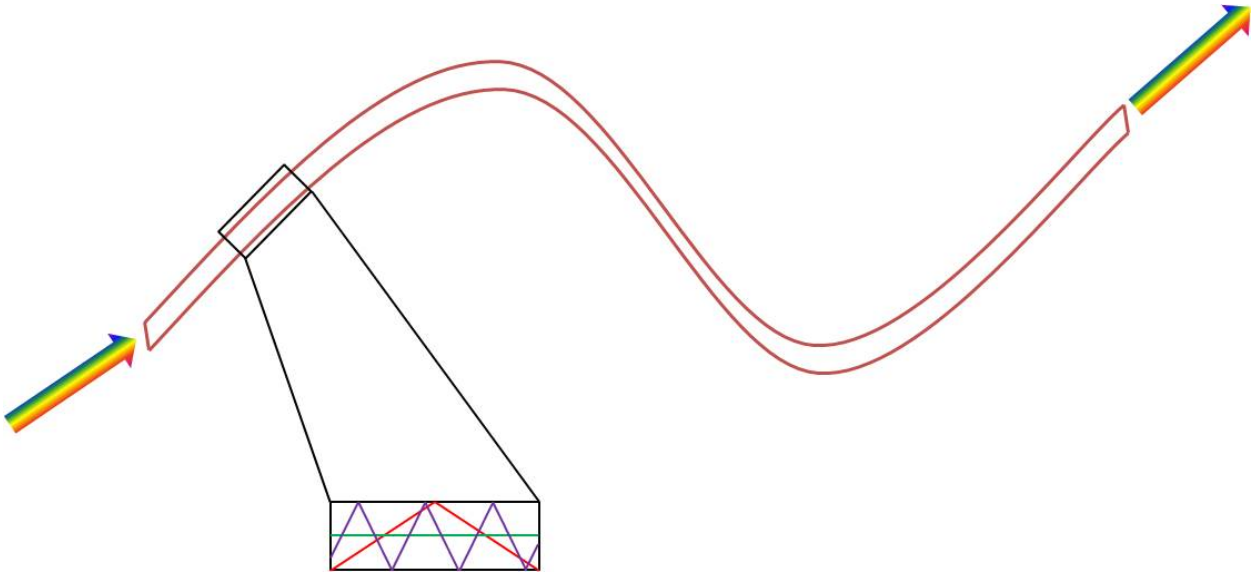

Figure 1.10. The fiber optic cable allows the light to travel efficiently from one point to another

1.4.4 Spectrum analysis

After the light has been collected in the detector, analysis of the resulting spectrum must take place. The radiation can have many different distributions of light depending on the chemical makeup of the sample. To describe the electromagnetic radiation observed, Planks law is often employed to calculate the blackbody radiation based upon the spectral radiance observed.[94,90]

$$I(\upsilon, T) = \frac{2h\upsilon^3}{c^2} \frac{1}{e^{h\upsilon/k_B T} - 1} \quad (1.2)$$

The composition of the plasma[95] can be characterized in terms of electron density,[93, 96] temperature,[92, 97] concentration of ionic species,[98, 99] and atomic species that may be present.[100, 101]

Each of the aforementioned characteristics of the plasma individually and in combination contributes to the chemical fingerprint of the sample and the laser pulse involved.[102, 103] This allows laser ablation and the associated plasma to be used as a spectroscopic technique. LIBS, depicted in Figure1.11, can be used for material identification, atomic spectroscopy, and also as a test of the physical properties of the sample. Being an entirely optical technique, there is the advantage of not having any instrument in close proximity to the sample, as fiber optics can be employed to deliver the pulse and collect the emission spectrum.[104] Although part of the material is ionized and removed, the ablated fraction is typically on the nano-gram scale so the sample tested can be small. But, the limits of detection and reproducibility are sample dependent.

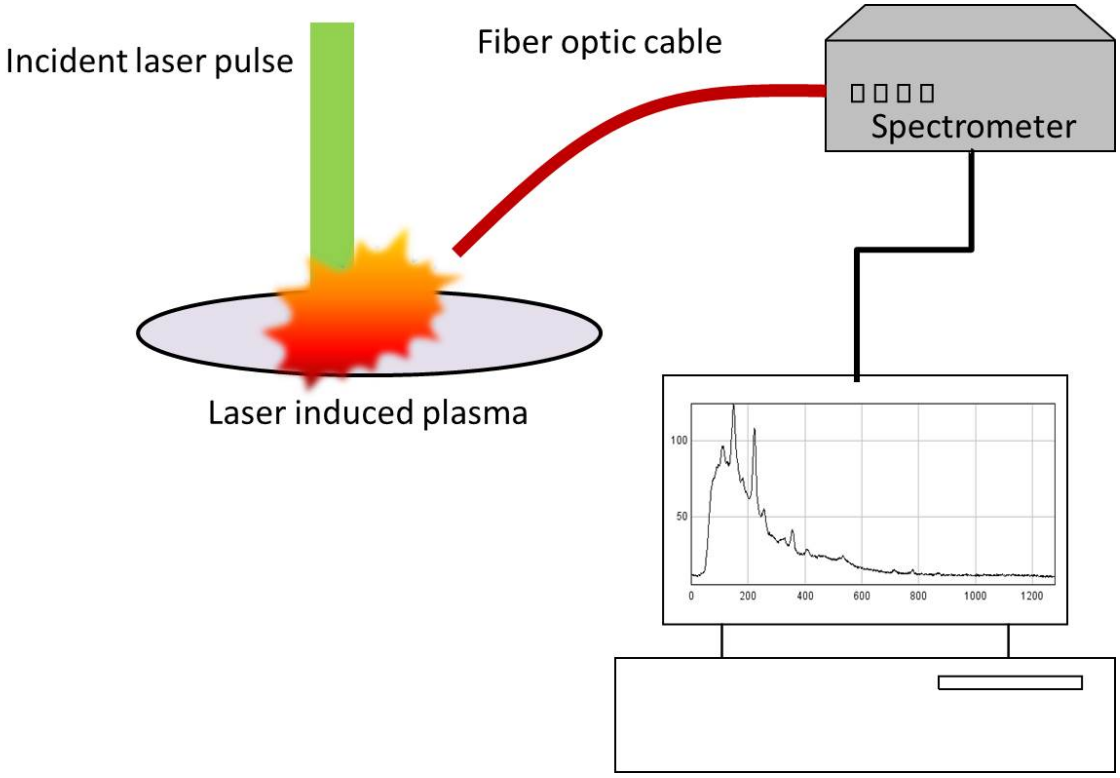

Figure 1.11. Typical schematic of laser induced breakdown spectrometer

1.4.5 Lasers for use with explosive ignition

A laser can be used as a powerful analytical tool as previously described and also as a focused source of high energy.[105] A high energy laser pulse can ionize the material directly to a plasma,[106-108] and the resulting plasma species can be used as more than an analytical label to the material.[88, 109] The energetic material laser interaction[59, 110] can be used to study photodecomposition mechanisms,[111, 112] reaction temperatures,[113, 114] kinetics,[115] and probe the material for ignition characteristics.[108, 116-118] This plasma contains energetic species[119, 120] that can directly be studied.[112, 115] For example, the broad emission of light has been used as a continuum source in absorption experiments.[121-125] Alternatively, the energetic species present in the plasma can be used as a source themselves for initiating energetic materials.

The use of laser ablation in explosives has been examined in a variety of cases. For many samples, irradiating the explosive directly with a laser beam does not induce ignition[126] as they are not photoactive in the regions of specific laser wavelength. There are various methods of achieving optical initiation of explosives. Some explosives have dyes[126, 127] added to them to enhance the absorption of light. Other explosives have nanoparticle additives[128, 129] that then absorb laser light, and create explosive heating within the energetic material. There are also cases of selectively tuning the synthesis of materials or the laser pulse itself [64, 130] for the initiation of energetic materials.

There are still barriers to overcome however to enhance the optical coupling of laser light to the materials. Instead of directly attempting to initiate the energetic material, a material that is more easily ignitable can be irradiated, and those products then used to ignite the EM. In ETC the significant chemical species responsible for ignition in EM, as modeled experimentally,[46, 47] was the H•. In ECR microwave plasmas this species is readily produced. The ionization of

polymers with a high concentration of hydrogen can also produce the same reactive species. Some polymers are easier to convert to high energy plasmas than others. Polymers have been used in the ETC igniters and can easily be converted to a plasma with a laser thus also producing the correct H• needed for initiation.

If one wants to try and ignite an EM by means of a laser induced plasma adjacent to it as depicted in Figure 1.12, the type of laser pulse used then becomes important. Infrared (IR) lasers heat polymer materials. In contrast, ultraviolet lasers are powerful enough to directly ionize the material into a gaseous plasma state. Presumably, the selective irradiation with a UV pulse on the correct polymer will then produce a high enough concentration of H•. These reactive species, in combination with the high temperatures associated with the ionization process, and the high pressures generated by the gas expansion, will induce ignition. This process then serves as a replacement for ETC ignition.[54, 131, 132]

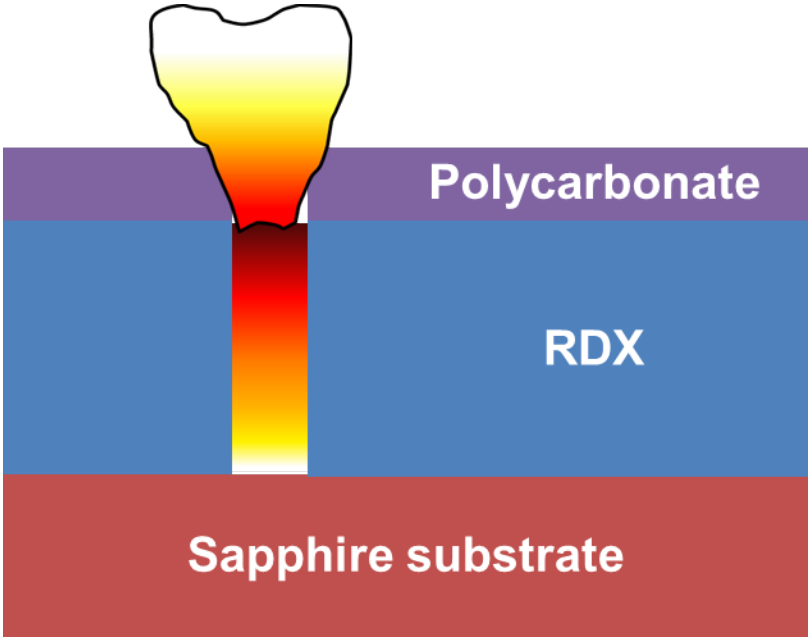

Figure 1.12. Proposed laser induced plasma ignition design

1.6 References

1. Akhavan, J., *The chemistry of Explosives, Second Edition*. 2004; p 180 pp.
2. Fajardo, M. E.; Lewis, W. K. *Progress Towards a Benchtop Energetics Capability (BRIEFING CHARTS)*; DTIC Document: 2006.
3. Couteur, P. L.; Burreson, J., *Napoleon's Buttons: 17 Molecules that Changed History*. Jeremy P. Tarcher/Penguin: 2004.
4. Wang, Y.; Jiang, W.; Song, D.; Liu, J.; Guo, X.; Liu, H.; Li, F., *Journal of thermal analysis and calorimetry* **2013,** *111*, 85-92.
5. Kuo, K. K.-y.; Acharya, R., *Applications of turbulent and multi-phase combustion*. John Wiley & Sons: 2012.
6. Agrawal, J. P., *Central European Journal of Energetic Materials* **2012,** *9*, 273-290.
7. Rice, B. M. In *Multiscale modeling of energetic materials: Easy to say, harder to do*, 2012, AIP Publishing: pp 1241-1246.
8. Akiki, M.; Menon, S., *Combustion and Flame* **2015,** *162*, 1759-1771.
9. Field, J. E.; Bourne, N. K.; Palmer, S. J. P.; Walley, S. M.; Sharma, J.; Beard, B. C., *Philosophical Transactions of the Royal Society of London A: Mathematical, Physical and Engineering Sciences* **1992,** *339*, 269-283.
10. Mahadevan, E. G., Classification of Explosives. In *Ammonium Nitrate Explosives for Civil Applications*, Wiley-VCH Verlag GmbH & Co. KGaA: 2013; pp 1-3.
11. Fried, L. E.; Ruggiero, A. J., *The Journal of Physical Chemistry* **1994,** *98*, 9786-9791.
12. Tsiaousis, D.; Munn, R. W., *The Journal of chemical physics* **2005,** *122*, 184708.
13. Kishore, K., *Defence Science Journal* **2014,** *28*, 59-66.

14. Maienschein, J. L. In *Research topics in explosives-a look at explosives behaviors*, 2014, IOP Publishing: p 052027.

15. De Lucia Jr, F. C.; Gottfried, J. L., *The Journal of Physical Chemistry A* **2013,** *117*, 9555-9563.

16. Keshavarz, M. H., *Propellants, Explosives, Pyrotechnics* **2012,** *37*, 93-99.

17. Kaste, P. J.; Rice, B. M., *AMPTIAC Q* **2004,** *8*, 84-90.

18. Rossi, C., *Propellants, Explosives, Pyrotechnics* **2014,** *39*, 323-327.

19. Fajardo, M. E.; Fossum, E. C.; Molek, C. D.; Lewis, W. K.; Nep, R. M. *Benchtop Energetics Progress*; DTIC Document: 2011.

20. Fajardo, M. E.; Lewis Iii, W. K.; Ashley, V. L.; Nep, R. M.; Fossum, E. C.; Molek, C. D. *Benchtop Energetics: Research Progress, Concept Evaluation, and Apparatus Development*; DTIC Document: 2012.

21. Fossum, E. C.; Molek, C. D.; Lewis, W. K.; Fajardo, M. E., *Propellants, Explosives, Pyrotechnics* **2012,** *37*, 445-458.

22. Greenaway, M. W.; Gifford, M. J.; Proud, W. G.; Field, J. E.; Goveas, S. G. In *An investigation into the initiation of hexanitrostilbene by laser-driven flyer plates*, 2002, IOP Institute of Physics Publishing LTD: pp 1035-1038.

23. Brown, K. E.; Shaw, W. L.; Zheng, X.; Dlott, D. D., *Review of Scientific Instruments* **2012,** *83*, 103901.

24. Curtis, A. D.; Banishev, A. A.; Shaw, W. L.; Dlott, D. D., *Review of Scientific Instruments* **2014,** *85*, 043908.

25. Shaw, W. L.; Curtis, A. D.; Banishev, A. A.; Dlott, D. D. In *Laser-driven flyer plates for shock compression spectroscopy*, 2014, IOP Publishing: p 142011.

26. Chen, S.; Wu, L.; Shen, R.; Ye, Y.; Hua, T., *Laser Physics* **2013,** *23*, 125002.

27. Paisley, D. L.; Luo, S.-N.; Greenfield, S. R.; Koskelo, A. C., *Review of Scientific Instruments* **2008,** *79*, 023902.

28. Watson, S.; Field, J. E., *Journal of Physics D: Applied Physics* **2000,** *33*, 170.

29. Yu, H.; Fedotov, V.; Baek, W.; Yoh, J. J., *Applied Physics A* **2014,** *115*, 971-978.

30. Gottfried, J. L., *Physical Chemistry Chemical Physics* **2014,** *16*, 21452-21466.

31. Gottfried, J. L., *Propellants, Explosives, Pyrotechnics* **2015**.

32. Murphy, M. J.; Clarke, S. A., Ultra-High-Speed Imaging for Explosive-Driven Shocks in Transparent Media. In *Dynamic Behavior of Materials, Volume 1*, Springer: 2013; pp 425-432.

33. Gregorčič, P.; Možina, J., *Optics letters* **2011,** *36*, 2782-2784.

34. Gregorčič, P.; Diaci, J.; Možina, J., *Applied Physics A* **2013,** *112*, 49-55.

35. MacPhee, A. G.; Akli, K. U.; Beg, F. N.; Chen, C. D.; Chen, H.; Clarke, R.; Hey, D. S.; Freeman, R. R.; Kemp, A. J.; Key, M. H., *Review of Scientific Instruments* **2008,** *79*, 10F302.

36. Matyáš, R.; Pachman, J., Introduction to Initiating Substances. In *Primary Explosives*, Springer Berlin Heidelberg: 2013; pp 1-10.

37. Li, X.; Li, R.; Jia, S.; Zhang, Y., *Journal of Applied Physics* **2012,** *112*, 063303.

38. Pesce-Rodriguez, R. A.; Beyer, R. A., *Army Research Lab. Tech. Rep. t ARL-TR* **2004,** *3286*.

39. Williams, A. W.; Beyer, R. A. *Ablation Loss Studies for Capillary-Sustained Plasmas*; DTIC Document: 2006.

40. Fifer, R. A.; Sagan, E. S.; Beyer, R. A., *Magnetics, IEEE Transactions on* **2003,** *39*, 218-222.

41. Chaboki, A.; Zelenak, S.; Isle, B., *Magnetics, IEEE Transactions on* **1997,** *33*, 284-288.

42. Porwitzky, A. J.; Keidar, M.; Boyd, I. D. In *Progress towards an end-to-end model of an electrothermal chemical gun*, 2008, IEEE: pp 1-6.

43. Kappen, K. *Radiation Transfer Modeling in Electrothermal Chemical (ETC) Ignition*; DTIC Document: 2002.

44. Starikovskiy, A.; Aleksandrov, N., *Progress in Energy and Combustion Science* **2013,** *39*, 61-110.

45. Dyvik, J.; Herbig, J.; Appleton, R.; Reilly, J. O.; Shin, J., *Ieee Transactions on Magnetics* **2007,** *43*, 303-307.

46. Blumenthal, R. *Understanding the Plasma-Propellant Interaction through Experimental Modeling*; DTIC Document: 2009.

47. Valliere, R.; Blumenthal, R., *Journal of Applied Physics* **2006,** *100*, 084904.

48. Boueri, M.; Baudelet, M.; Yu, J.; Mao, X. L.; Mao, S. S.; Russo, R., *Applied Surface Science* **2009,** *255*, 9566-9571.

49. Schmidt, H.; Ihlemann, J.; Wolff-Rottke, B.; Luther, K.; Troe, J., *Journal of applied physics* **1998,** *83*, 5458-5468.

50. Srinivasan, R.; Braren, B., *Chemical Reviews* **1989,** *89*, 1303-1316.

51. Bityurin, N., *Annual Reports Section" C"(Physical Chemistry)* **2005,** *101*, 216-247.

52. Bormotova, T. A.; Blumenthal, R., *Journal of Applied Physics* **2009,** *105*, 4910.

53. Beyer, R.; Pesce-Rodriguez, R. In *The response of propellants to plasma radiation*, 2005, IEEE: pp 273-278.

54. Casper IV, W.; denHartog, H.; Blumenthal, R., **A Novel Method For The Laser Induced Ignition Of RDX**. In *Proceedings of the 46st JANNAF Combustion Subcommittee Meeting*, CPIAC: Albuquerque, NM, 2014.

55. Gottfried, J. L.; Harmon, R. S.; Munson, C. A.; Winkel Jr, R. J.; Miziolek, A. W. *Detection of Energetic Materials and Explosive Residues With Laser-Induced Breakdown Spectroscopy: 1. Laboratory Measurements*; DTIC Document: 2007.

56. Sunku, S.; Gundawar, M. K.; Myakalwar, A. K.; Kiran, P. P.; Tewari, S. P.; Rao, S. V., *Spectrochimica Acta Part B: Atomic Spectroscopy* **2013,** *79*, 31-38.

57. Gottfried, J. L.; De Lucia Jr, F. C.; Munson, C. A.; Miziolek, A. W., *Journal of Analytical Atomic Spectrometry* **2008,** *23*, 205-216.

58. Lopez-Moreno, C.; Palanco, S.; Laserna, J. J.; DeLucia Jr, F.; Miziolek, A. W.; Rose, J.; Walters, R. A.; Whitehouse, A. I., *Journal of Analytical Atomic Spectrometry* **2006,** *21*, 55-60.

59. Glumac, N., *Shock Waves* **2013,** *23*, 131-138.

60. López-Claros, M.; Vadillo, J. M.; Laserna, J. J., *Journal of Analytical Atomic Spectrometry* **2015**.

61. Ma, Q. L.; Motto-Ros, V.; Lei, W. Q.; Wang, X. C.; Boueri, M.; Laye, F.; Zeng, C. Q.; Sausy, M.; Wartelle, A.; Bai, X. S. In *Characteristics of laser-induced plasma as a spectroscopic light emission source*, 2012, p 243.

62. Johnson, S. L. Resonant-Infrared laser ablation of polymers: Mechanisms and applications. Vanderbilt University, Nashville, TN, 2008.

63. Wang, Q.; Jander, P.; Fricke-Begemann, C.; Noll, R., *Spectrochimica Acta Part B: Atomic Spectroscopy* **2008,** *63*, 1011-1015.

64. Greenfield, M. T.; McGrane, S. D.; Bolme, C. A.; Bjorgaard, J. A.; Nelson, T. R.; Tretiak, S.; Scharff, R. J., *The Journal of Physical Chemistry A* **2015,** *119*, 4846-4855.

65. Ahmad, S. R.; Russell, D. A., *Propellants, Explosives, Pyrotechnics* **2005,** *30*, 131-139.

66. Ma, Q.; Motto-Ros, V.; Laye, F.; Yu, J.; Lei, W.; Bai, X.; Zheng, L.; Zeng, H., *Journal of Applied Physics* **2012,** *111*, 053301.

67. Baravian, G.; Godart, J.; Sultan, G., *Applied Physics Letters* **1980,** *36*, 415-416.

68. Tozer, B. A., *Physical Review* **1965,** *137*, A1665.

69. Meyerand Jr, R. G.; Haught, A. F., *Physical Review Letters* **1963,** *11*, 401.

70. Park, H. S.; Nam, S. H.; Park, S. M., *Journal of applied physics* **2005,** *97*, 113103-113103.

71. De Giacomo, A.; Dell'Aglio, M.; Gaudiuso, R.; Amoruso, S.; De Pascale, O., *Spectrochimica Acta Part B: Atomic Spectroscopy* **2012,** *78*, 1-19.

72. Hermann, J.; Gerhard, C.; Axente, E.; Dutouquet, C., *Spectrochimica Acta Part B: Atomic Spectroscopy* **2014,** *100*, 189-196.

73. Vadillo, J. M.; Fernandez Romero, J. M.; Rodriguez, C.; Laserna, J. J., *Surface and interface analysis* **1999,** *27*, 1009-1015.

74. Hiyoshi, R. I.; Brill, T. B., *Propellants Explosives Pyrotechnics* **2002,** *27*, 23-30.

75. Mao, X. L.; Chan, W. T.; Shannon, M. A.; Russo, R. E., *Journal of applied physics* **1993,** *74*, 4915-4922.

76. Chen, J. Z.; Zhao, S. R.; Wei, Y. H.; Guo, Q. L.; Huai, S. F., *Spectroscopy and Spectral Analysis* **2005,** *25*, 1693-1696.

77. Malevich, P. N.; Chumakov, A. N., *Journal of Applied Spectroscopy* **2012**, 1-5.

78. Zhang, S.; Wang, X.; He, M.; Jiang, Y.; Zhang, B.; Hang, W.; Huang, B., *Spectrochimica Acta Part B: Atomic Spectroscopy* **2014,** *97*, 13-33.

79. Rusak, D. A.; Castle, B. C.; Smith, B. W.; Winefordner, J. D., *Spectrochimica Acta Part B: Atomic Spectroscopy* **1997,** *52*, 1929-1935.

80. Bai, X.; Motto-Ros, V.; Lei, W.; Zheng, L.; Yu, J., *Spectrochimica Acta Part B: Atomic Spectroscopy* **2014,** *99*, 193-200.

81. Lam, J.; Motto-Ros, V.; Misiak, D.; Dujardin, C.; Ledoux, G.; Amans, D., *Spectrochimica Acta Part B: Atomic Spectroscopy* **2014,** *101*, 86-92.

82. Ionin, A. A.; Kudryashov, S. I.; Makarov, S. V.; Saltuganov, P. N.; Seleznev, L. V.; Sinitsyn, D. V.; Lednev, V. A.; Pershin, S. M., *JETP Letters* **2015,** *101*, 308-312.

83. Verhoff, B.; Harilal, S. S.; Freeman, J. R.; Diwakar, P. K.; Hassanein, A., *Journal of Applied Physics* **2012,** *112*, 093303.

84. Lerner, J. M.; Thevenon, A., Optics of Spectroscopy Tutorial. In HORIBA, Ed. 2015.

85. D'Angelo, C. A.; Pace, D. M. D.; Bertuccelli, G.; Bertuccelli, D., *Spectrochimica Acta Part B: Atomic Spectroscopy* **2008,** *63*, 367-374.

86. Unnikrishnan, V. K.; Mridul, K.; Nayak, R.; Alti, K.; Kartha, V. B.; Santhosh, C.; Gupta, G. P.; Suri, B. M., *Pramana* **2012,** *79*, 299-310.

87. Cvejić, M. In *Diagnostics of laser-induced plasma by optical emission spectroscopy*, 2014, IOP Publishing: p 012014.

88. Lazic, V.; Palucci, A.; Jovicevic, S.; Poggi, C.; Buono, E., *Spectrochimica Acta Part B: Atomic Spectroscopy* **2009,** *64*, 1028-1039.

89. Luna, H.; Dardis, J.; Doria, D.; Costello, J. T., *Brazilian Journal of Physics* **2007,** *37*, 1301-1305.

90. De Giacomo, A.; Gaudiuso, R.; Dell'Aglio, M.; Santagata, A., *Spectrochimica Acta Part B: Atomic Spectroscopy* **2010,** *65*, 385-394.

91. Nagy, B.; Nemes, L.; Kubinyi, M., *Periodica Polytechnica-Chemical Engineering* **2009,** *53*, 61-66.

92. Bredice, F.; Martinez, P. P.; Sánchez-Aké, C.; Villagrán-Muniz, M., *Spectrochimica Acta Part B: Atomic Spectroscopy* **2015,** *107*, 25-31.

93. Maynard, G.; Lambert, F.; Andreev, N.; Robillar, B.; Boudaa, A.; Clerouin, J.; Cros, B.; Lenglet, A.; Mocek, T.; Sebban, S., *Contributions to Plasma Physics* **2007,** *47*, 352-359.

94. Möllmann, K.-P.; Pinno, F.; Vollmer, M., **2010**.

95. Mohamed, W. T. Y., *Progress in Physics* **2007,** *2*, 87-92.

96. Borges, F. O.; Cavalcanti, G. H.; Gomes, G. C.; Palleschi, V.; Mello, A., *Applied Physics B* **2014,** *117*, 437-444.

97. Mendys, A.; Kański, M.; Farah-Sougueh, A.; Pellerin, S.; Pokrzywka, B.; Dzierżęga, K., *Spectrochimica Acta Part B: Atomic Spectroscopy* **2014,** *96*, 61-68.

98. Malvezzi, A. M.; Garifo, L.; Jannitti, E.; Nicolosi, P.; Tondello, G., *Journal of Physics B: Atomic and Molecular Physics* **1979,** *12*, 1437.

99. Cvejić, M.; Gavrilović, M. R.; Jovićević, S.; Konjević, N., *Spectrochimica Acta Part B: Atomic Spectroscopy* **2013,** *85*, 20-33.

100. Novotný, J.; Brada, M.; Petrilak, M.; Prochazka, D.; Novotný, K.; Hrdička, A.; Kaiser, J., *Spectrochimica Acta Part B: Atomic Spectroscopy* **2014,** *101*, 149-154.

101. Li, X.; Wang, Z.; Mao, X.; Russo, R. E., *Journal of Analytical Atomic Spectrometry* **2014,** *29*, 2127-2135.

102. Fierro, A.; Laity, G.; Neuber, A., *Journal of Physics D: Applied Physics* **2012,** *45*, 495202.

103. Huang, H.; Yang, L.-M.; Liu, J., *Applied optics* **2012,** *51*, 8669-8676.

104. Cremers, D. A.; Radziemski, L. J., *Handbook of Laser-Induced Breakdown Spectroscopy*. Wiley: 2013.

105. Kemp, A. J.; Fiuza, F.; Debayle, A.; Johzaki, T.; Mori, W. B.; Patel, P. K.; Sentoku, Y.; Silva, L. O., *Nuclear Fusion* **2014,** *54*, 054002.

106. Muller, G. M.; Moore, D. B.; Bernstein, D., *Journal of Applied Physics* **1961,** *32*, 1065.

107. Bhattacharya, A.; Guo, Y. Q.; Bernstein, E. R., *The Journal of Physical Chemistry A* **2009,** *113*, 811-823.

108. Zhang, W.; Shen, R.; Wu, L.; Ye, Y.; Hu, Y. In *Experimental studies on plasma emission spectroscopy of laser ablation of hexahydro-l, 3, 5-trinitro-l, 3, 5-triazine*, 2013, International Society for Optics and Photonics: pp 87961A-87961A.

109. De Lucia, F. C.; Harmon, R. S.; McNesby, K. L.; Winkel, R. J.; Miziolek, A. W., *Applied optics* **2003,** *42*, 6148-6152.

110. Kappen, K.; Beyer, R., *Propellants, Explosives, Pyrotechnics* **2003,** *28*, 32-36.

111. Merten, J.; Jones, M.; Sheppard, C.; Parigger, C.; Allen, S. In *Spatiotemporal evolution of plasma molecular emission following laser ablation of explosive analogs*, 2013, International Society for Optics and Photonics: pp 87100S-87100S.

112. Greenfield, M.; Guo, Y. Q.; Bernstein, E. R., *Chemical physics letters* **2006,** *430*, 277-281.

113. Tang, C.-J.; Lee, Y.; Litzinger, T. A., *Combustion and flame* **1999,** *117*, 244-256.

114. Lewis, W. K.; Rumchik, C. G., *Journal of Applied Physics* **2009,** *105*, 056104.

115. Babushok, V. I.; DeLucia, F. C.; Dagdigian, P. J.; Gottfried, J. L.; Munson, C. A.; Nusca, M. J.; Miziolek, A. W., *Spectrochimica Acta Part B: Atomic Spectroscopy* **2007,** *62*, 1321-1328.

116. Dolgachev, V. A.; Khaneft, A. V. In *Ignition of organic explosives by a laser pulse*, 2015, EDP Sciences: p 01023.

117. Stacy, S. C.; Massad, R. A.; Pantoya, M. L., *Journal of Applied Physics* **2013,** *113*, 213107.

118. Hirlinger, J. M.; Burke, G. C.; Beyer, R. A.; Hamlin, S. J.; Doris, T. In *A laser ignition system for the M230 cannon*, 2005, International Society for Optics and Photonics: pp 587101-587101.

119. Delgado, T.; Vadillo, J. M.; Laserna, J. J., *Journal of Analytical Atomic Spectrometry* **2014,** *29*, 1675-1685.

120. Sreedhar, S.; Nageswara Rao, E.; Manoj Kumar, G.; Tewari, S. P.; Venugopal Rao, S. In *Investigation of molecular and elemental species dynamics in NTO, TNT, and ANTA using femtosecond LIBS technique*, 2013, pp 871012-1.

121. Meighan, O.; Danson, C.; Dardis, L.; Lewis, C. L. S.; MacPhee, A.; McGuinness, C.; O'Rourke, R.; Shaikh, W.; Turcu, I. C. E.; Costello, J. T., *Journal of Physics B: Atomic, Molecular and Optical Physics* **2000,** *33*, 1159.

122. Adamson, A. W.; Cimolino, M. C., *The Journal of Physical Chemistry* **1984,** *88*, 488-490.

123. Laporte, P.; Damany, N.; Damany, H., *Optics Letters* **1987,** *12*, 987-989.

124. D'Yachkov, L. G.; Golubev, O. A.; Kobzev, G. A.; Vargin, A. N., *Journal of Quantitative Spectroscopy and Radiative Transfer* **1978,** *20*, 175-189.

125. Xu, N.; Majidi, V., *Applied spectroscopy* **1993,** *47*, 1134-1139.

126. Aluker, E. D.; Krechetov, A. G.; Mitrofanov, A. Y.; Zverev, A. S.; Kuklja, M. M., *The Journal of Physical Chemistry C* **2012,** *116*, 24482-24486.

127. Brown, K. E.; Fu, Y.; Shaw, W. L.; Dlott, D. D., *Journal of Applied Physics* **2012,** *112*, 103508.

128. Zheng, X.; Curtis, A. D.; Shaw, W. L.; Dlott, D. D., *The Journal of Physical Chemistry C* **2013,** *117*, 4866-4875.

129. Taylor, D. E.; Strawhecker, K. E.; Shanholtz, E. R.; Sorescu, D. C.; Sausa, R. C., *The Journal of Physical Chemistry A* **2014,** *118*, 5083-5097.

130. Greenfield, M.; Mc Grane, S.; Moore, D.; Scharff, R. J. *Towards understanding initiation reactions of explosives via ultrafast laser quantum control*; Los Alamos National Laboratory (LANL): 2010.

131. Dyachenko, A. Studies on laser ablation of polymer coated propellant films. Auburn University, Auburn, AL, 2006.

132. Sun, H.; Blumenthal, R. In *Products of the Ultraviolet Laser Ablation of RDX* The 43rd JANNAF Combustion Subcommittee Meeting, 2009; CPIAC: 2009; pp 2009-0105CS.

Chapter 2

Experimental Design

2.1 Wafer translation

Movement of all samples and variation of the distance between the lens and sample was accomplished through the use of a three axis computer – controlled positioning system on a 4'x4' optical breadboard table. The Parker-Dadaell motors and rails (Parker, 404-XR) were controlled with a Galil DMC-1800 motion controller. The resolution was 12 μm on the x and y axis (80 cm travel distance) and 8 μm on the z (30 cm travel distance), both with a 3 μm repeatability. The computer interface with the positioning system was handled through the Galil DMC "Smart Terminal" software[1] which allowed integration of the motion within custom written experimental program routines (Appendix 1) so that movement could be coordinated with data collection. The lens to sample distance in a laser set up is an important adjustment for the fluence of the pulse. The 120 mm focal length lens was posited on the x axis and was thus able to be controlled very precisely. For experiments where the fluence was adjusted, the programming allowed the x axis to be changed per experimental parameters. The 2" (50.8 mm) wafers were held in place by a custom made wafer holder seen in Figure 2.1 that was mounted on the YZ axis and placed at the end of the X axis.

Figure 2.1. Sample holder without sample (left) and with 2” RDX wafer (right)

2.2 Experimental programming

The interface of the driving electronics origination trigger pulse, the laser, the motion control hardware, the CCD camera, and the oscilloscope all had proprietary software packages with unique programming language. To overcome this barrier, a third party software package, AutoIt[2] was used to communicate to all software in the Windows XP architecture. AutoIt programming scripts were written (Appendix 1) that would control the laser, fire the origination pulse, retrieve and save the resulting CCD image of the Image intensified (II) spectra, download the resulting photodiode trace from oscilloscope #2 and save it, communicate with the motion control to move the sample, and repeat the experiment.

Programming scripts were written in the native DMC motion control program for sample movement across the wafer to ensure precise placement of the 70 shots, to move the wafer systematically through spraying techniques, and for movement across the x-axis for fluence measurements. The movement could be accomplished in an automated manner by the use of internal scripts alone, through an external trigger interface with internal scripts, or through the use of the AutoIt software to enter specified motion routines.

2.3 Sample preparation

2.3.1 Drop cast films

For samples where a uniform thickness was not overly important, but simply a thick, ~100 μm or greater film was necessary the films were prepared from a concentrated solution and drop cast. Sucrose and ammonium nitrate were prepared in this manner. Polymer samples that were purchased as solid thin films were cut to fit the sample holder designed for a 2” wafer. Therefore the preparation time was minimal. The drop cast solutions were deposited on a 2” borosilicate or sapphire wafer and allowed to dry overnight.

2.3.2 Spray deposition

Using the nebulizing spray technique previously designed,[3] this expanded upon technique depicted in Figure 2.2 was used to spray films over large areas with uniform thickness. Typically, using a syringe pump (New Era, NE-1000) with a 10 mL gas-tight syringe (Hamilton 81620), a solution of 5 mg/mL solution of RDX in acetonitrile was pumped through a 32 GA SS-302 capillary. Surrounding the capillary was a flow of nitrogen that served as the carrier gas. The solution was slowly pumped through the capillary to create small droplets of the solution at the tip of the capillary. The carrier gas dried this solution to a solid as it flowed from the capillary to the wafer. The distance from the capillary tip to the surface of the wafer and the carrier gas flow rate determined the size of the RDX crystals and the porosity of the thin film.[4] A 41.28 mm distance and flow rate of at 20 psi (138 kPa) was used for all experiments in this work as determined by precise positioning on the z-axis to ensure uniform films. The wafer was spun below the capillary at a constant rate of 220 rpm on a motorized chuck. The geometry of the nebulizing spray deposition is shown in Figure 2.2.

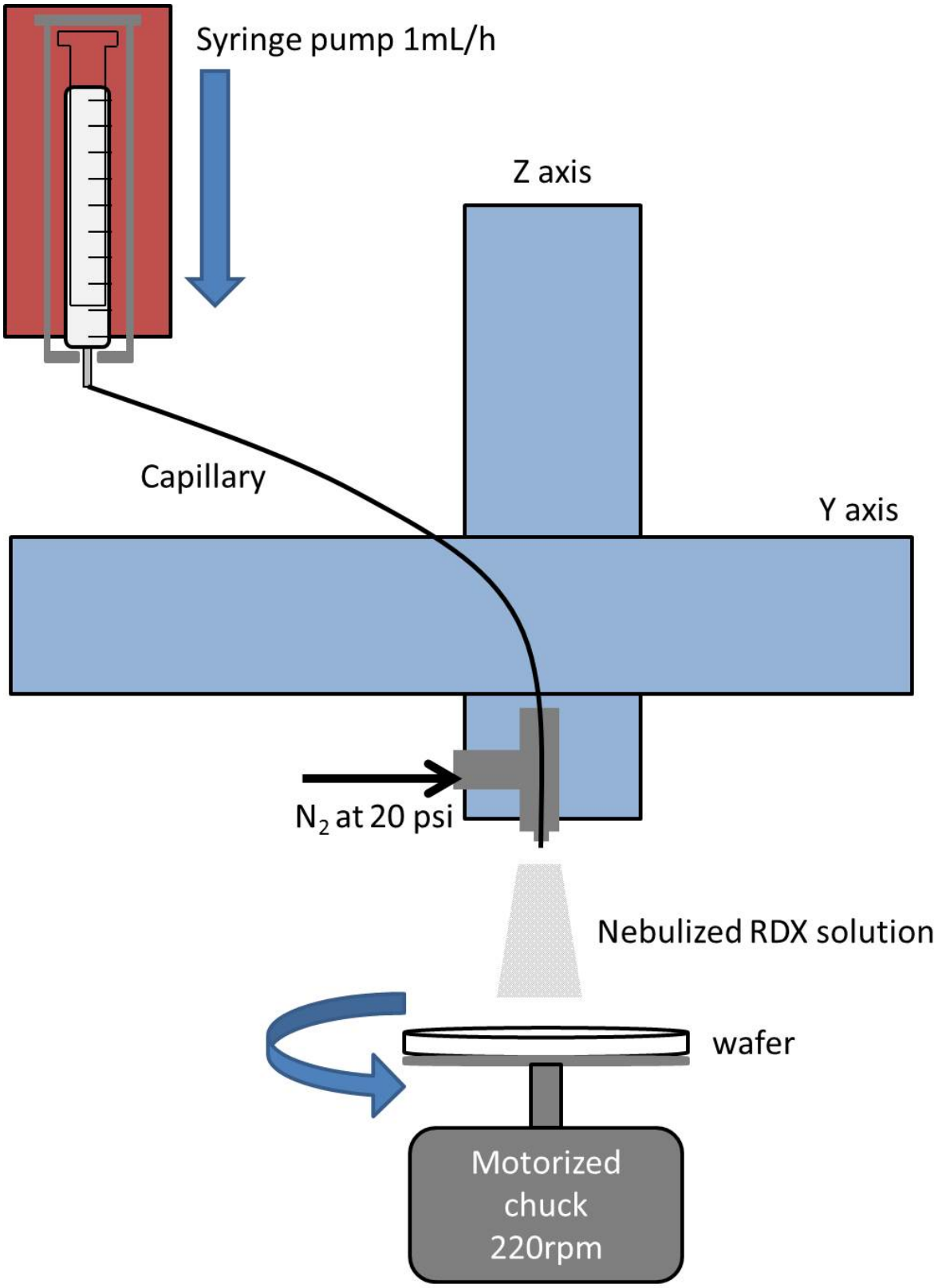

Figure 2.2. Experimental set up of nebulized sprayer on x-y axis to spray large surface area thin films.

An automation program was written to spray the 2” wafer uniformly. The y axis was translated across the wafer from center to edge in 100 µm increments which was determined to be a small enough step to create a uniform film. Given the typical volume of 10 mL and the rate of 10 mL/h, the typical total spray time was 10 h. The substrate was a 2” wafer that was used for all experiments. The circumference of the wafer at each 100 µm increment from center to edge was calculated, summed, and divided by the total spray time (3600 s).

$$\frac{t}{c} = \frac{3600s}{\sum_{25.4mm}^{0mm}(2\pi r)} = \frac{1.77ms}{mm} \quad (2.1)$$

The calculated t/c constant of 1.77 ms/mm, was then multiplied by the total circumference at each 100µm point across the wafer to give a total time for the capillary to spend at each point. As the sprayer was moved from center to edge then, it would stay positioned for longer time periods to account for the increase in circumference with radius. The thickness of the films was only limited by the volume of solution sprayed. Films of RDX as thin at 5 µm and as thick at 50 µm have been prepared using this method.

2.3.3 Spin coating

Some experiments were carried out with polycarbonate covered RDX wafers. The preparation of the RDX was standard in this case and a polycarbonate overlayer was deposited on the already prepared wafer. To a 20 mL solution of dichloromethane (DCM), 600 mg of PC thin film (the same PC film used on its own) was dissolved. Approximately 2 mL of that PC/DCM solution was deposited at the center of the RDX coated wafer and was spun (Laurell WS-400) with a program of 500 rpm for five seconds and 1500 rpm for forty-five seconds to achieve a resulting thickness of 0.6 µm.

2.4 RDX analysis

To determine the thickness of spraying conditions, thin films were analyzed with a scanning electron microscope (SEM) and optical microscopic imaging. When using the SEM, an RDX wafer under standard spraying conditions was fractured in half. The interior portion of the halved wafer was positioned perpendicular to the positioning camera in the SEM. As seen in Figure 2.3, the borosilicate glass wafer can be seen on the bottom of the image. On top of that is the deposited RDX film outlined in red. This precise camera allowed the RDX film to be measured as 13.5 µm. Optical microscopy images of RDX films on borosilicate glass wafers are seen in Figure 2.4. The white in the images is empty space and the RDX crystallites are black. As indicated, the capillary to sample distance affected the porosity of the deposited film.

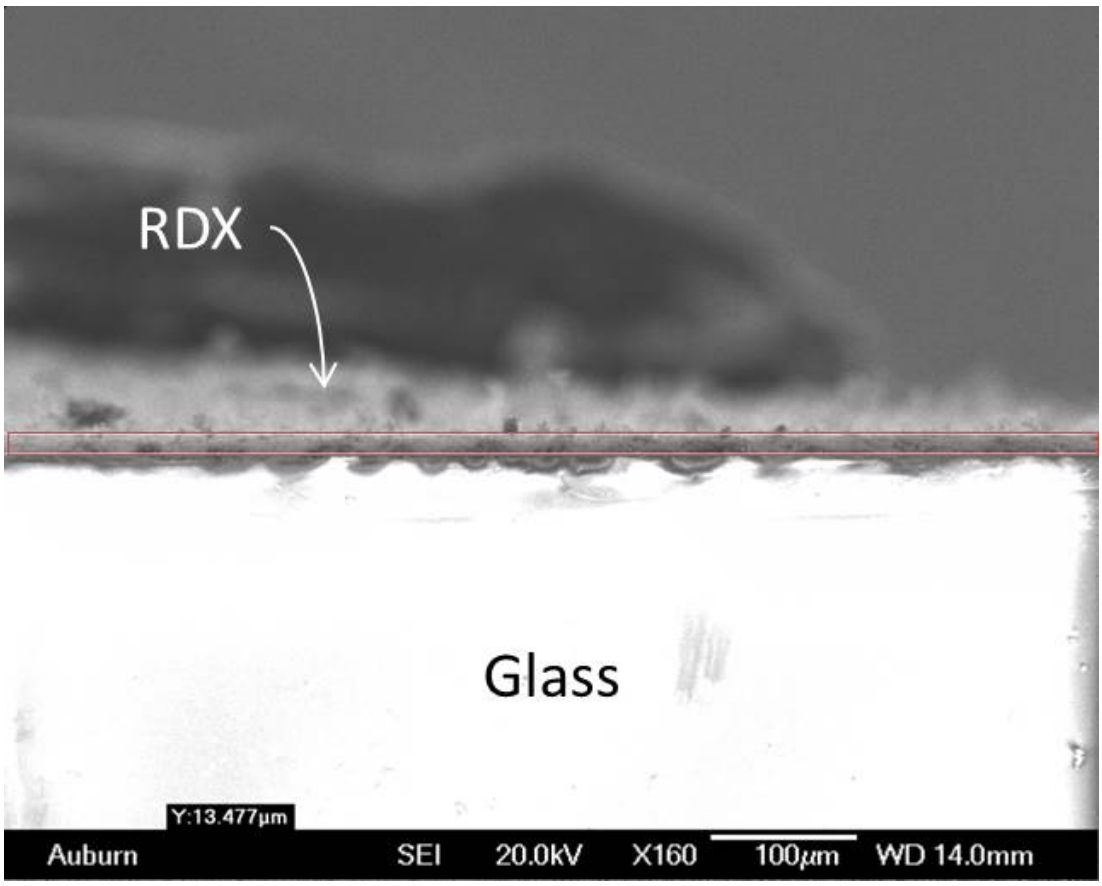

Figure 2.3. Under standard spraying conditions a 5mg/mL solution of RDX in acetonitrile produced a resulting thin film of 13.5 µm (Scale bar = 100 µm)

Optical microscopy was carried out on the CRAIC Microspectrophotometer (Craic Technologies, 20/20 PV™) also allowed the porosity of thin films to be examined. Example microscope images of the change in porosity with capillary to sample distance are shown in Figure 2.4. The top left image was obtained under standard conditions.

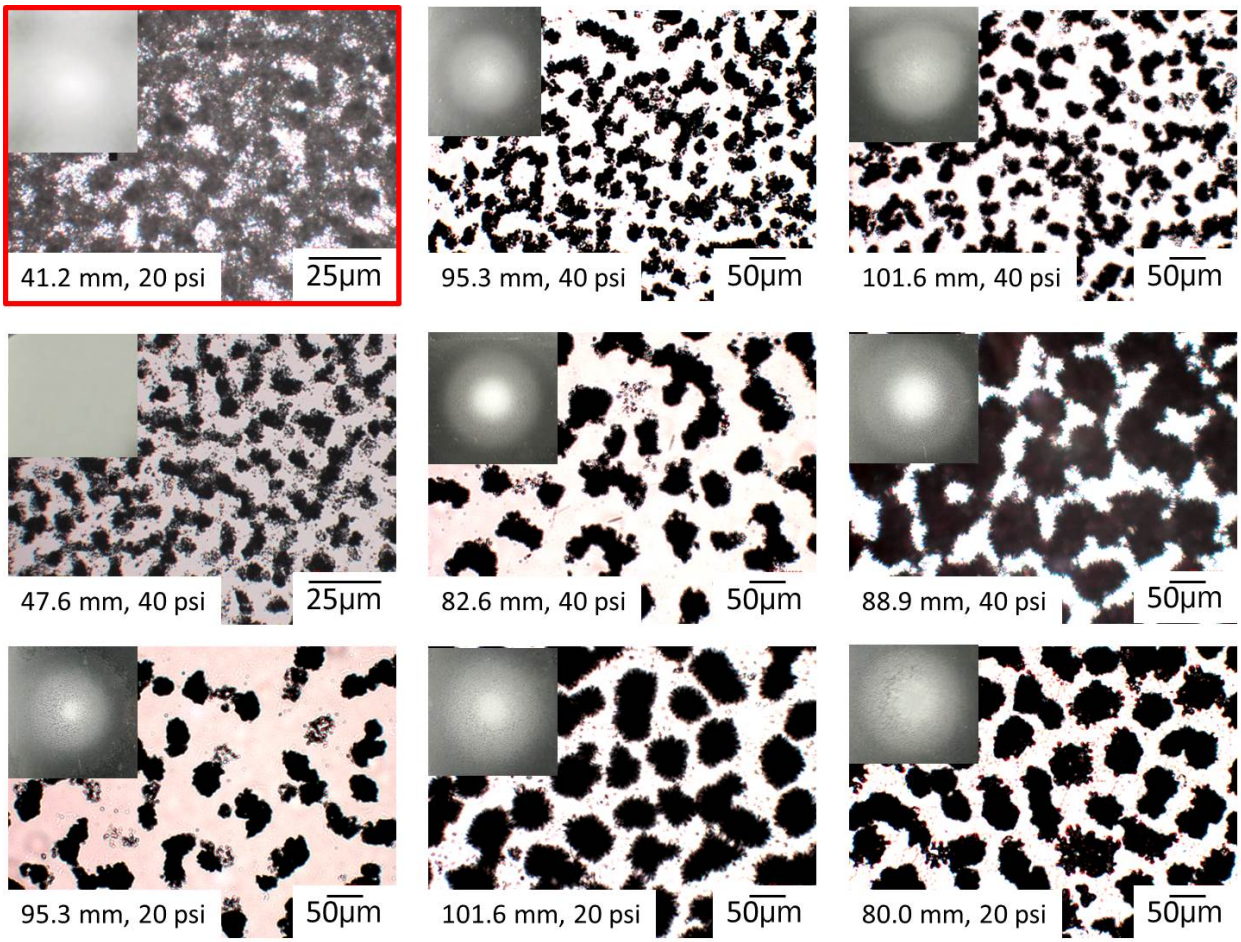

Figure 2.4. Microscope images (large image) indicating a change in porosity with capillary to sample distance and carrier gas flow rate where the RDX (black) and empty space (white) change with conditions. Top left inset image is a 20 mm x 20 mm photograph of resulting film

2.5 Laser pulse control

The laser used for all experiments was a Continuum Inlite III-10 laser system, interfaced through serial input at the computer and the Inlite software.[5] The Nd:YAG was operated at 266 nm with a 6.5 ns pulse and it delivered 50 mJ of energy. The laser could be operated in a 10 Hz repetition rate with 1 to 10 divisions (with a division of 10 it becomes 1 Hz), or in a single shot mode through an external triggering input. The q-switch was always set internally to fire at a 175 μs delay from the flash lamps. The voltage to the flash lamps had to be routinely monitored and occasionally adjusted to ensure that the power was sufficient. The flashlamp voltage was adjusted until 50 mJ was output from the laser which was run at 10Hz and not focused through a lens. The resulting power over time was measured on a Laser Bee power meter which recorded the power over time via USB and the LaserBee software and is shown in Figure 2.5.[6] The voltage was set when the power achieved a steady-state over 600 mW.

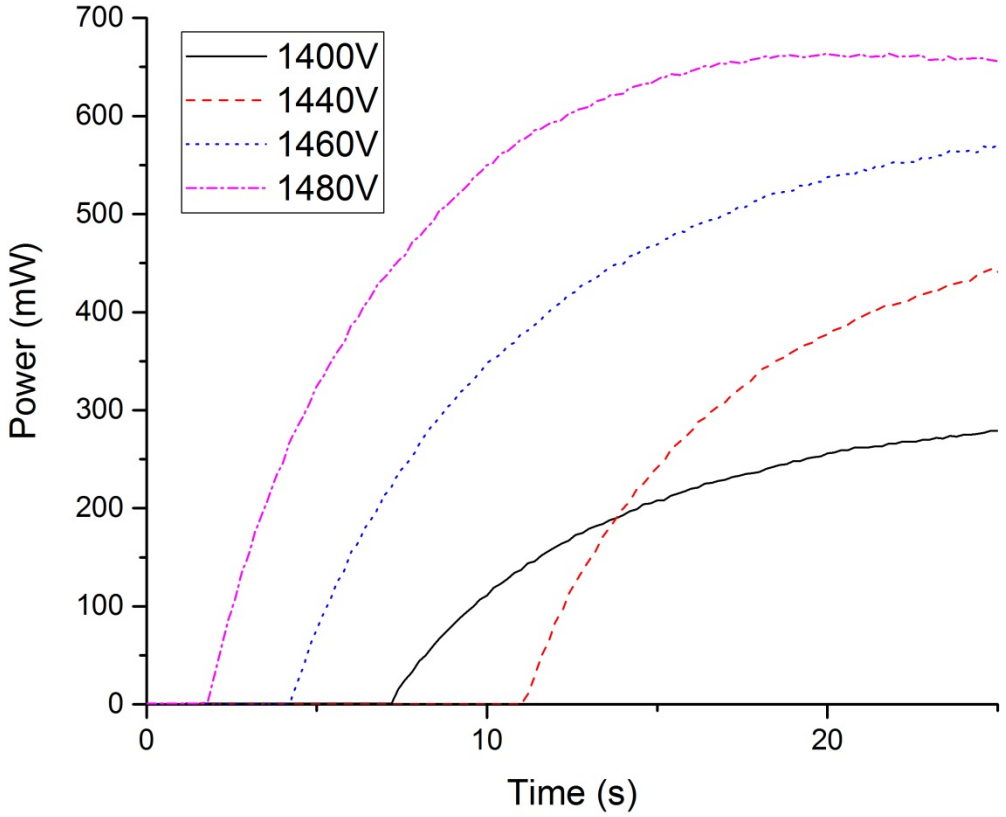

Figure 2.5. Laser power meter measurements showing dependence on flash lamp voltage

2.6 Fast-switching spectrometer

A diffraction grating based spectrometer, which collects and outputs a wide region of the optical spectrum, has been coupled with a fast electronic shutter to collect spectra of laser induced plasma events. This allowed the continuous emission of the spectrum to be gated on a defined time scale so that optical information can be obtained throughout an emission event. The fast electronic shutter (Varo 510-9323-301), the image intensifier (II), is gated in time to allow only light in a specific period of time to be collected by a CCD camera (Sony, XCD-SX900) interfaced with the computer through firewire and Sony IIDC software.[7] Custom programming in AutoIt[2], allows the entire process to be collected automatically by firing the laser, collecting the spectrum, moving the sample, and repeating.

Light from laser induced plasmas was delivered to the spectrometer by collection of the emission by a ball lens (Edmund Optics, 32-748), focused onto the end of a Ø1000 μm, 0.48 NA, 1 m long fiber (ThorLabs, M71L01). The fiber is then positioned by an XY translator in front of the entrance slit (108 μm) of the spectrometer. The diffraction based grating (PG&G 4160) was set to a grating of 150 grooves per millimeter with a blaze of 450 nm, to allow a ~400-1000 nm range of emission to be continuously output through the exit slit.

To gate the detector, the voltage needs to be switched from 300V to 0V in a time period equivalent to that of the desired input signal. The fast optical shutter has a working spectral range of 300-800 nm, though not a uniform transmission. The resulting dispersed light is imaged onto the front metallic cathode window of the image intensifier[8,9] as shown in Figure 2.6. The image intensifier utilizes the photoelectric effect. The photons passing through the quartz window strike the metal cathode ejecting a photoelectron. The cathode voltage is controlled at 0/300 V to gate the photoelectrons from entering the front of the microchannel plate (MCP) where the voltage is

set to 200 V. When there is a period of time that the photocathode voltage is at 0 V, the photoelectrons are accelerated to the more positive MCP where they are multiplied. The gain is set on the backside of the MCP where the potential is set from 200 – 1000 V to adjust the amplitude of signal. The then multiplied charges (1 incident electron generates ~10,000 electrons) are then further accelerated to the phosphor screen anode at 6000 V. The location of where the photons hit the cathode are representative of the wavelength of light, those photoelectrons then strike the phosphor screen emitting a glow at that same position.

The gating electronics and circuit (Figure 2.7), based on a half-bridge driver[10] controls the voltage to the cathode on the image intensifier to gate it on a ~10^{-6} s time scale.

Using a square wave input to IR2111 with a width equal to the desired output, the "Cathode" output of the circuit will switch from 300 V to 0 V and back to 300 V on the time scale of the input pulse. This switching of the voltage for the cathode by this circuit allows the gating of the image intensifier shown in Figures 2.6 and 2.7 and verified on the oscilloscope trace in Figure 2.8.

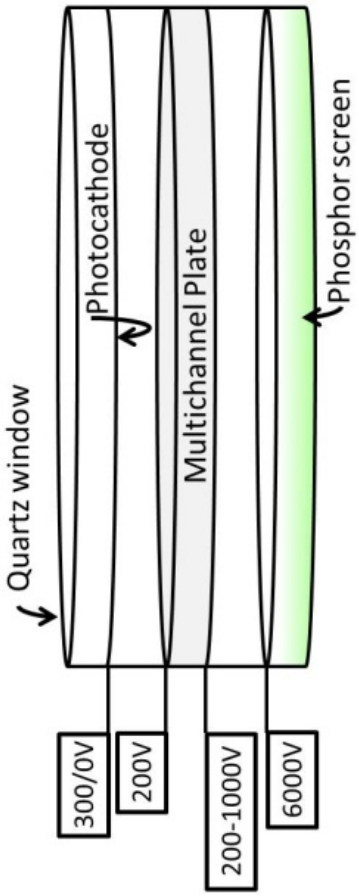

Figure 2.6. Image Intensifier used as fast gated detector

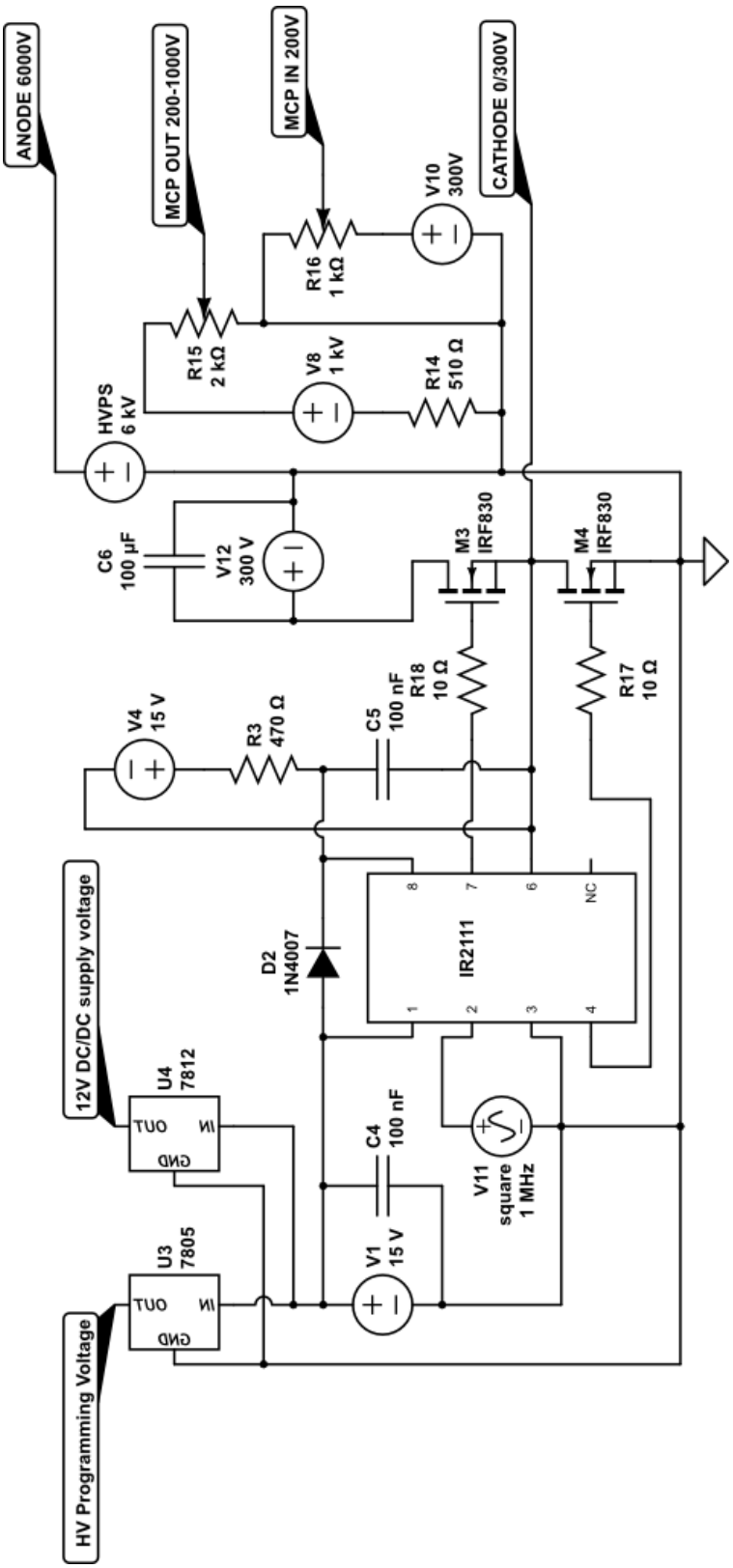

Figure 2.7. Circuit responsible for the control of the image intensifier, the input square wave drives the function of the cathode through the use of the half-bridge circuit

The resulting light from the phosphor screen, on the output of the II, is imaged onto a SONY XCD900 CCD camera that is triggered in sequence with the gated detector. The computer saves the resulting image of the spectrum.

2.7 Instrument calibration

A 1μs exposure time as measured on an oscilloscope is shown to switch “off” and “on” in 1 μs. The “off” state being 0 V in which this is the associated time in which the detector is “on”. There is an inherent 900 ns in the IRF830 n-Channel MOSFET.

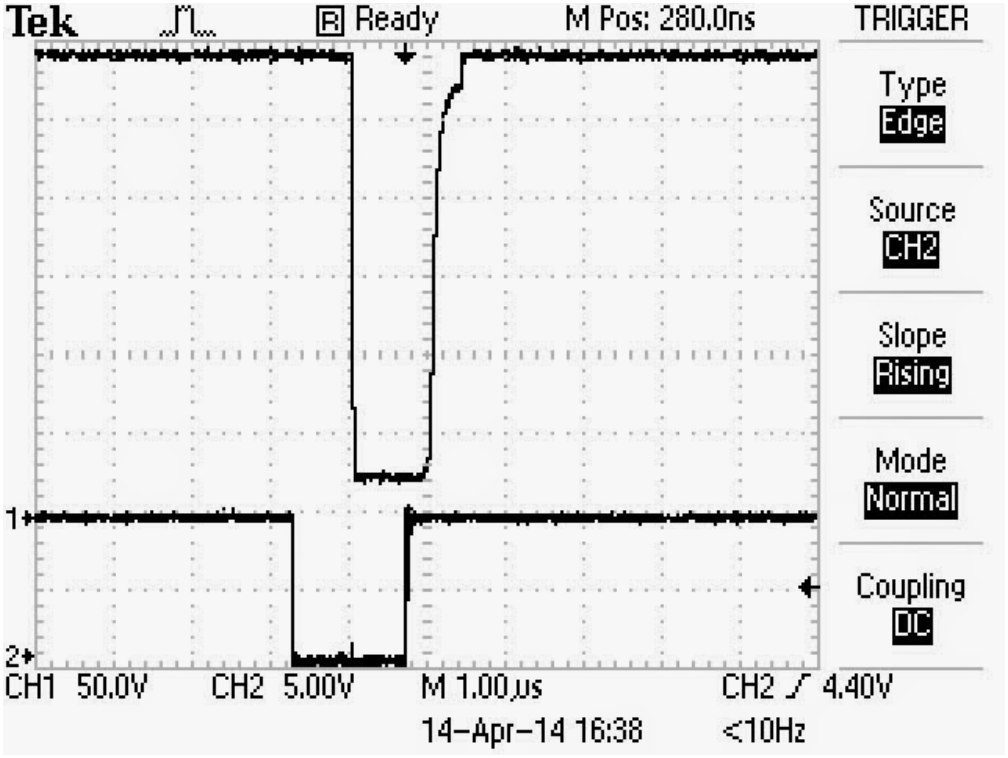

Figure 2.8. Oscilloscope trace of 300V/0V output as measured on the cathode of the II

In order to verify the circuit design and the operation of the image intensifier, the characteristic turn on response was verified. A 1 μs probe laser pulse was walked through the trigger pulse for the image intensifier in 100 ns incremental steps. The turn on and turn off response was verified by a high speed photodiode (Vishay TEMD6200) measuring the light emerging from the phosphor screen of the II and the results are shown in Figure 2.9.

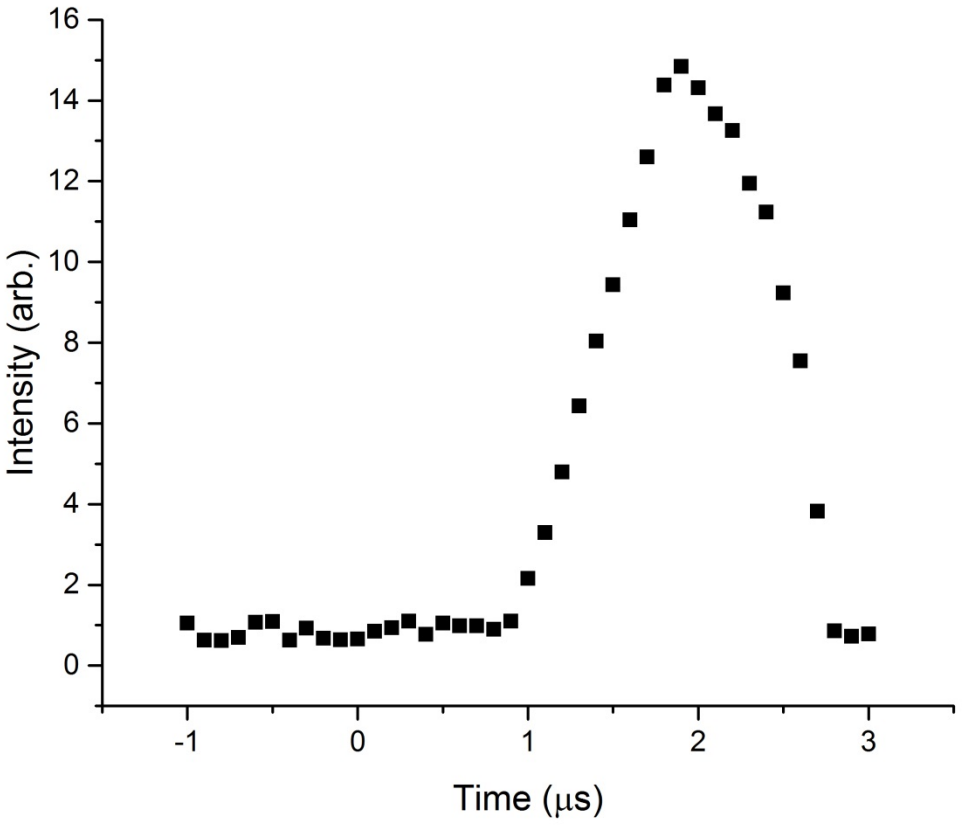

Figure 2.9. Image intensifier turn on / off response

The increase in signal is due to the additive 100 ns of light being incident upon the detector. In the first point, the pulse length is 100 ns, by the tenth point, all 1 μs of light have been imaged by the detector. The turn on response is linear as shown in Figure 2.10 and the non-linearity of the turn off response can be attributed to the residual phosphor glow of the screen.

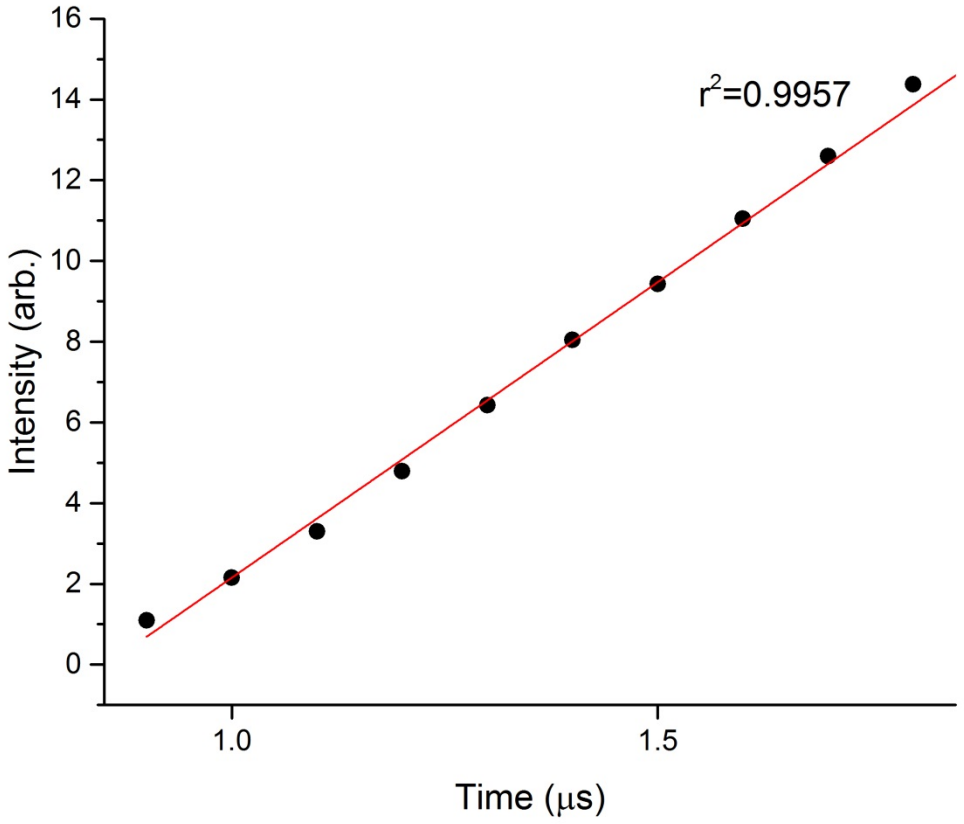

Figure 2.10. Linear turn on response of the II detector verified by walking a 1μs laser pulse through the gate of the detector in 100ns steps

The CCD camera imaged the II which detected the light at each pixel. Calibrations were performed with gas discharge lamps to generate a pixel to wavelength to calibration curve from the relative pixel positions of the known atomic lines of the lamps. Individually, calibration standard gas discharge lamps of hydrogen, helium, and krypton were placed in front of the ball lens and the resulting spectrum was recorded for each as shown in Figure 2.11. The spectral lines for each gas are published and well known.[11, 12] The wavelengths of those peaks were then representative of a pixel location on the resulting light from the II that was imaged by the CCD camera. A calibration curve was established based upon these experiments and is shown in Figure 2.12.

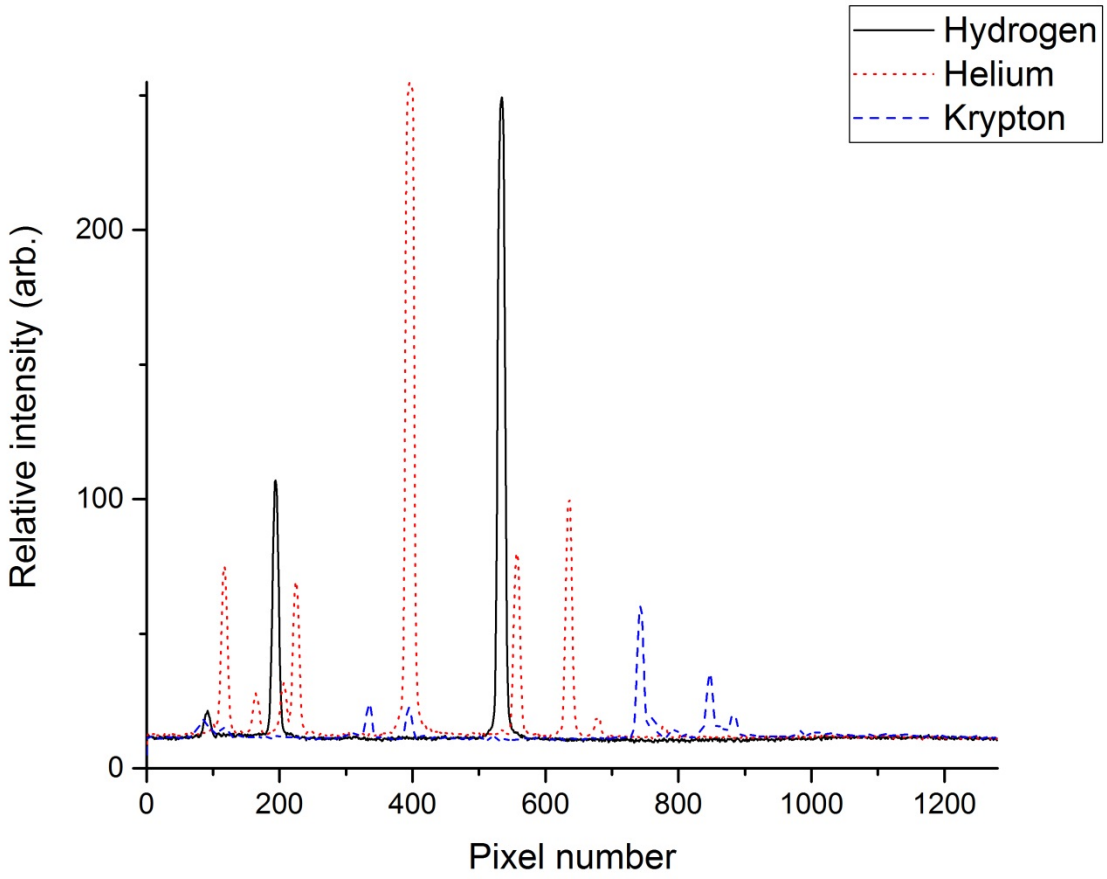

Figure 2.11. Calibration lamps as seen by spectrometer and the corresponding pixel position as imaged by the camera

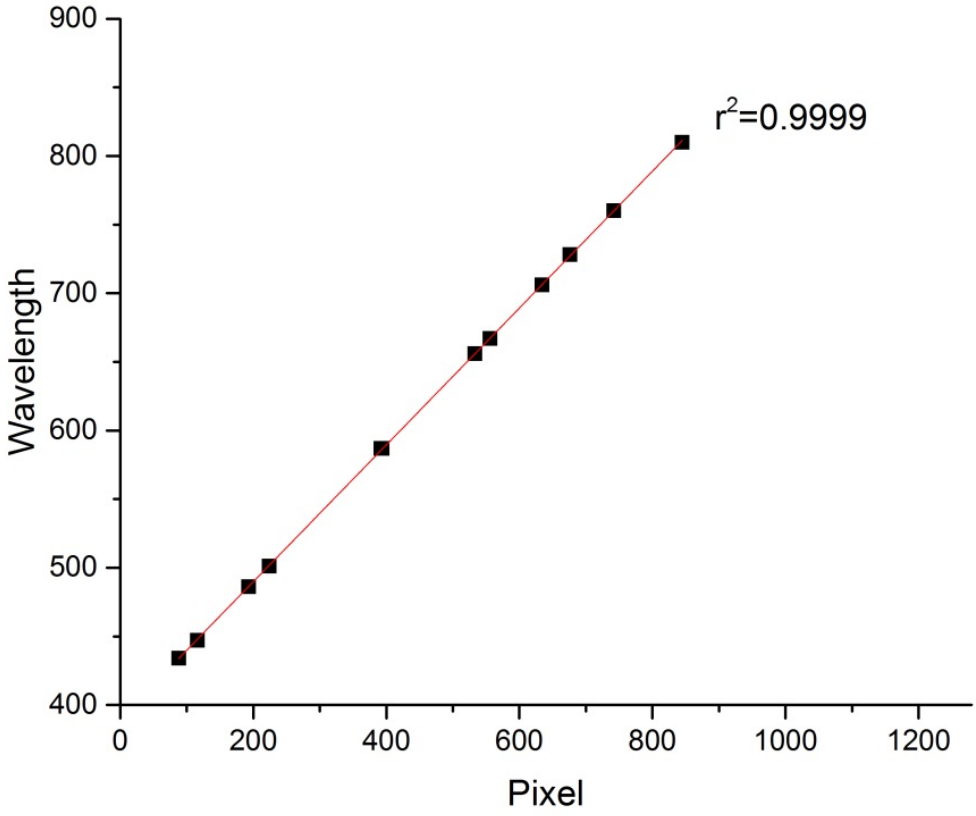

Figure 2.12. Wavelength calibration curve converting pixel position to wavelength as dictated by lamp emission lines with resolution of 0.5nm/pixel

Intensity calibrations were performed by creating a correction to a known emissivity source obtained from Spectrecology.[13] The relative intensity of the calibration lamp as measured on the instrument in comparison to its known values is shown in Figure 2.13 along with the associated correction.

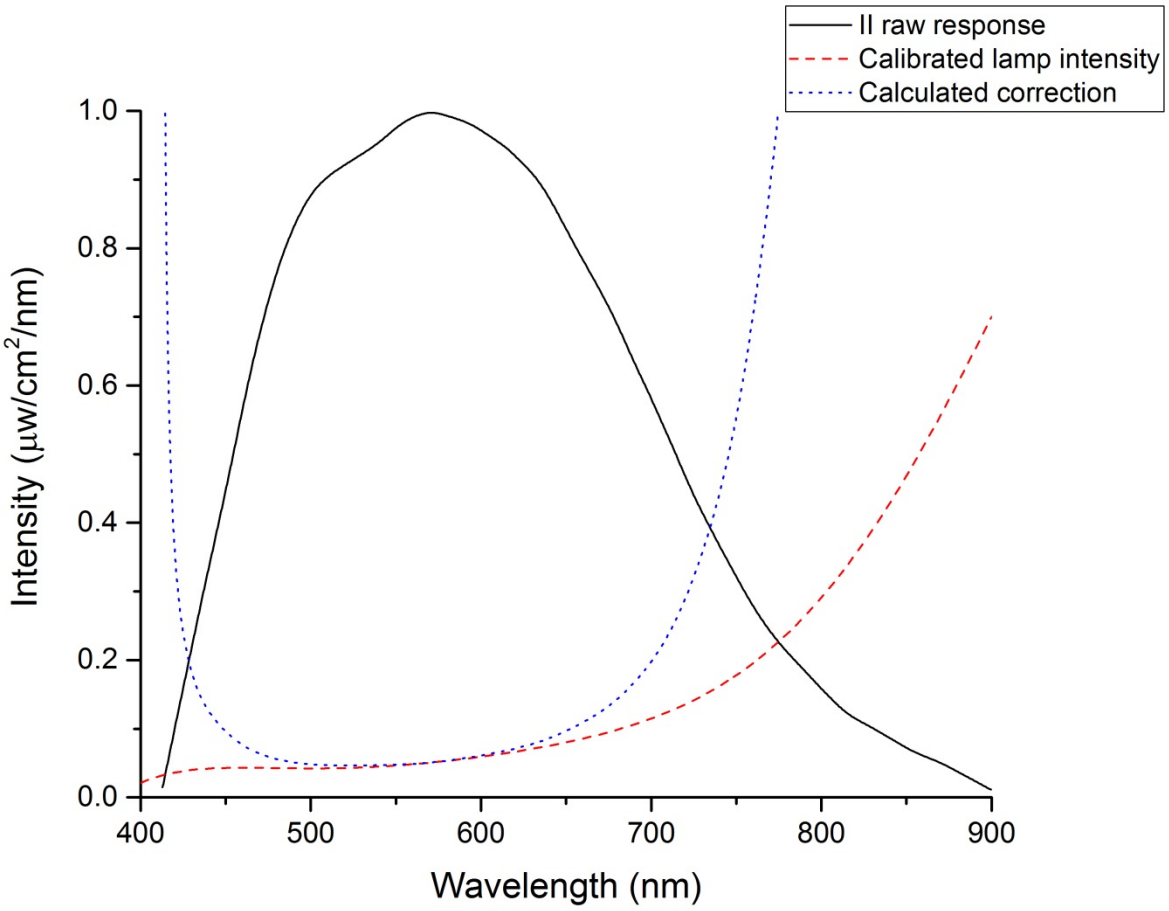

Figure 2.13. Calibration lamp as measured on spectrometer (blue), calibration lamp known values (red), and the correction factor applied to raw data (green)

2.8 Photodiode plasma lifetime experiments

The lifetime of the laser ablation events of the aforementioned samples was measured with an ultrafast photodiode (Vishay TEMD6200). The photodiode has a response restricted to two regions, one within 400-700 nm and the second involving 800-1100 nm. The lifetime of the plasma was determined by measuring the visible emission. To ensure that the IR was not making an additional contribution to the signal, heat absorbing glass (Edmund Optics 49-092) was placed over the sensor on the photodiode to remove all radiation at wavelengths greater than 800 nm. The photodiode was connected to a 9 V battery in series with a 3300 Ω resistor the limit the current. The voltage on the photodiode was recorded with an oscilloscope (Tektronix TDS1001B) that was triggered off of the q-switch to record the visible emission.

2.9 Plasma emission spectra collection

The complete experimental set up is shown in Figure 2.14. The laser is set at 90 degrees from the sample surface as to prevent any plasma radiation from reflecting back into the laser cavity. The beam is then turned 90 degrees towards the sample by the 266 nm specific mirror (Melles Griot Y4-2037-0) positioned in front of the laser head at a 45 degree angle. The laser light then passes through the 120 mm focal length lens located on the x translator as described above, and onto the sample surface along the x axis. The y and z axis of the translator control the sample movement left to right and up and down, respectively.

The photodiode and the ball lens coupled fiber optic cable are positioned at a 45 degree angle from the sample surface on the left and right side of the beam, respectively. The ball lens increases the angle of acceptance of the fiber optic cable. A separate, manual x-y translator is situated on the front of the diffraction grating set up allowing for precise focus of the light onto the entrance slit. The diffraction grating was adjusted to allow for roughly a 400-1000 nm

working range of light to be collected. The image intensifier is positioned at the focal point of the exit slit on the diffraction passing through to the camera. The CCD camera then collected light exiting the image intensifier and through the firewire connection and Sony IIDC software, resulting images were transferred to the computer. The photodiode traces were collected by oscilloscope #2 and transferred to the computer.

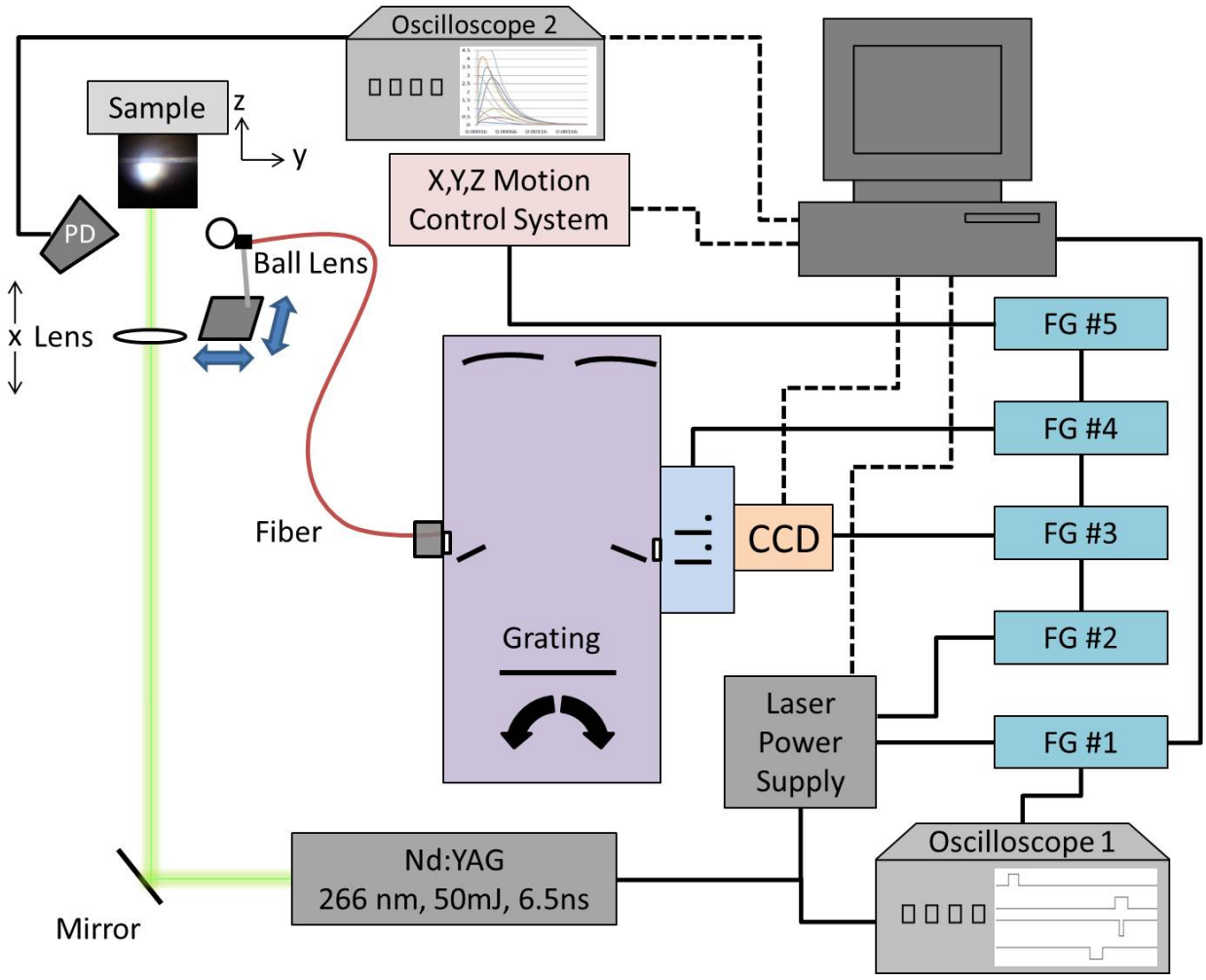

Figure 2.14. Experimental set up showing instrument orientation, driving electronics, and timing control

The heart of the experimental set up is the driving electronics and the timing scheme. The short lifetime of the plasma dictates a need for precision in data collection as related to the laser pulse. All signals were collected on oscilloscope #1 (Tektronix TDS540) to ensure necessary time resolution for collection. The timing scheme is shown in Figure 2.15. The origination pulse from the Sericon[14] computer program initiates the experimental routine (appendix 1). The computer pulse triggers function generator #1 (Wavetek 186) to fire the flash lamps on the laser and 175μs later, the q-switch opens, letting the pulse escape the laser cavity based upon an internal laser delay. The q-switch triggers oscilloscope #2 (Tektronix 10001B) to record the photodiode trace and collect the visible light emission over time. The q-switch also triggers a delay on function generator #2 (Wavetek 95) which can be adjusted to allow for the rest of data collection to take place over any time period. The delay sends a trigger signal to function generators 3 (Wavetek 145) and 4 (Wavetek 166) which trigger the CCD camera to start collection and the II to be gated, respectively. The trigger for the CCD camera is also used to send a trigger signal from function generator #5 (Wavetek 186) to the motion control system in charge of displacing the sample after the data collection is over. This routine may be repeated as many times as required.

Spectroscopic data collection could be carried out manually or through an automated programmed routine. A typical wafer provided data from 70 ablation experiments. Spectra were typically collected in 1, 5, 10, or 20 μs windows. For example, with 20μs windows, a total time range of 0 to 280μs after the laser pulse could be collected. A few sets of spectra were also collected with a 1μs collection window overlapping the laser pulse to see how they differed from later spectra. Multiple experiments were always collected at each delay and exposure to average either 5, 7, or 10 experiments. The gate on the image intensifier was moved accordingly in time

relative to the q-switch as shown in Figure 2.15. The background spectra collection was accomplished by the CCD saving an image of the II during the laser induced plasma event, but with the II always in an “off” state. The resulting wavelength dispersed light was not imaged on the image intensifier so the only light the CCD image recorded as a background was ambient light. Each sample had its own background obtained as the resulting scattered light and intensity was different. All spectra were saved as *.bmp images after firewire transfer through the Sony IIDC software.

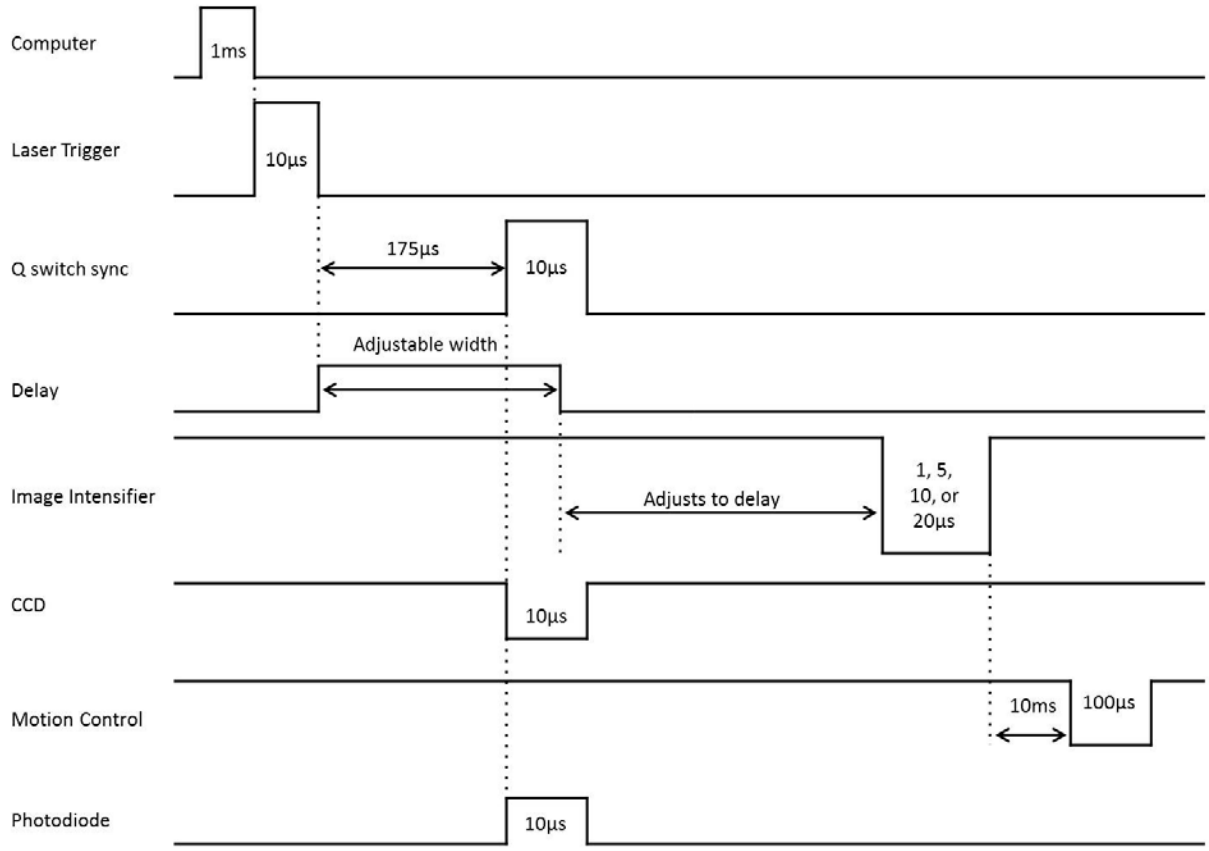

Figure 2.15. Timing scheme of driving electronics for data collection

2.10 Data processing

After a set of given experiments there would be hundreds of *.bmp or *.csv files of spectra or photodiode traces waiting to be processed. Batches of images were processed by ImageJ[15] using AutoIt commands (appendix 1) to convert the images from 8-bit to 32-bit, select a region of interest (constant throughout experiments) and obtain gray values (intensities) for each X-axis pixel. Resulting intensities and pixel values were transferred to Excel[16] where they were combined and calculated to provide intensity and wavelength values for each collected spectra. Background data processed in the same manner was subtracted from raw data to provide resulting background corrected data for further analysis. The oscilloscope traces were imported into Excel through a VBA script that batch processed them to a single spreadsheet for analysis. Plots were made in Excel and Origin.[17]

2.11 References

1. *DMC Smart Terminal*, Galil Motion Control, Inc.: Rocklin, California, 2008.
2. Ltd, A. C. *AutoIt Script*, v3.3.12.0; 2014.
3. Orland, A.; Blumenthal, R., *Journal of Propulsion and Power* **2005,** *21*, 571-573.
4. Hickox, H.; Chamberlain, C.; Casper IV, W. F.; Blumenthal, R., Porosity of RDX films deposited by nebulizing spray technique. In Auburn University: Auburn, AL, 2010-2013.
5. *Inlite*, 1.0.0.0; Continuum: 2005-2006.
6. *LaserBee Laser Power Meter Interface*, 2.1.0.29 Wm; J. Bauer Electronics: 2010.
7. Sony IIDC. In Sony Corporation: 2002.
8. Jaramillo, S. A.; Yates, G. J. In *Quantitative Comparison Of Different Microchannel Plate Image Intensifier Tubes As Nanosecond Light Shutters In Coupled Video Systems*, 1986, International Society for Optics and Photonics: pp 63-69.
9. Sync Lite 2 Image Intensifier http://home.fnal.gov/~cheung/synclite/image_intensifier.htm
10. Woolfolk, T. M., Pulse modulated automatic light control utilizing gated image intensifier. In Google Patents: 1989.
11. Inc., E.-T. P., Spectrum Tubes. In.
12. NIST: Atomic Spectra Database Lines Form. In 2015.
13. Morris, M.; Spectrecology, Owner. In Casper IV, W. F., Ed. 2015.
14. *SeriCon*, 2.8; Softbattery: 2007-2011.
15. Rasband, W. S., ImageJ. In U. S. National Institutes of Health: Bethesda, Maryland, USA, 1997-2014; Vol. 1.48.
16. Microsoft, Excel. In Microsoft: Redmond, Washington, 2010.

17. *Origin*, OriginLab: Northampton, MA, 2015.

Chapter 3

Spectroscopic study of UV laser induced plasma decay

3.1 Introduction

3.1.1 Laser induced plasma formation

The ultraviolet (UV) laser pulse and the resulting photoionization are dependent upon laser wavelength,[1-3] background gas,[4, 5] pressure,[6, 7] laser fluence,[8] and sample material.[9] The UV laser induced plasma (LIP) process takes place through a multi-photon absorption mechanism due to the high energy of the photon in the laser pulse. The first photon in the process excites an electron in an atomic bond to a virtual state. With the second photon, the electron can be promoted to the continuum, which starts the ionization process. When this occurs with multiple photons, bonds will be broken, material will be removed, and a plasma will be formed. The threshold for the ablation in the UV process depends on the fluence of photons incident upon the material. In order for the ionization to be sustained, the second photon to promote the excited electron lying in a virtual state to a continuum must be present before the relaxation process occurs. High laser fluences,[10] the absorptive qualities of the laser pulse, and gases capable of sustaining a plasma are all considerations that must be made when creating LIPs for spectroscopic studies. This is of interest for various spectroscopic techniques involving laser induced breakdown spectroscopy (LIBS),[11, 12] machining applications,[13, 14] medical uses,[15, 16] and in military applications for standoff explosives detection,[17, 18] or plasma propellant initiation applications.[19-22]

After the laser pulse has started the ablation process, this fast change to gaseous molecules creates a pressure gradient near the surface inducing a shock wave.[23] This wave

propagates along the beam path at speeds of kilometers per second. Within this nanosecond time regime, the laser pulse is still incident on the sample surface further ionizing the gaseous ablation products into an optically dense plasma. The time scale on which this occurs is so fast that these changes cannot be temporally resolved, but is depicted schematically in Figure 3.1. The conversion observed is directly from a solid to plasma state. This plasma thus rapidly accelerates away from the surface adding to the force and momentum of the laser induced shock wave that originates from the large increase in pressure.

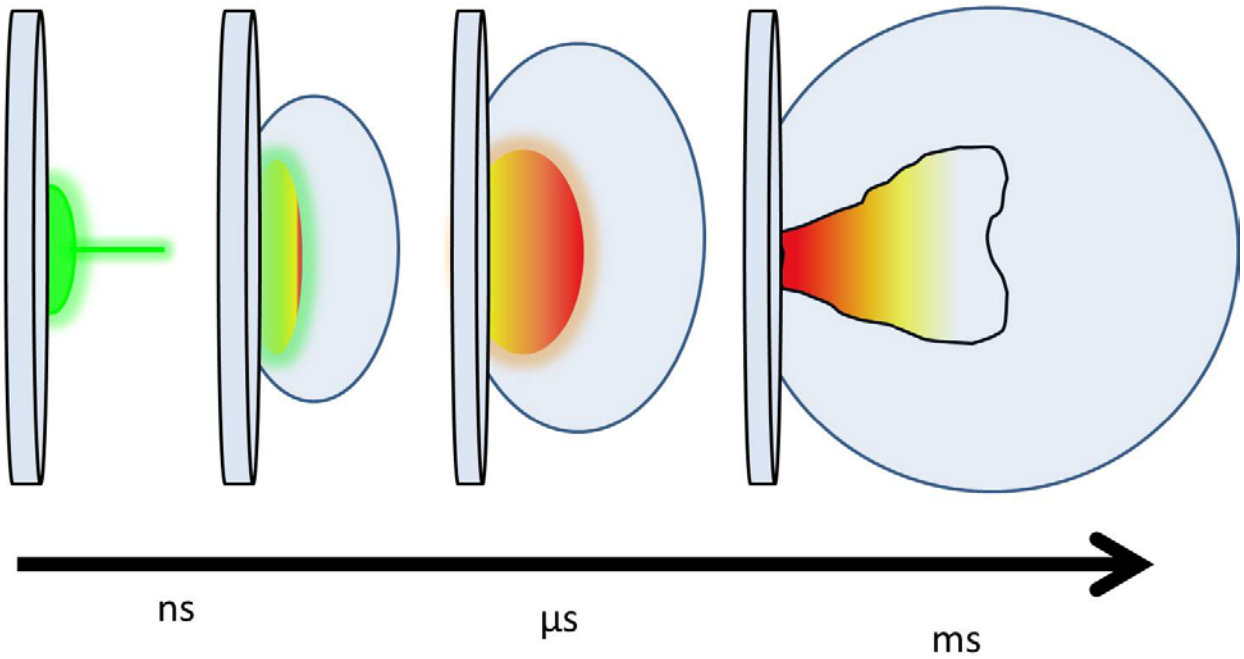

Figure 3.1. Schematic of plasma plume expansion. Left to right: incident laser pulse heating and vaporizing material; gaseous expansion with shock wave formation as plasma starts expanding; further expanding shock wave and heating plasma; shock wave moves through air to its maximum and plasma has started to expand and begin the cooling process

For fluences above a threshold, there is a finite amount of the laser energy that will be used for the formation of an optically dense plasma. Once one has been formed within the first few nanoseconds, the remainder of the pulse energy will be absorbed by the plasma itself in a direct absorption. Therefore laser energy above threshold will go into heating the plasma. The

pulse continues to heat as the plasma expands, but not nearly as fast. The excited electrons and ionic species in the plasma begin to cool radiatively[24] and through recombination mechanisms. [25] The cooling due to expansion ends at the point of maximum expansion, but recombination processes continue as long as the plasma exists.

3.1.2 Plasma decay process

The plasma gas phase transition[26-28] is of interest to understand the dynamics that are occurring during the decay process and the resulting chemical species[29] that are the effect of the LIP process. The gaseous products may be various recombination products from the plasma species or hot accelerated particles from the sample surface that were ejected from the shock waves or sublimed from the radiation of the hot body above it.[30, 31] Study of these phenomena can motivate further understanding into the laser induced plasma processes, and the interactions of plasmas with solid materials.

3.2 Experimental

3.2.1 Sample preparation

Polyethylene (PE) and polycarbonate (PC) 25.4 μm films from McMaster-Carr were used as is and after removing protective film on PC. Sucrose and ammonium nitrate (AN) films were prepared by drop casting concentrated aqueous solutions of each in water onto a 2" borosilicate wafer and allowing the solvent to evaporate overnight to form a thin film of recrystallized solid on the borosilicate glass surface.

3.2.2 Spectroscopy

All laser ablations were carried out with a Continuum Inlite III-10 Nd:YAG laser system, operating at 266 nm, with a pulse length of 6.5 ns and 50 mJ of energy. Three dimensional sample movement was accomplished using a custom Parker-Dadaell 3-axis position system. This

included the x-axis used to move the 120 mm lens to different to sample distances (LSDs). In all experiments the LSD was kept constant at 90 mm yielding a 1.25 mm spot diameter. The y and z axes were used to move the sample to allow for each laser shot to impinge upon fresh material.

Light emission was initially captured by a ball lens (Edmund Optics32-748) placed at a 45° angle to the sample surface. The ball lens transferred the light into a fiber optic cable (ThorLabs M71L01) cable. The other end of the fiber optic cable was in front of the 100 µm entrance slit of the custom built optical emission spectrometer system. A diffraction grating dispersed the light by wavelength at a plane at the exit of the system where an image intensifier was placed. The custom driving electronics described in detail elsewhere (Chapter 2) allowed the resulting spectra to be gated in time. A TTL pulse was input with a width equal to the desired collection time. The driving electronics drop the voltage of the microchannel plate below that of the cathodic window for the specified period of time. Typical collection employed a 20 µs time integrated window that was moved from the beginning of the laser pulse to up to 200 µs after. Five spectra were collected at each delay.

Resulting light emitted from the image intensified detector was captured by the CCD camera and saved to the computer. The entire experimental sequence was controlled by a custom written program that resulted in the laser being fired onto the sample, the spectrum collected and saved, and then the sample wafer moved to expose new fresh material to the next laser pulse.

3.2.3 Photographic imaging of plasma plumes

Photographic images of the plasma plume were collected. With the laser run at a 10 Hz repetition rate, video was collected until the laser broke through the film. Still frames of the video were selected at key points to show the initial formation, expansion, decay, and cooling.

3.3 Results & Discussion

3.3.1 Spectra analysis

Resulting spectra over the course of the first 240 µs are shown below in Figures 3.3 – 3.6 where each spectra is representative of an average of five laser shots at the specified delay after the laser pulse. All spectra are spatially and temporally averaged over the 20 µs collection window through the ball lens. In all cases, the initial 20 µs has the largest amount of radiation present. This is indicative of the highest electron densities and highest temperatures. In general, there is a relative decay in intensity with time in the four spectra of polycarbonate, ammonium nitrate, polyethylene, and sucrose. The decrease in overall intensity with time is most likely due to the volume of the plasma decreasing with time. At the point of maximum expansion, the plasma intensity is greatest due to the size of the radiating body being at its largest point. The intensity of the plasma then decreases with volume as the plasma decays when material is removed as described by Figure 3.2.

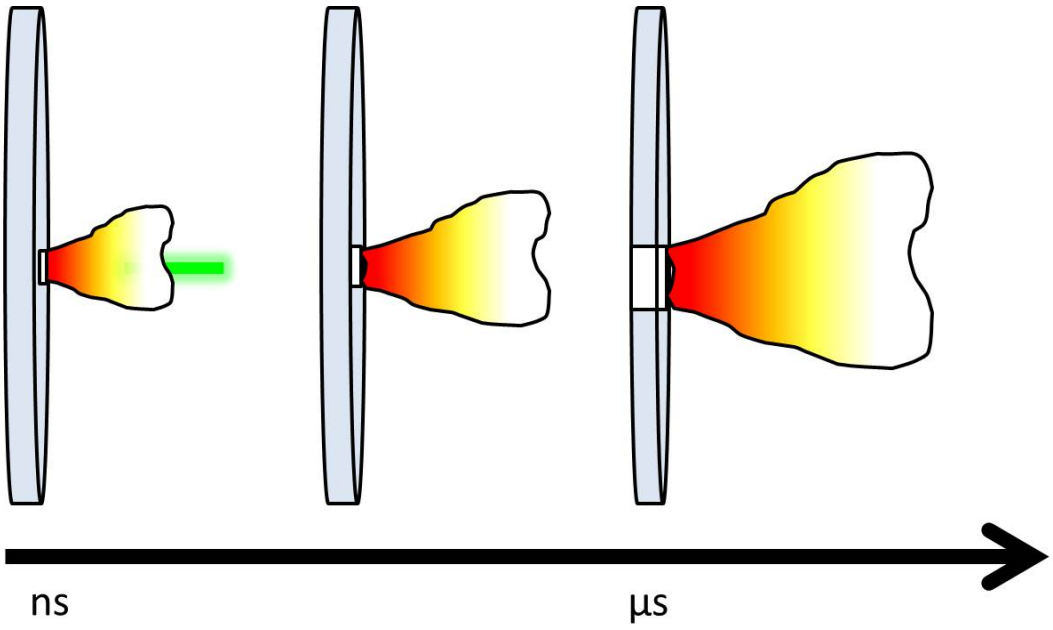

Figure 3.2. Process of laser ablation material removal showing laser plasma heating, plasma plume expansion and material removal through ionization

3.3.2 Polycarbonate spectra

In Figure 3.3, polycarbonate is the only material that shows any significant ionic species present. The C_2 swan bands[12, 32, 33] can be seen at 437, 470, 510, 554, and 610 nm. At 767 nm, signal of a carbon ion[34] is present. The swan bands persist for approximately 60μs and are sitting on top of a background continuum radiation. The first 20 μs shows the greatest signal of these peaks and also the presence of absorption of the peaks as seen by the derivative shape tangential to the peak. The plasma being a hot radiating body is emitting energetic carbon species, but they are also recombining and reabsorb into the plasma simultaneously. This is due to the ablated carbon species being in such a high concentration in the plasma that they are also reabsorbing the emission of the species at these wavelengths. The emission from the other samples shows no evidence of C_2 swan bands at this fluence; this suggests that there is not a significant enough amount of energy capable of producing the molecular and ionic species. Thus, PC has a lower threshold to ablation than the other carbon – containing materials; a lower electronic barrier for the excitation of the electrons into a continuum.

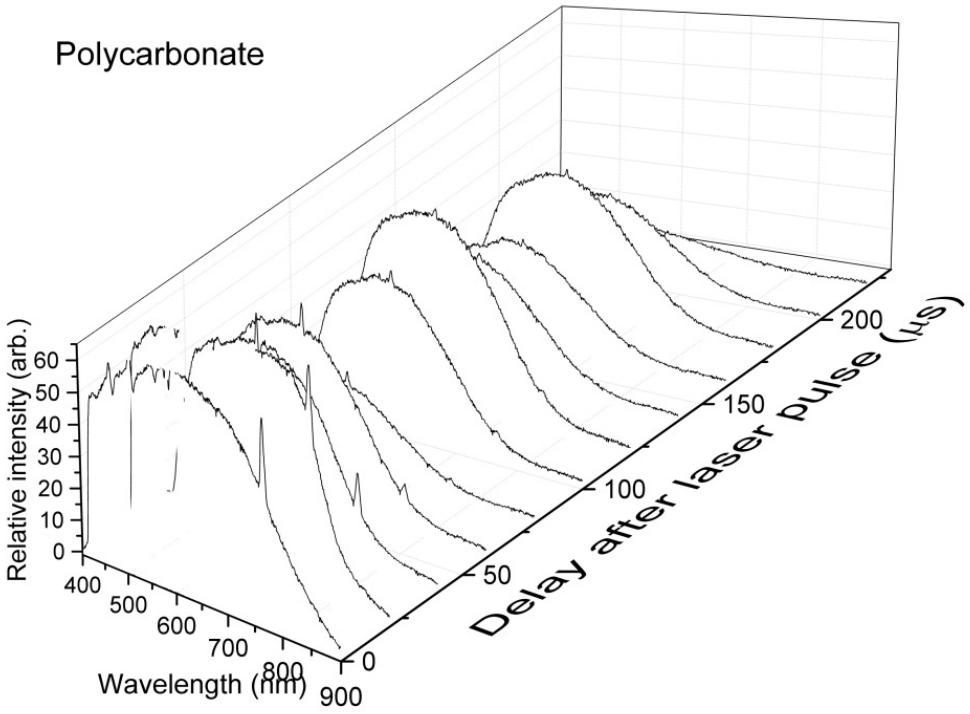

Figure 3.3. Polycarbonate spectra over time

3.3.3 Ammonium nitrate spectra

The spectra of ammonium nitrate are shown in Figure 3.4 to be of similar intensity to polycarbonate. The broadband continuum persists in observable levels for the duration of the experiment. It has a broad presence across 400-700 nm. The long wavelength edge falls off in time to leave a broad peak. The spectra grow and shrink in intensity over this time period which could be explained by dynamic plasma volume. The plume is changing spatially over time. Additionally, the lack of spectral lines suggests that the electron density was so great that the recombination dominates and only emits a continuum. This could be indicative of the recombination processes occurring on faster time scale than any observed atomic or ionic species.

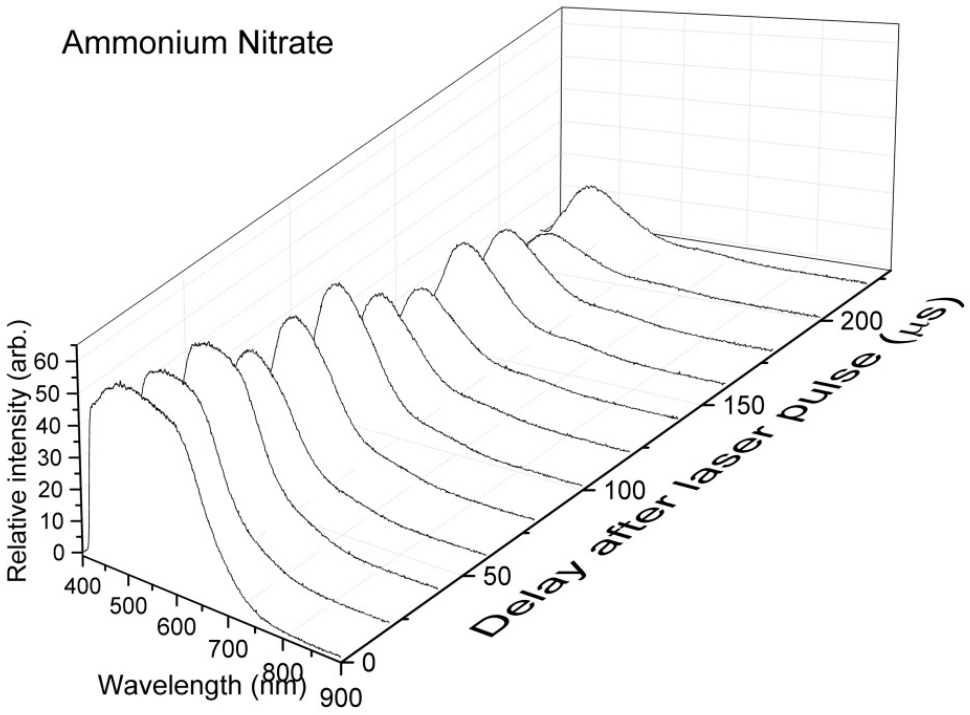

Figure 3.4. Ammonium nitrate spectra over time

3.3.4 Polyethylene spectra

In Figure 3.5, the polyethylene spectra is shown to have only a significant emission for the first 20 µs. Unlike PC and AN, there is no broadband emission for the remaining 220 µs of the experiment. The broadband emission that is observed is very sharp in nature with a steep slope that decays significantly before 600 nm, and a secondary structure that is present from 600 – 750 nm. This could be a presence of a secondary emission feature dissimilar to the feature that is driving the emission at shorter wavelengths. The lack of spectral lines again suggests a high electron density that is causing the recombination processes to dominate not allowing individual species to emit. The most significant observation of PE in comparison to the other samples is the short lifetime of the observed emission. After the first 20 µs there is no further emission observed. This is most likely due to the ablation threshold of PE. With such a high threshold, the only significant plasma that is formed and capable of emitting radiation that is detected is that which is formed in its strongest point within the initial formation where the laser pulse is still present to heat it. The resulting plasma after this time frame has cooled and collapsed so quickly that it cannot be sustained.

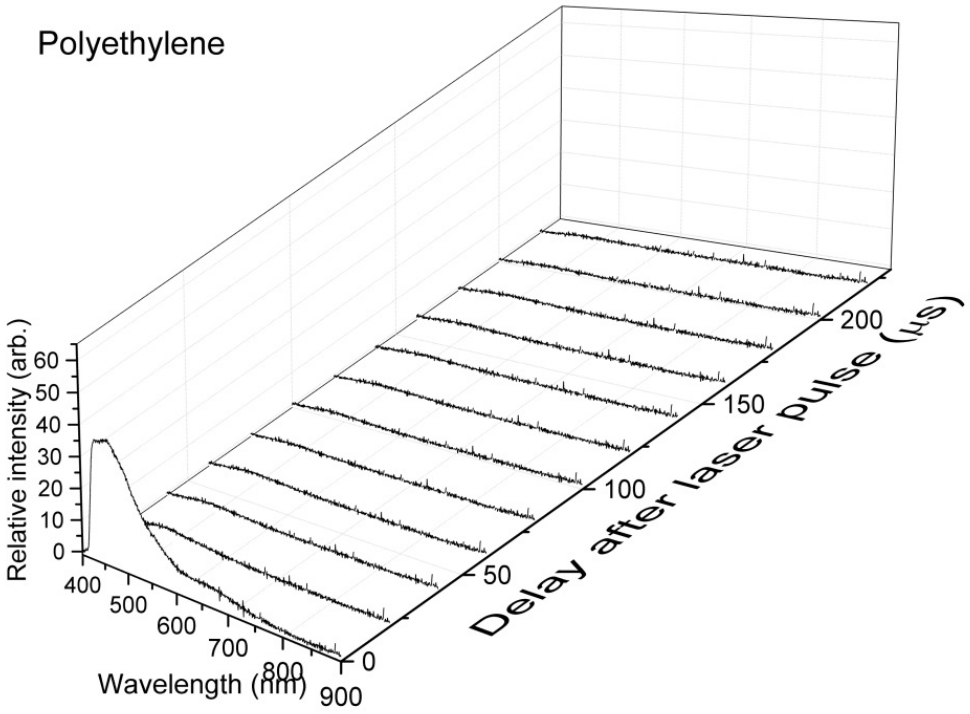

Figure 3.5. Polyethylene spectra over time

3.3.5 Sucrose spectra

Sucrose, in Figure 3.6 shows emission characteristics similar to polyethylene. The sucrose spectra show a strong broadband continuum from 400 to 800 nm. There are however what appear to be two distinct portions, or a shoulder, around 650 nm present only in the first 20 µs. This could be due to two distinct emission sources as the plasma is temporally resolved. The decay of the large continuum decreases significantly and appears to reach a steady state after 40 µs. Again, the lack of any atomic or ionic lines suggests a high enough electron density to allow the recombination to be the significant emission source rather than any specific emitting species.

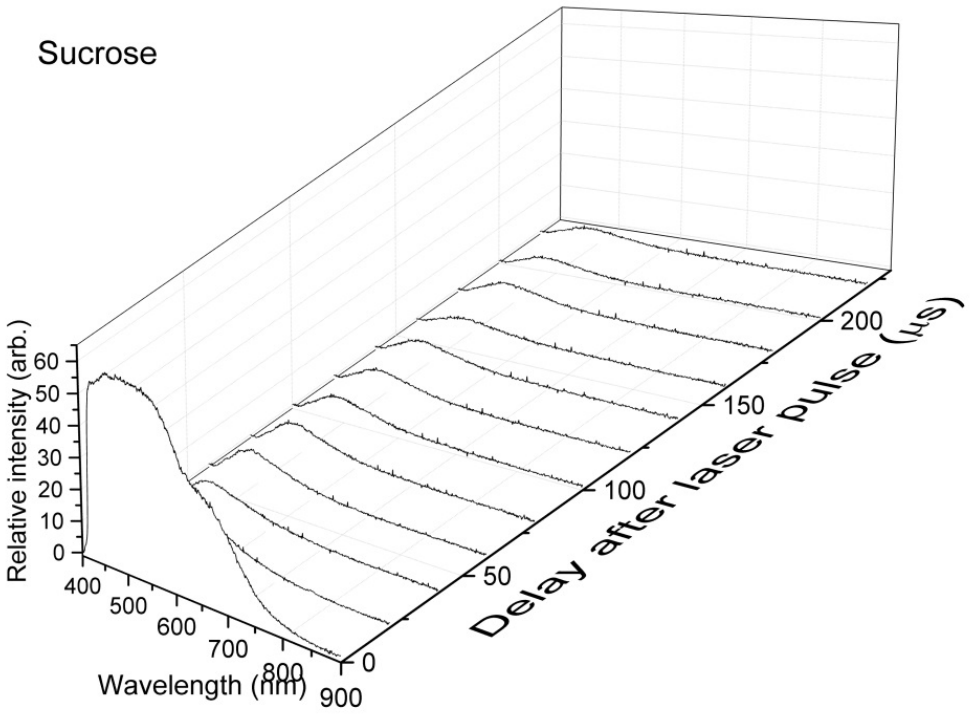

Figure 3.6. Sucrose spectra over time

3.3.6 Continuum radiation

The continuum radiation is present in all samples studied. The source of the radiation is a complex issue. In PC it persists for the longest time. The lifetime is observed in greatest duration for AN, PC, sucrose, and lastly PE. This trend then also can suggest an order of ease of ablation; or rather PC has the lowest threshold and PE the highest. The intensity and propensity of signal in the spectra is indicative of the ability of the laser pulse to convert that material to a plasma state.

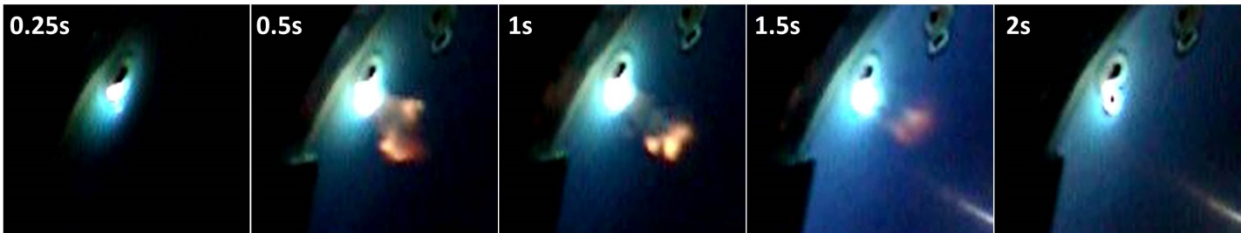

Figure 3.7. Still frames from video evidence of laser induced plasma as collected on polyethylene at a 10Hz laser firing rate

The images in Figure 3.7 are still frames of the video. As these were collected at a 45° angle to the sample surface, there is an angular dependence to the observed images that must be taken into account. The bright white region is where the laser pulse is incident upon the material and the plasma formation occurs. Dark spots are holes from previous experiments. The images were taken as still frames from the video at the approximate times indicated while the laser was continuously firing on the sample. The images from left to right show the initial plasma formation from the 3. As the laser pulse continues to heat the plasma at 5 laser pulses, it expands and reacts with ambient gases in the air. With continued laser radiation, there is further expansion as the material and the plasma are continually heated at the 10^{th} laser pulse mark. Eventually, at around 15 pulses, there is a cooling as the plasma is not able to be sustained due to loss of material. At some point before the 20^{th} pulse, there is a breakthrough of the film as

evident by the black dot indicating a hole has formed and no more plasma is evident. Of note is the variation in the shape and form of the plasma from 0.5 s to 1.5 s.

The source of the background continuum radiation is multi-faceted.[35, 36] Even while the ionization of the material is still taking place, the laser pulse is heating the electrons, which are involved in constant collision processes with the material and ionic species. The emitted radiation could arise from any combination of blackbody radiation, with ionic, atomic, or molecular species emitting at their specific wavelengths, along with other re-combinative radiation. Attempts to fit the data to a simple blackbody were unsuccessful implying that the observed radiation is not simply of one kind, but results from a combined process.

3.3.7 Blackbody radiation model

There is however evidence of blackbody radiation at later times at least in polycarbonate. Blackbody radiation is defined by Planck's law in equation 3.1.

$$I(\upsilon, T) = \frac{2h\upsilon^3}{c^2} \frac{1}{e^{h\upsilon/k_B T} - 1} \quad (3.1)$$

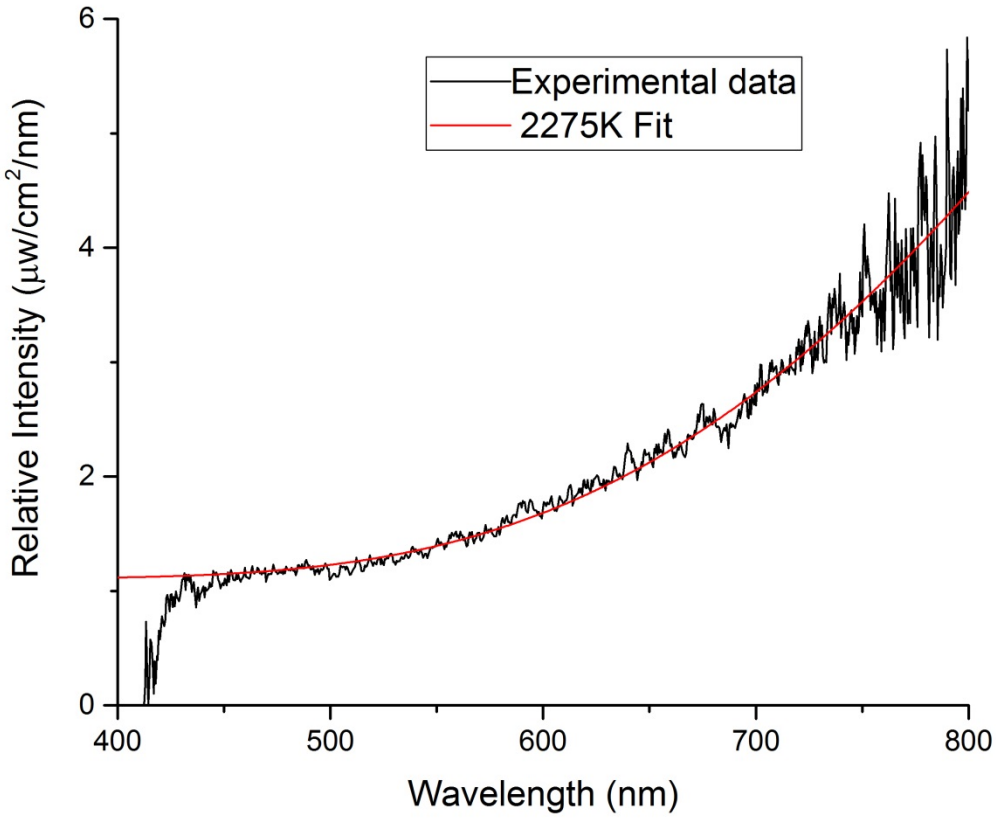

Figure 3.8. Blackbody fit of polycarbonate at 200 to 220μs

After correcting the measured spectra for the relative intensity at each wavelength based upon a standard light source,[37] a least squares fit was made of Planck's equation (3.1) to polycarbonate data at a 200 μs delay resulting in an estimated 2275 K hot body (Figure 3.8). This estimate is consistent with previous results,[5, 38] for a relatively cool plasma. Unfortunately, these late-time polycarbonate spectra are the only collected data that fit to this model. For such fits, the assumption was made that the temperature was such that $\frac{h\nu}{k_B T} \gg 1$. This assumption allowed a temperature to be approximated based upon the negative slope of the following equation.[12, 13, 39, 40] From Planck's equation (3.1), where $C_1 = {2h}/{c^2}$ and $C_2 = {h}/{k_B}$, a natural log plot could be made.

$$C_2 \upsilon = -T \ln\left(\frac{I}{\upsilon^3}\right) - \ln C_2 \quad (3.2)$$

In Figure 3.9, the natural log plot of the spectra yields a straight line in the wavelength regions where Planck's law fits the data. This defines regions of the spectra, and times within the collected data for each sample, where blackbody radiation is present. The slope of this line then will give an approximation as to the temperature in accordance with equation 3.2.

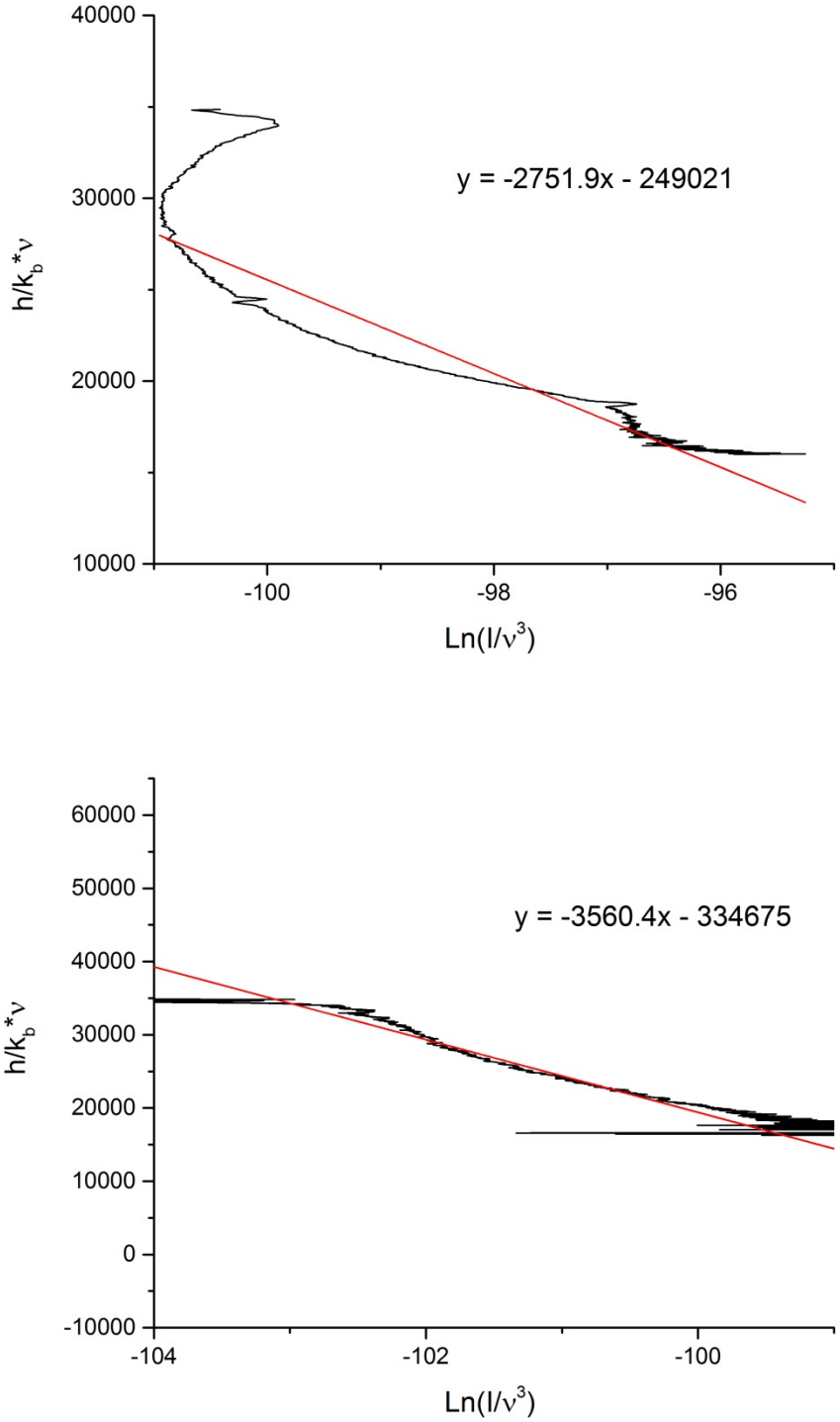

Figure 3.9. Example plots of a linear fit to solved Planck's equation for an early (0μs top) and a late (200μs bottom) time polycarbonate spectrum. The blackbody contribution of the temperature is thus given by the slope

3.3.8 Plasma density

From the data collected, only the plasma density can only be estimated. The lack of any significant atomic lines[41, 42] limits the amount of analysis that can be done to calculate electron densities on this time scale. There is a very short lifetime of emission lines in any of the samples studied aside from polycarbonate, which exhibits also the brightest and longest lived emission. The short lifetime of the C_2 swan bands in PC, and the lack thereof in other samples, can be evidence of recombination that is occurring and is then limiting the lifetime of such species. Free electrons in the plasma must be in such a high concentration that they are readily interacting with the ionic species on a very short time scale, not allowing the ionic or atomic species to persist for any significant time, and thus not showing signals in the emission spectrum. This then suggests that the continuum is present due to the large degree of free electrons.

The lack of ionic and atomic spectral lines suggests that the electron density is high. Previous work has shown rough estimates, of electron densities based upon radiative recombination $A^+ + e^- \rightarrow A + h\nu$ for ions, electrons, atoms, and photons respectively.[43] The large reaction rate can be understood using: $\frac{dn_e}{dt} = \alpha n_e n^+$ where the recombination constant α is on the order of 10^{-12} for ionic species. Since there is a lack of atomic and ionic emission lines, it can be assumed that there is not a significant net charge to the plasma at this measured point. In previous work, the plasma lifetimes were estimated to be about 100 ns, giving an electron density of ~10^{19} cm^{-3}.[44] Here, the plasma lifetime is 100-200 μs which would yield an electron density of ~10^{16} cm^{-3}. The experimental set up for the spectroscopy measurements spatially averages the plasma over the sample collected. This neglects any inhomogeneity that may be present and assumes that the entire collected spectra are then representative of the plasma body. This assumption is most likely not to be correct because on the microsecond time scale, where

the plasma is decaying, these processes will not have any time to reach an equilibrium or stabilize in a homogenous form. By temporally averaging the spectra over the 20 μs time regime, any inhomogeneity to the plasma body is then lost in the spectral measurement.

3.3.9 Decay in plasma shape

The plasma as observed is a hot radiating body of energy. In the presence of air, it can only be sustained for a period of time before decay and cooling begins to take place as it loses energy to its surroundings. The plasma cools as it expands and the recombination processes occur. In a blackbody, there will be an exponential decay in temperature with time, and a shift of the maximum wavelength to longer, less energetic portions of the electromagnetic spectrum. Within each set of spectra in these experiments, for any given sample the shape of the curves does not shift in wavelength. Normalizing the data shows this effect across all time frames. It therefore must be assumed that some degree of steady state temperature has been reached. This suggests that there may be a phase transition occurring once the final state of the spectra has been reached.[45, 46] After this point, the only variation in the spectra is the intensity. For a blackbody radiation source, the intensity varies with the surface area of the blackbody. The surface area will change, decreasing in intensity as the plume decreases in size, but still keeping its relative shape. The point at which the steady state shape arises is different for each material. For PC, AN, PE, and sucrose these are approximately 70, 60, 40, and 50 μs, respectively.

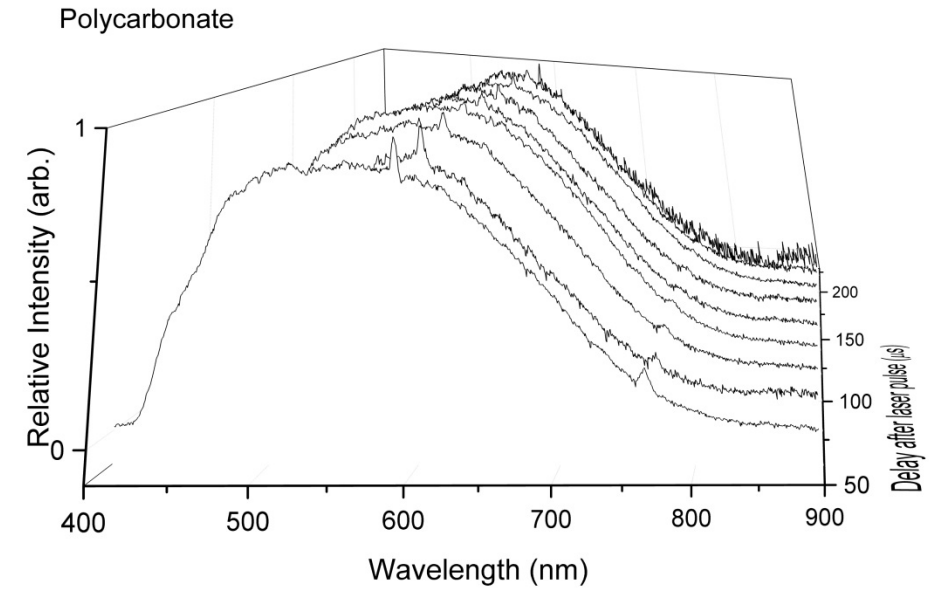

Figure 3.10. Normalized and time-resolved spectra of polycarbonate

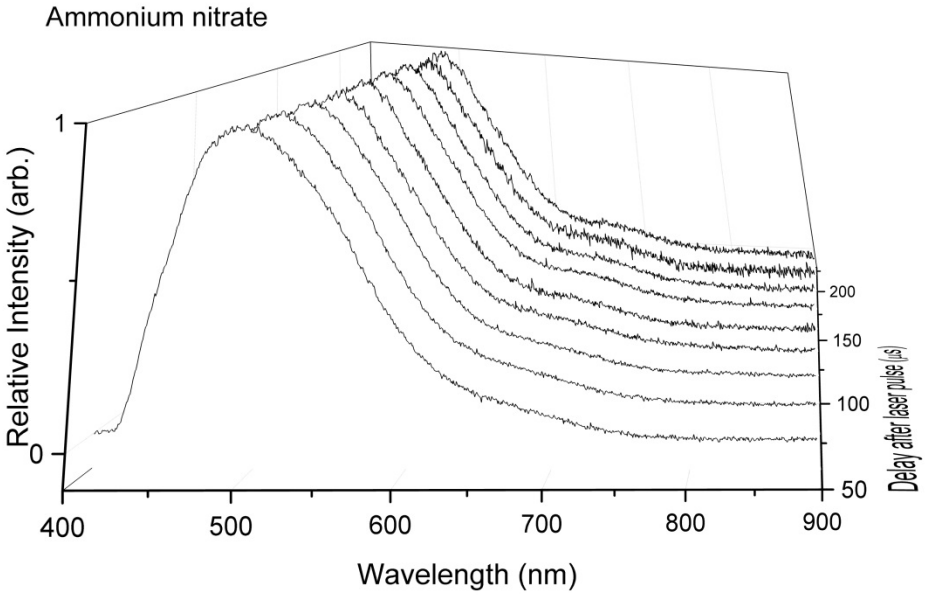

Figure 3.11. Normalized and time-resolved spectra of ammonium nitrate

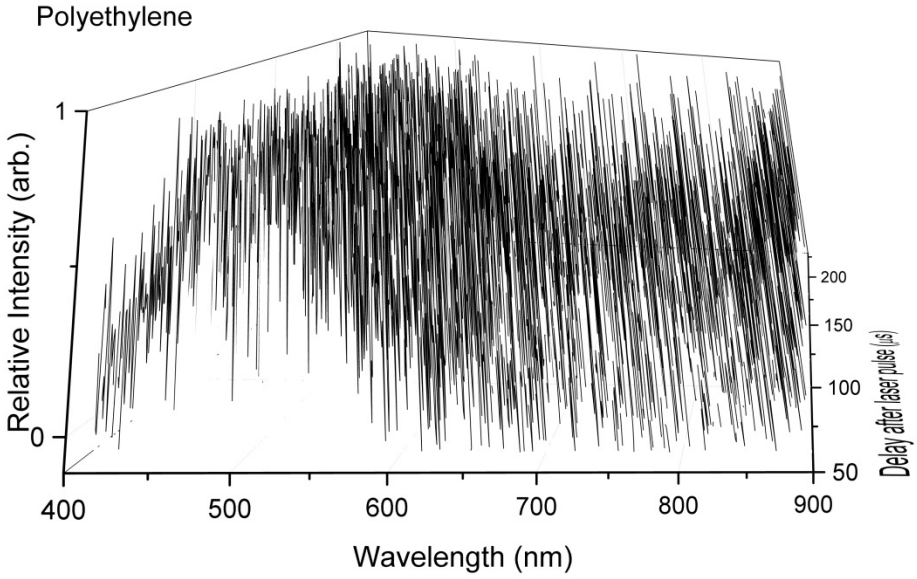

Figure 3.12. Normalized and time-resolved spectra of polyethylene

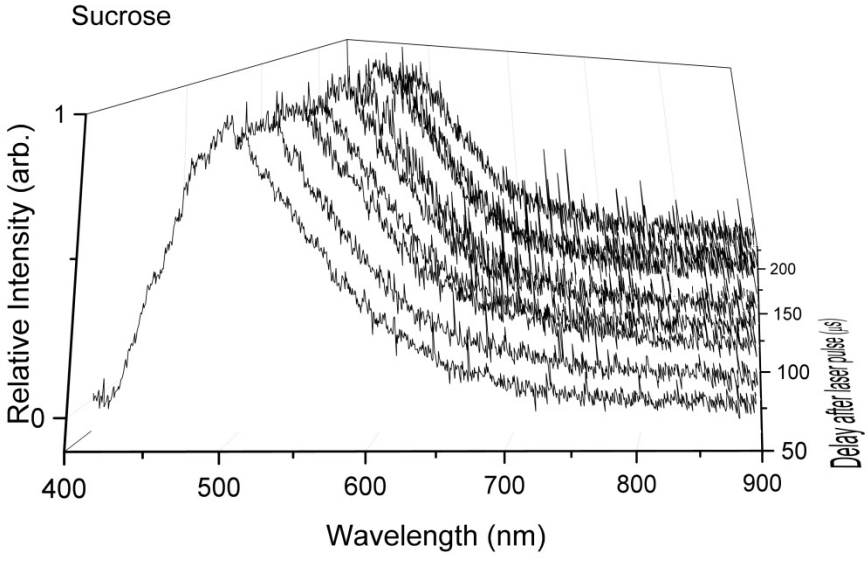

Figure 3.13. Normalized and time-resolved spectra of sucrose

The spectra shown in Figures 3.10 to 3.13 are normalized to the maximum area of the curve for each sample. The decay of the plasma species to a point in time at which the transition from a plasma to a gas is evident. In all of these cases, a single shot from the laser pulse, which lasts only 6.5 ns, induced the plasma formation. The radiation from the plume has only enough energy to sustain itself before the species recombine and cool. Once the plasma has cooled to a significant degree, the visible radiation will undergo a change as shown in Figure 3.5. The maximum electron densities and temperatures are greatest in the time-integrated spectra of the first 20 μs. If the plasma were cooling radiatively, its temperature would be expected to decrease. This is not observed. Instead, the shape of the plasma reaches a steady-state, suggesting that a constant temperature is reached during the last ~150 μs. In this time range, the spectra decrease in intensity. The change in shape is indicative of a cooling to a gaseous state at constant temperature. This is the observed plasma to gas phase transition.

3.4 Conclusion

Plasma plumes induced by a UV laser pulse were studied through optical emission spectroscopy over the first 240 μs. In most all materials studied, a broad continuum of radiation is observed. This radiation does not fit to a blackbody shape during the time that the plasma must presumably cool. The likely observation of the continuum radiation then is the decay of the plasma species into a gaseous state. There is no shift in the continuum radiation as would be expected in a cooling blackbody suggesting that radiative cooling processes are not observed. The observed emission spectra are therefore observations of laser induced plasmas undergoing a phase transition to a cooled gas. As the optically dense plasma radiatively cools and recombination continues, the inner hot plasma core decreases in volume. The steady-state is observed in the spectra because the skin of the optically dense plasma is what is observed

spectroscopically through the thick surrounding gas that it cools to. This process is depicted in Figure 3.14 below as the observed plasma to gas phase transition.

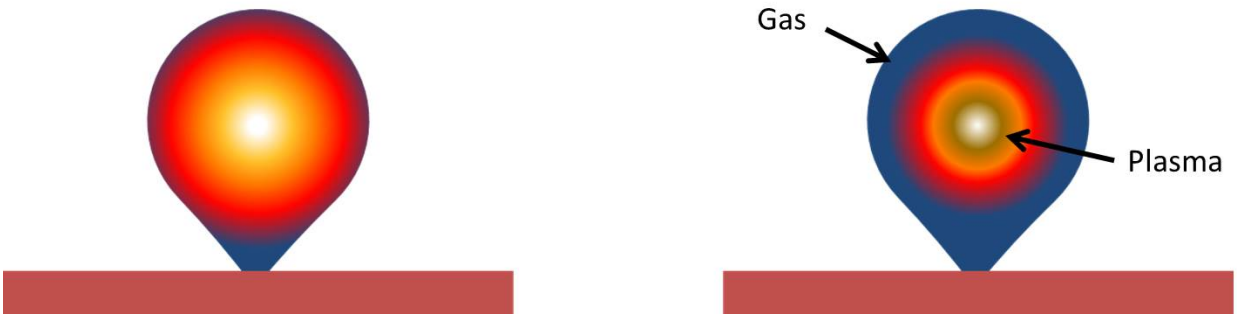

Figure 3.14. Schematic of observed plasma to gas phase transition as plasma decreases in volume, the skin of the optically dense plasma gives rise to the steady-state in observed spectra

3. 5 References

1. Xu, N.; Majidi, V., *Applied spectroscopy* **1993,** *47*, 1134-1139.
2. Ma, Q.; Motto-Ros, V.; Laye, F.; Yu, J.; Lei, W.; Bai, X.; Zheng, L.; Zeng, H., *Journal of Applied Physics* **2012,** *111*, 053301.
3. Ahmad, S. R.; Russell, D. A., *Propellants, Explosives, Pyrotechnics* **2005,** *30*, 131-139.
4. De Giacomo, A.; Dell'Aglio, M.; Gaudiuso, R.; Amoruso, S.; De Pascale, O., *Spectrochimica Acta Part B: Atomic Spectroscopy* **2012,** *78*, 1-19.
5. Farooq, W. A.; Tawfik, W.; Alahmed, Z. A.; Ahmad, K.; Singh, J. P., *Journal of Russian Laser Research* **2014,** *35*, 252-262.
6. Vadillo, J. M.; Fernandez Romero, J. M.; Rodriguez, C.; Laserna, J. J., *Surface and interface analysis* **1999,** *27*, 1009-1015.
7. Boker, D.; Bruggemann, D., *Spectrochimica Acta Part B-Atomic Spectroscopy* **2011,** *66*, 28-38.
8. Ionin, A. A.; Kudryashov, S. I.; Makarov, S. V.; Saltuganov, P. N.; Seleznev, L. V.; Sinitsyn, D. V.; Lednev, V. A.; Pershin, S. M., *JETP Letters* **2015,** *101*, 308-312.
9. Luna, H.; Dardis, J.; Doria, D.; Costello, J. T., *Brazilian Journal of Physics* **2007,** *37*, 1301-1305.
10. López-Claros, M.; Vadillo, J. M.; Laserna, J. J., *Journal of Analytical Atomic Spectrometry* **2015**.
11. De Giacomo, A.; Dell'Aglio, M.; De Pascale, O.; Gaudiuso, R.; Palleschi, V.; Parigger, C.; Woods, A., *Spectrochimica Acta Part B: Atomic Spectroscopy* **2014,** *100*, 180-188.
12. Nagy, B.; Nemes, L.; Kubinyi, M., *Periodica Polytechnica-Chemical Engineering* **2009,** *53*, 61-66.

13. Yermachenko, V. M.; Kuznetsov, A. P.; Petrovskiy, V. N.; Prokopova, N. M.; Strel'tsov, A. P.; Uspenskiy, S. A., *Laser physics* **2011,** *21*, 1530-1537.

14. Shcheglov, P. Y.; Gumenyuk, A. V.; Gornushkin, I. B.; Rethmeier, M.; Petrovskiy, V. N., *Laser Physics* **2013,** *23*, 016001.

15. de la Cruz, J.; Roberto Pineda, II, *International ophthalmology clinics* **2007,** *47*, 73-84.

16. Netto, M. V.; Mohan, R. R.; Ambrósio Jr, R.; Hutcheon, A. E. K.; Zieske, J. D.; Wilson, S. E., *Cornea* **2005,** *24*, 509-522.

17. Lopez-Moreno, C.; Palanco, S.; Laserna, J. J.; DeLucia Jr, F.; Miziolek, A. W.; Rose, J.; Walters, R. A.; Whitehouse, A. I., *Journal of Analytical Atomic Spectrometry* **2006,** *21*, 55-60.

18. Bremer, M. T.; Wrzesinski, P. J.; Butcher, N.; Lozovoy, V. V.; Dantus, M., *Applied Physics Letters* **2011,** *99*, 101109.

19. Kappen, K.; Beyer, R., *Propellants, Explosives, Pyrotechnics* **2003,** *28*, 32-36.

20. Valliere, R. Plasma Propellant Interactions: RDX Films in Hydrogen, Argon, and Mixed Composition Plasmas. Auburn University, 2013.

21. Pesce-Rodriguez, R. A.; Beyer, R. A., *Army Research Lab. Tech. Rep. t ARL-TR* **2004,** *3286*.

22. Blumenthal, R. *Understanding the Plasma-Propellant Interaction through Experimental Modeling*; DTIC Document: 2009.

23. Gregorčič, P.; Možina, J., *Optics letters* **2011,** *36*, 2782-2784.

24. Boueri, M.; Baudelet, M.; Yu, J.; Mao, X. L.; Mao, S. S.; Russo, R., *Applied Surface Science* **2009,** *255*, 9566-9571.

25. Taylor, M. J., *Propellants, Explosives, Pyrotechnics* **2003,** *28*, 26-31.

26. Beule, D.; Ebeling, W.; Förster, A.; Juranek, H.; Nagel, S.; Redmer, R.; Röpke, G., *Physical Review B* **1999,** *59*, 14177.

27. Bonitz, M.; Levashov, P. R.; Mulenko, I. A.; Oleinikova, E. N.; Filinov, V. S.; Fortov, V. E.; Khomkin, A. L., *Plasma Physics Reports* **2002,** *28*, 484-488.

28. Kappus, B.; Khalid, S.; Chakravarty, A.; Putterman, S., *Physical review letters* **2011,** *106*, 234302.

29. Delgado, T.; Vadillo, J. M.; Laserna, J. J., *Journal of Analytical Atomic Spectrometry* **2014,** *29*, 1675-1685.

30. Zhigilei, L. V., *Applied Physics A* **2003,** *76*, 339-350.

31. Saito, K.; Takatani, K.; Sakka, T.; Ogata, Y. H., *Applied Surface Science* **2002,** *197*, 56-60.

32. King, R. B., *The Astrophysical Journal* **1948,** *108*, 429.

33. Hagan, L. G., *The absolute intensity of C2 Swan bands*. Lawrence Radiation Laboratory: 1963.

34. NIST: Atomic Spectra Database Lines Form. In 2015.

35. De Giacomo, A.; Gaudiuso, R.; Dell'Aglio, M.; Santagata, A., *Spectrochimica Acta Part B: Atomic Spectroscopy* **2010,** *65*, 385-394.

36. D'Yachkov, L. G.; Golubev, O. A.; Kobzev, G. A.; Vargin, A. N., *Journal of Quantitative Spectroscopy and Radiative Transfer* **1978,** *20*, 175-189.

37. Morris, M.; Spectrecology, Owner. In Casper IV, W. F., Ed. 2015.

38. Tang, C.-J.; Lee, Y.; Litzinger, T. A., *Combustion and flame* **1999,** *117*, 244-256.

39. Zou, J. L.; Xiao, R. S.; Huang, T.; Li, F.; Ma, R., *Laser Physics* **2014,** *24*, 6.

40. Kop'ev, V. A.; Kossyi, I. A.; Magunov, A. N.; Tarasova, N. M., *Instruments and Experimental Techniques* **2006,** *49*, 573-576.

41. Harilal, S. S.; Bindhu, C. V.; Issac, R. C.; Nampoori, V. P. N.; Vallabhan, C. P. G., *Journal of Applied Physics* **1997,** *82*, 2140-2146.

42. Borges, F. O.; Cavalcanti, G. H.; Gomes, G. C.; Palleschi, V.; Mello, A., *Applied Physics B* **2014,** *117*, 437-444.

43. Sakka, T.; Iwanaga, S.; Ogata, Y. H.; Matsunawa, A.; Takemoto, T., *Journal of Chemical Physics* **2000,** *112*, 8645-8653.

44. Sakka, T.; Takatani, K.; Ogata, Y. H.; Mabuchi, M., *Journal of Physics D: Applied Physics* **2002,** *35*, 65.

45. Norman, G. E., *Contributions to Plasma Physics* **2001,** *41*, 127-130.

46. Iosilevski, I. L.; Chigvintsev, A. Y., Phase Transition in Simplest Plasma Models. In *Physics of Nonideal Plasmas*, Springer: 1992; pp 87-94.

Chapter 4

Observation of four distinct mechanisms of material removal from a molecular solid as the distance between the sample and the point of maximum UV laser focus is adjusted

4.1 Introduction

4.1.1 Lasers as a scientific tool

Lasers have been used as tools in science, manufacturing and medicine for over fifty years.[1, 2] With sufficient energy, lasers have the ability to remove materials through a process known as ablation, where part of the sample is removed with little or no damage to surrounding material. When reshaping a cornea during eye surgery, the laser interaction is more selective and controlled than a scalpel, resulting in less residual damage and more rapid healing due to the ability to precisely focus a laser pulse.[3] In manufacturing, lasers are able to remove or join micrometers of metals that traditional methods of cutting and welding cannot. Recent advances in 3D printing have allowed the fabrication of parts from computer designs by using a laser as a tool to harden polymers. With laser ablation being at the heart of such a diverse set of tools, understanding of the fundamentals of the processes is of critical importance to the optimization and refinement of these processes.

Early mechanistic studies began with attempts to characterize laser induced sparks,[4] which is the ionization of air to a plasma through laser irradiance. The initial understanding of laser-solid interactions was as a form of very rapid local heating or UV absorption processes.[5, 6] Schlieren photography[7] and shadowgraph imaging revealed the evolution of shockwaves and other gas dynamical features present in laser induced plasmas (LIPs). Interferometer

measurements were used to determine the electron densities and local temperatures.[8] More recently, these spectroscopic diagnostic techniques have evolved into laser induced breakdown spectroscopy (LIBS), an analytical techniques capable of identifying the temporal evolution of the chemical species in a plasma.[9, 10] Optical spectroscopy and fast-imaging techniques[11-13] have been used to understand the temporal[14] and spatial[15] evolution of laser induced plasmas.[16] As the mechanisms of plasma formation and ablation have further been studied, other factors of the process achieved greater interest.[17] This includes plasma plume formation,[18] expansion,[19] and decay during laser ablation.[20] Each of these plasma features are dependent upon background gas,[21-23] and especially laser power and wavelength.[24-27] One of the most important aspects relevant to the understanding of LIP and ablation mechanisms[28] is the dependence on the exposed material. The different molecular structures result in unique plasma emission signatures as different atomic and ionic species are present with different energy, and thus various emission spectra.

4.1.2 Laser interaction with materials

From a fundamental standpoint, the interaction of a photon with a solid depends on the electronic structure of the material and the wavelength of the light incident upon it. Infrared (IR) photons are adsorbed directly into the vibrational modes of the material. The increased vibrational motion leads directly to an increase in temperature that induces a very rapid melting, vaporization, and eventually ionization. Hence, the infrared interaction is a photo-thermal process occurring in a very short time (ns or fs). Further, IR absorption then depends on the thermal properties of the material. If the wavelength of light is resonant with the material and fluence is high, very fast heating is achieved. Most materials have a relatively continuous IR spectrum. Ablation occurs as the very rapid heating eventually leads to vaporization. Continued

IR irradiation can then heat the vapor to ionization resulting in plasma formation. The IR absorption is a linear process occurring with a first order rate.

In contrast, in the UV ablation process, the photons have more energy and are absorbed by electronic transitions. If the material and laser wavelength are resonant, the interaction can take place similar to an IR absorption process. In a metal there is a continuum of real states. In insulating and semi-conducting materials, the incident photons excite electrons into a virtual state. If a second photon is present before the electron decays back to the ground state, the electron may be promoted to the continuum. Removing an electron from the ground state will result in a disruption to the bonding in the molecule. When this ionization happens to two electrons, bond breaking occurs. If the bond breaking process occurs simultaneously at multiple sites, ablation occurs. Under UV irradiation of insulators or semiconductors, the excitation of the solid to a plasma is a multiphoton photoionization process and frequently not linear. Thus the laser induced plasma formation is capable of conversion of a solid directly to a plasma state, but only in the regions where laser fluence is intense enough to drive the multiphoton process, without disrupting neighboring material. Observations of the features formed by laser ablation can give insight into the mechanism of the event.

4.2 Experimental

4.2.1 Sample preparation

Thermal laser paper (ZAP-IT®) was used as received from Kentek. All solid polymer films were purchased from McMaster Carr in 25.4 μm thickness and used as obtained except for the removal of protective coatings that were peeled off of the polycarbonate before use. Samples of RDX were prepared through a nebulizing spray technique described elsewhere.[29] Briefly, using a syringe pump (New Era NE-1000), a 10 mL 5mg/mL solution of RDX in acetonitrile was pumped through a 32GA SS-304-RW capillary at a rate of 1 mL/h. Using nitrogen at 20 psi (138 kPa) as a carrier gas, the resulting spray was deposited on a 2" borosilicate glass wafer 41.28 mm from the end of the capillary. During spray process, the wafer was spun at a constant rate of 220 rpm below the incident spray. The sprayer was moved across the wafers surface from the center to the outer edge in increasingly longer time steps to yield a uniform coating. A 50 mJ, 6.5 ns, 266 nm Nd:YAG laser pulse (Continuum Inlite III-10) was used in all experiments. The laser pulse is redirected by 90° by a mirror (Melles Griot Y4-2037-0) and down to the sample. A 120 mm focal length lens (Edmund Optics), placed on a separate automated x-axis translator for precise positioning, was used to focus the laser light onto the sample surface at various lens to sample distances (LSD). Experiments were carried out at LSD of 60-150 mm in 10 mm increments.

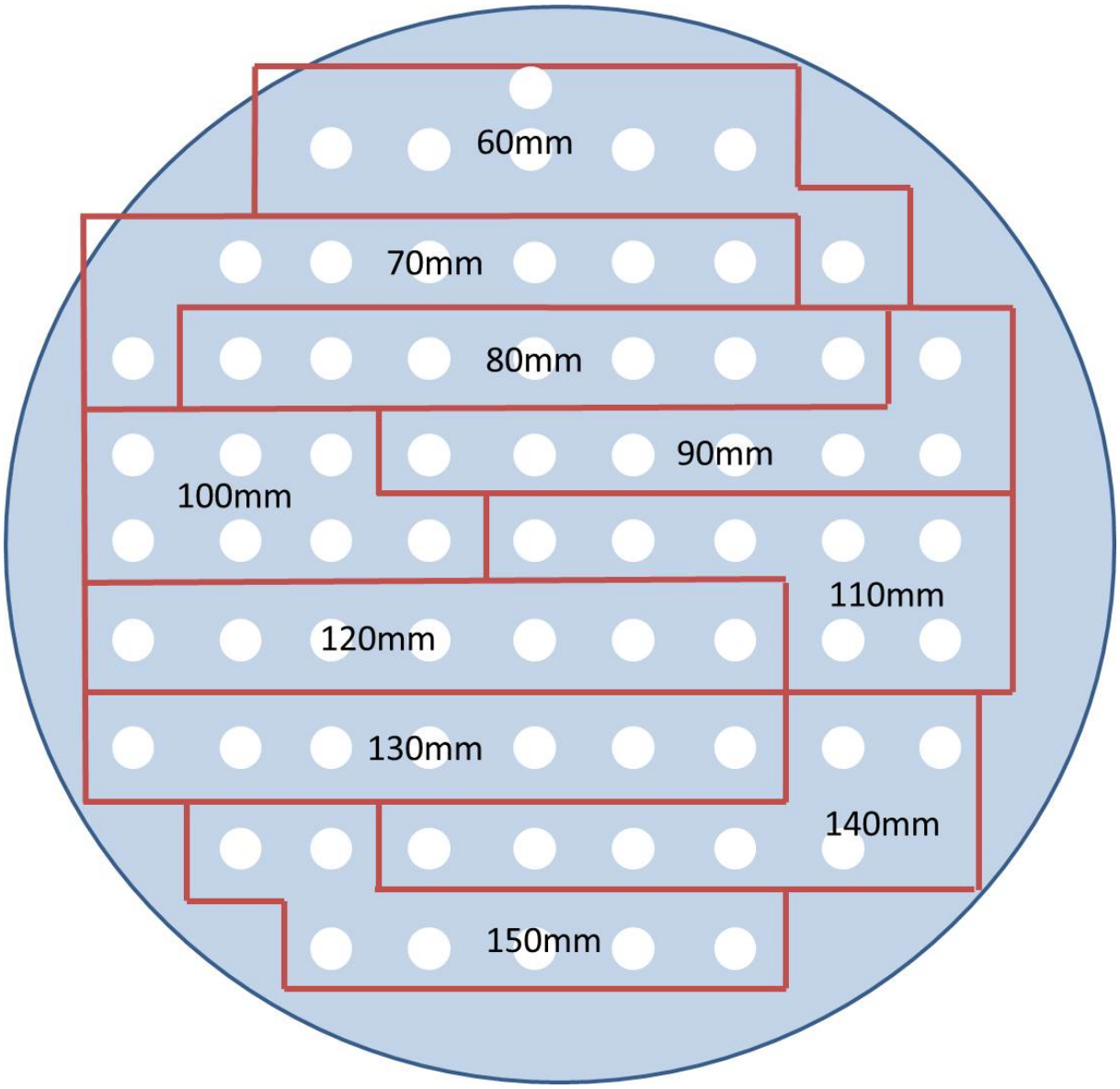

Figure 4.1. Layout of wafer shots at each LSD

4.2.2 Sample translation

To ensure that each laser shot was incident on fresh material, the sample was translated between laser pulses with an automated two-dimensional positioning system perpendicular to the direction of the beam and axis containing the lens. The locations of the laser shots for each LSD were uniformly distributed on the wafer as shown in Figure 4.1. The 5mm spacing was independently determined as to not have the current ablation event overlap with the next in any

direction.[30] This spacing on the wafer was such that 70 shots could be fired on each prepared sample allowing a repeatability of seven shots per LSD.

4.2.3 Spectroscopy

Spectroscopic observations of the resulting plume were collected by an optical emission spectrometer shown in Figure 4.2 and described previously in detail in Chapter 2. The emission is collected by the 10.0 mm ball lens (Edmund Optics 32-748) attached to a fiber (Thor Fiber M71L01) which is directed onto the entrance slit of the diffraction grating. The wavelength dispersed light emitted from the grating is incident upon the gated cathode of the image intensifier (Varo 510-9323-301) detector, gated by custom built fast-switching driving electronics. The amplified output of the image intensifier is captured by a CCD camera focused on it. As a result, the plasma plume radiation (emission) is efficiently collected and spatially distributed onto the camera's CCD array for 20 μs following the laser pulse.

4.2.4 Experimental timing

Precise timing of laser pulse to gated collection was accomplished using four function generators and is depicted in Figure 4.3. The origination pulse generated by the custom computer automation program that was user initiated began after a 10 s delay. After the delay, the flash lamps were triggered through the laser power supply, with an internally defined 175 μs q-switch delay. The q-switch sync pulse was then used to trigger a delay which could be adjusted to move the spectroscopic detector signal anywhere in time with respect to the laser pulse. The CCD camera began exposure before the laser pulse was fired. The image intensified gated detector was operated at a minimum 1μs delay from the pulse as to not contaminate the spectra with laser light. Temporal resolution is achieved by integrating the 20 μs exposure period of image intensified operation over the duration of the CCD collection time.

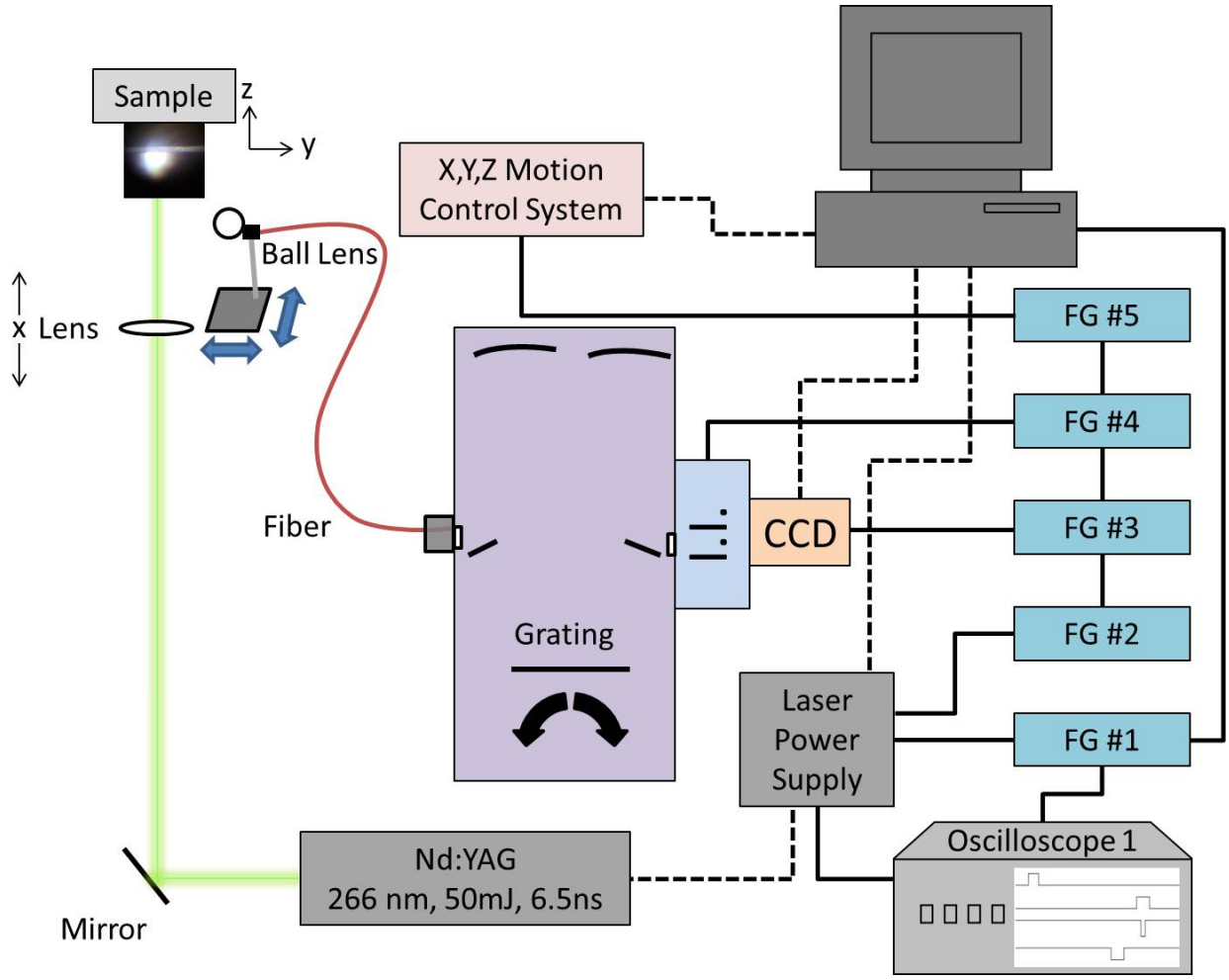

Figure 4.2. Experimental set up showing trigger connections (solid lines) and computer connections (dash lines)

All aspects of the experiment were controlled through custom software. Beyond the initial trigger to fire the laser and trigger the spectrometer, the computer saved the resulting image as a *.bmp and controlled the motion of the sample. After seven experiments at each LSD, the programmed routine moved the lens 10 mm from the previous location to the new LSD and repeated until all 70 data points from 60 mm to 150 mm were collected. The spectra presented then reflect seven averaged experiments at each LSD.

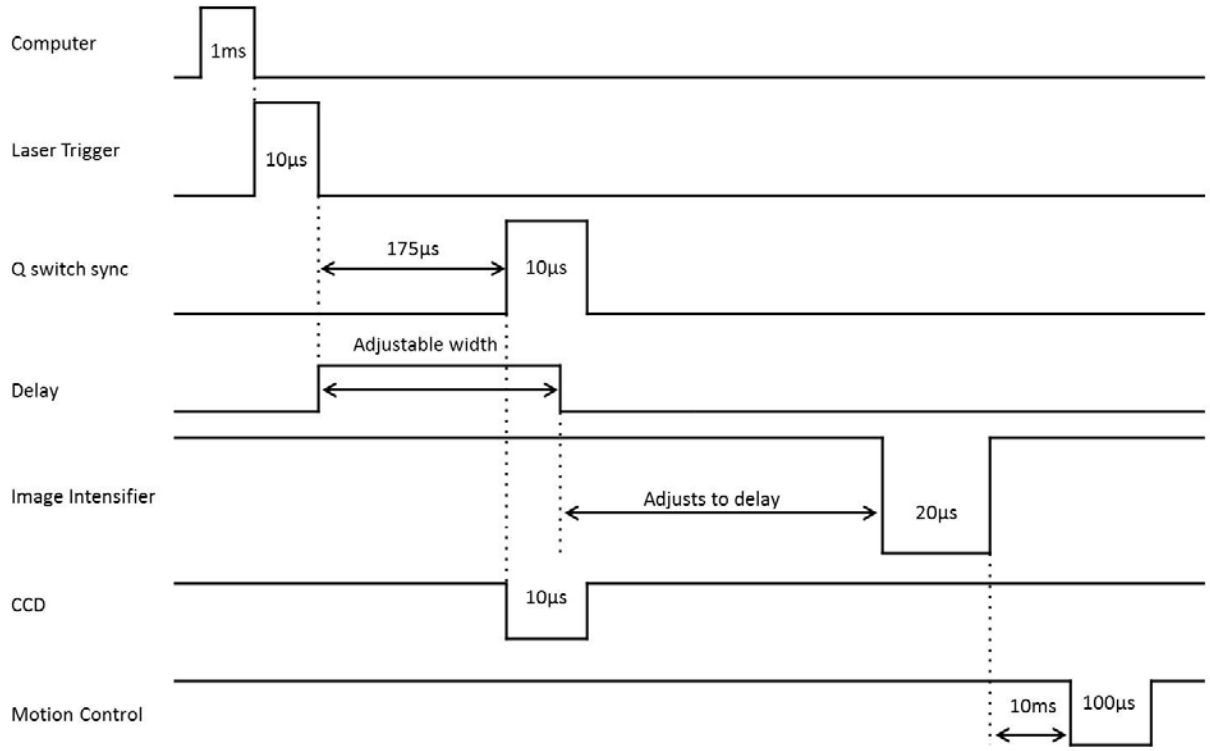

Figure 4.3. Schematic diagram of experimental timing

The laser was fired at a 10 Hz repetitious rate while videos (Pentax Optio S5i) were taken at a 30 Hz rate to record the long term formation, evolution, and decay of the LIP. Single frame images of the video were obtained to glean specific information about the LIP and ablation thresholds. From the ablated samples, photographic evidence of material removed was obtained by imaging the resulting materials after ablation with the camera at a fixed height from the samples. The laser paper was photographed as is, PC on a white background, and PE and RDX on black backgrounds to create the highest degree of contrast. All images of irradiated samples were taken under identical imaging conditions.

4.3 Results

4.3.1 Ablated film images and still frame evidence from videos

Images of the resulting ablated films are presented in Figure 4.4 for laser paper, polyethylene, polycarbonate, and RDX from top to bottom. One general trend seen in all images is that the pits grow smaller as the sample becomes closer to the focal point of the lens. The trend for laser paper, PC, and PE are all similar in that the ablation pit generally grows smaller and there is only one distinct feature present. Unlike the others, RDX displays four distinct types of pits and does not follow the same general trend of the other three samples indicating that there are other mechanisms of removal dominating the formation of pits.

The areas of each pit feature were measured using ImageJ[31] by fitting an ellipse to the pits. As a proxy for the radius, the square root of the area is plotted in Figure 4.5. There is no consistency across samples in terms of a largest overall pit at each sample position. The laser paper uniformly decreases in spot size as the sample is moved to the focal point of the lens and then increases after. The detailed structure of the pit remains the same as the overall size decreases and increases following the “v-shape” on Figure 4.5. As also seen on the laser paper, as could be expected for a typical focusing of light with a lens, the polycarbonate ablation pits linearly decreases as the sample location is increased to the focal length of the lens and then linearly increases as the point of maximum focus is further moved away from the sample. Polyethylene at the two extreme distances measured does not have any visible pits, and a uniform removal of material is only seen at the three positions near the focal point of the lens. The curve on Figure 4.5 is similar to that of the laser paper. The RDX ablation pits have four different general appearances, a thinned sublimed region not complete, a near completely removed pit with a “drip”, a completely ablated region with a thinned ridge surrounding the pit,

and a completely removed pit with chunks of ablated material on still present. All of the RDX pit sizes vary with distance and do not have a trend as with other samples.

The still frame images extracted from the video recording of the PE ablation are shown in Figure 4.6. Snapshots were taken at various focus conditions to demonstrate the influence of focus upon the resulting plume. The ball lens is seen on the right of the image, and the sample and plume on the left. The lowest degree of luminosity above the plane of the sample is at the distances where the focal point is behind the sample surface. When the focal point is brought to the sample plane, a plume is observed that extends from the surface. At distances greater than the point where the focus is in the sample plane, the ionization of air can be observed. Each of these dynamic features of the plumes may contribute to the appearance of the resulting ablation pits. The air plasma may be observed in Figure 4.6 as the bright dot located in front of the sample surface at 110 mm to 150 mm.

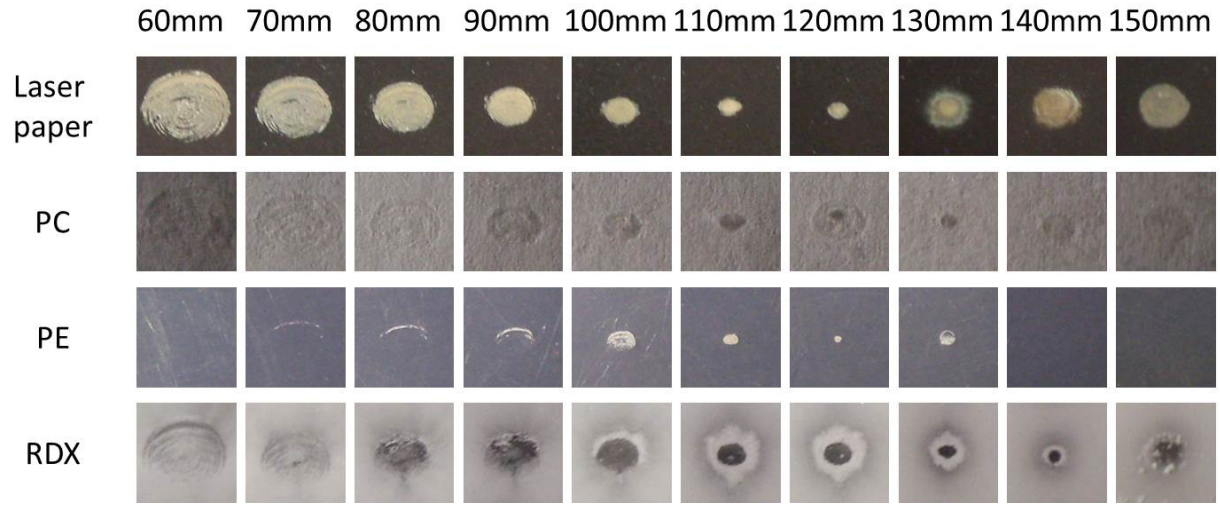

Figure 4.4. Images of samples after laser irradiation at different lens to sample distances (5mm by 5mm)

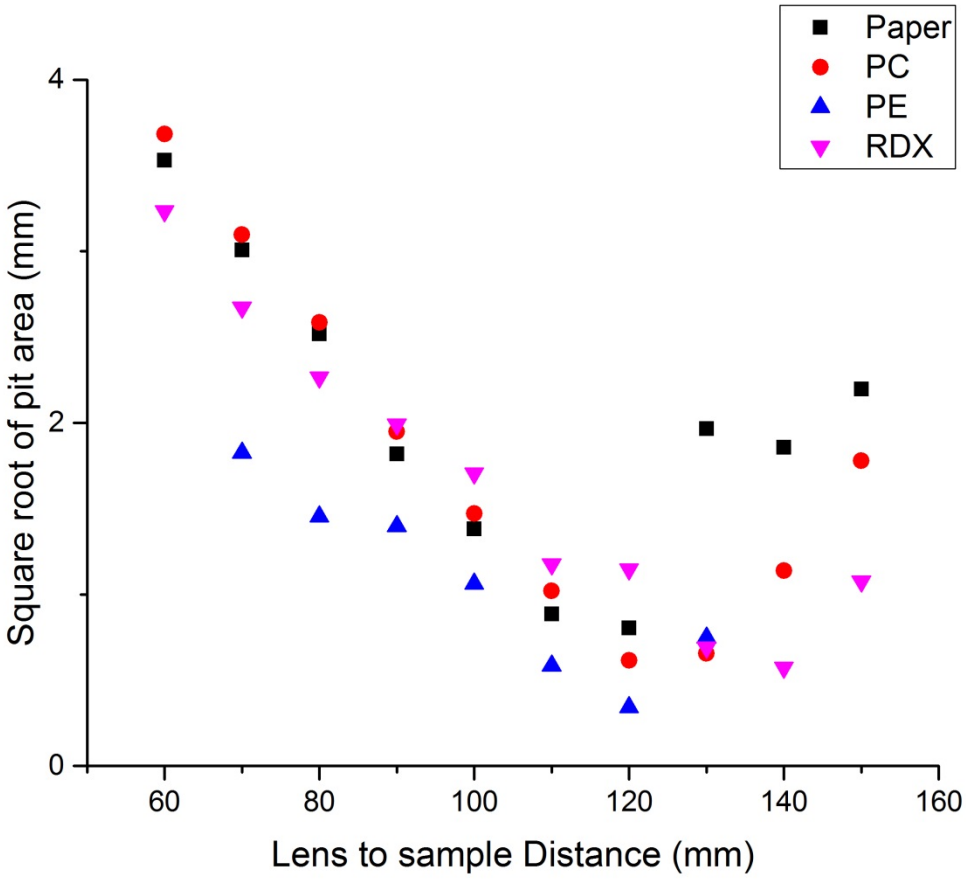

Figure 4.5. Resulting ablation area of laser spot size at each lens to sample distance

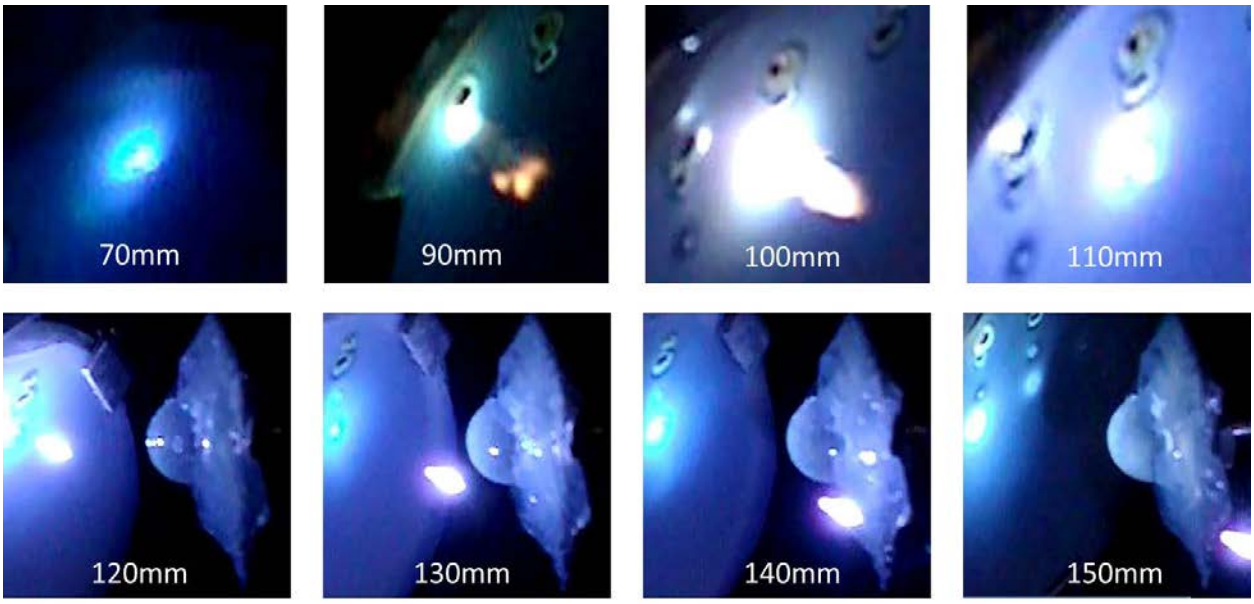

Figure 4.6. Evolution of plasma formation on PE at different lens to sample distances. Still frame image taken from video approximately the 15th laser pulse

4.4 Discussion

4.4.1 Images of laser paper

The laser paper was studied as a potential blank for comparison to the other samples. It was found that resulting images would primarily illustrate the laser spot resulting from a thermal process. As the LSD is changed from 60 to 120 mm, the pits formed on the films decrease in size nearing the focal point of the lens. After the lens is moved past its focal point, the resulting image of the pit sizes show an increase, with a secondary ring structure surrounding the laser spot (between 130-140 mm).

When the LSD is increased to the greatest distances, the focal point is no longer on or behind the sample but focused at a point in front of the sample in the air. At the laser fluence used, a local ionization forming a plasma of air is observed at the point of maximum focus. This plasma consumes some portion of the laser energy, reflects another portion, while allowing the remaining portion to pass through to the plane of the sample. The amounts however are unknown as the atmospheric plasma, at maximum focus, acts like a metal and is reflective as well. The additional ring observed on the paper in Figure 4.4 at 130-140 mm may be due to radiation from this plasma. The radius of the laser beam when moved toward the focal point of the lens should scale as a function of the radius. As is seen in Figure 4.5 however, there is non-linearity to the resulting spot size indicating the multi-photon ionization process, which results from including the effects of the air plasma.

4.4.2 Polycarbonate results

On polycarbonate, the ablation pits follow a similar trend as were observed on the laser paper. The closest LSD pits also begin to show a rippled ring structure that may reflect the oscillation of the laser pulse intensity. As the beam profile is not uniform over all areas, there are

regions of higher and lower fluence. At close LSD, there are regions of high enough fluence to ionize portions of material, and these regions show where shallow ablation has occurred. As the LSD is increased to 100 mm, the fluence becomes great enough to not only selectively ablate the film as is shown in earlier images, but there is a clearly defined ablation pit present, representative of the beam diameter. At this point, the distribution of energy to the surface area is high enough in all regions so that a complete local removal of material is possible. As the pits become deeper, they presumably become more pronounced. At 120 mm, the ablation pit is smallest, with an outer diameter pit also showing signs of being affected. At this point two things have taken place as can be seen in Figure 4.6 together with the formation of the air plasma. One, the center most portion of the pit is exposed to a fluence significantly above the ablation threshold, resulting in a direct ablation and plasma formation. This region is presumably completely ionized to a high degree. Therefore, the plasma formation at this region is heated to high temperatures resulting in radiation back to the sample surface that is capable of transforming the film surrounding the pit to a melt region similar to those seen in the previous images.

From the plot in Figure 4.5, it can be seen that the PC spot size is actually larger than the paper up until the point of maximum focus. Using the laser paper as a standard measure of laser spot size was the original intent. However, the UV photons have enough energy to disrupt any of the bonds in the laser paper. Therefore, it is likely that the formation of plumes above the laser paper surface could contribute to the spot size on the thermally reactive laser paper. The non-linearity of the laser spot size with respect to lens to sample distance shows that ablation occurs via a multi-photon absorption process. A single photon, first order process would yield a linear dependence. The larger spot size in PC compared to the laser paper suggests then that the

threshold to UV ablation is actually lower in the former case. The change in correlation of spot size to distance, with PC to laser paper, is further evidence that laser – induced air ionization was taking place. Positioning the lens at a distance greater than the focal length focuses the beam energy at a point above the sample. This creates a plasma above the sample surface. In polycarbonate this phenomena does not affect the sample as much as the case of the laser paper. Since the laser paper is thermally sensitive, the air plasma taking place within vicinity of the paper will be radiating heat. This radiation is what induces an increased area of the spot size on the laser paper but not PC at these greater LSD.

4.4.3 Polyethylene results

In the single shot experiments of PE, there is no visible material removed from the sample surface until a distance of 70 mm is reached (Figure 4.4). It is not until 100 mm that a fluence capable of removing a detectable amount of material is observed. The previous pits have only an upper ring that is visible suggesting that that is a region of the beam energy where the fluence is large enough to create visible ablation. This could be indicative of the laser pulse having a high energy density across the upper portion of the focused pulse and not elsewhere. This results in material loss in this region with the same general pattern as seen in paper at 60mm. The spot size in PE is the smallest in all of the cases indicating that the threshold for plasma formation and material removal is greatest here. The thermal threshold due to radiation of neighboring plasma plumes is also higher than for other materials as no signs of ablated regions are noticed. No visible evidence of damage at 60, 140 and 150 mm is observed. In the PE spectra of Figure 4.7, it can be seen that at the same LSD there is also a strong amount of carbon and other unidentified ionic and atomic species present in comparison to the blackbody – like continuum seen otherwise. Also to note, there is visible emission present at all LSD in the

resulting spectra for PE. This confirms that even though visible ablation was not noticeable on the resulting films in Figure 4.4, in fact, some material was removed.

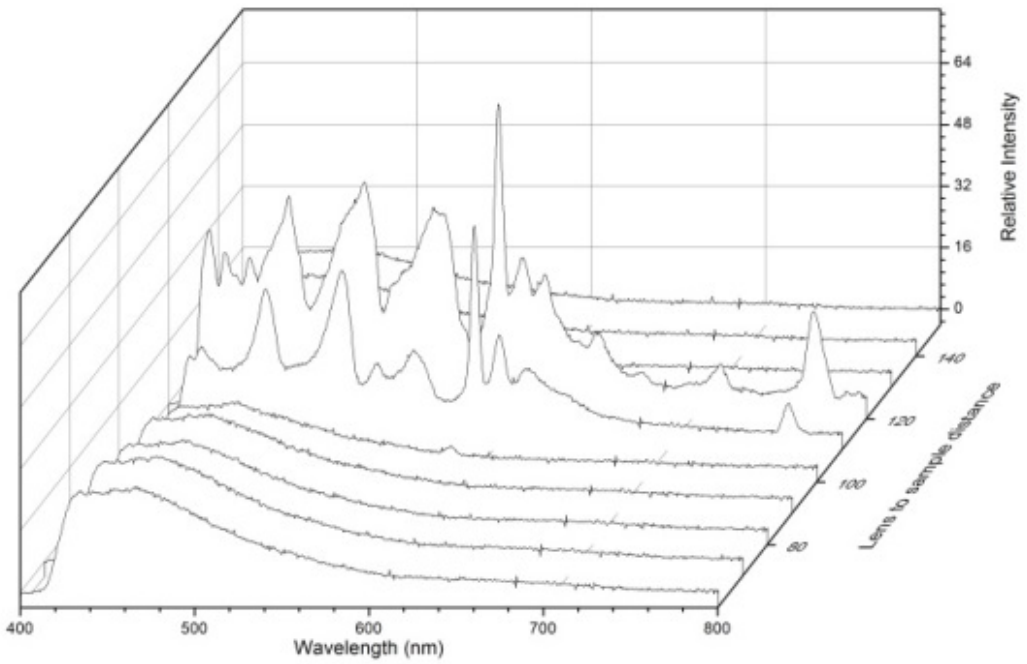

Figure 4.7. Spectroscopic results obtained with a polyethylene sample with C_2 swan bands present at 437, 470, 510, 554, and 610 nm as well as other unidentified ionic species.

From the images in Figure 4.6, evidence of the small degree of plasma formation is noticed at 70 mm. By 90 mm there is a large degree of formation and what appears to be a strong column of heated gas. At 100 mm the plasma formation is strong and extends far from the surface, whereas at 110 mm, it is mostly localized on the surface. By 120 mm the images suggest that there is still incident laser light on the surface, but also a plasma that has formed above. This could again be explained by formation of an air plasma forming above the sample surface, or evidence of plume splitting.[2, 32] The images from 130 to 150 mm, however, support the assumption that the increased area observed on the laser paper and not with PC is a result of this hot plasma radiating heat. There is no extra visible material that this plasma has removed. In

comparison, polycarbonate has a more efficient emission mechanism as the ablation is apparent to a greater degree at all LSD. This could be due to occupied states lying near the virtual states in PC, resulting in a near resonance enhancement.

4.4.4 RDX results

Combining all of the previous observations from the polymeric samples and the still frames of the plasma plume formation, the more complex material removal in RDX can be explained. In Figure 4.4 there is not a single simple trend across the images in RDX. From 60 to 120 mm, the pit sizes resemble the pits on the laser paper. At 60 and 70 mm, there is only a clean ablation process as evidenced from the sharp edges, but broadened because melting was taking place, and the pits are nearly identical in size and shape to those of the laser paper. Only in regions of the beam in which the fluence is great enough for the second order process to proceed does removal take place. The material surrounding the pit is left untouched indicating that no thermal interaction was taking place as would be expected in a first order ablation process. A ringed structure (similar to that pattern in the laser paper) is observed, pointing to only regions of the beam that have high enough energy density for RDX removal.

In experiments with LSD values of 80 and 90 mm, an increase in the amount of RDX removed in comparison to 60 and 70 mm is noticeable. The white films were photographed on a black background, which becomes more visible through the ablated film. In comparison to the laser paper (Figures 4.4 and 4.5) the pits have a smaller area. Therefore the 80-90 mm region is driven by a secondary removal process, but with increased plasma heating. This conclusion is supported by 3D laser scanning microscope imaging,[33] where the results are presented in Figure 4.8 for 90 mm. The laser scanning images show pits rimmed with thicker, lighter, yellow/red regions leading up to darker, blue/black, thinner regions. The increase in removal of material

without a noticeable sublimation indicates that the ablation occurred in a localized region, but what is more apparent is the “drip” on the bottom edge of the pit. These experiments were performed in a vertical orientation. So presumably, the hot removal of molecular RDX would “fall” downward from the surface of the film. It has been shown that the ablation process can eject hot material during the UV interaction, and that molecular solids can be removed.[2, 17, 37]

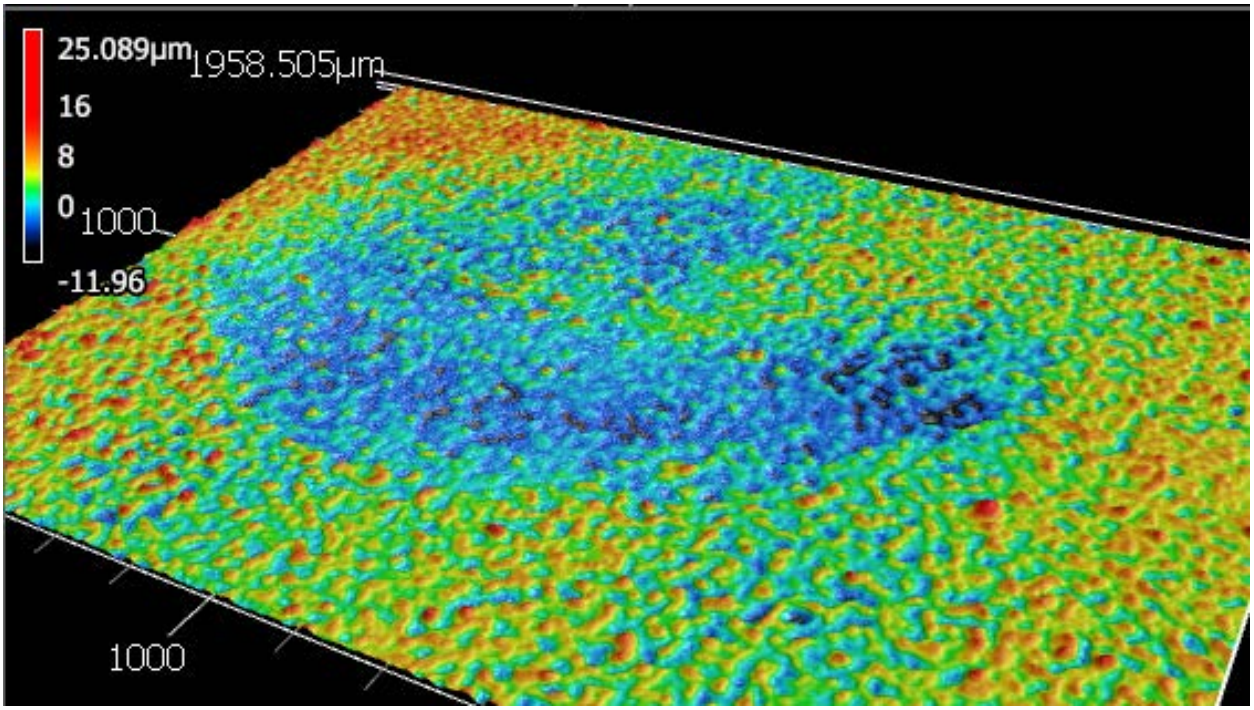

Figure 4.8. 3D laser scanning microscopic evidence of sloped edges of RDX ablation pit

In the range of 110 to 140 mm, there is a complete thin film removal over the entire spot size. The complete removal of material in this case may also be driven by a chemical interaction from the reactive species in the plasma plume. The pits here are larger due to sublimation and this being the region nearest to the focal point of the lens with highest fluence. This is indicative of the beam profile being focused to the point at which the uniform energy density of the laser is great enough to remove all material over the spot size of the beam. There is a hot plasma that has

completely ionized the material and/or part of the air in front of the sample. This hot body at the sample surface is capable of radiating heat back.

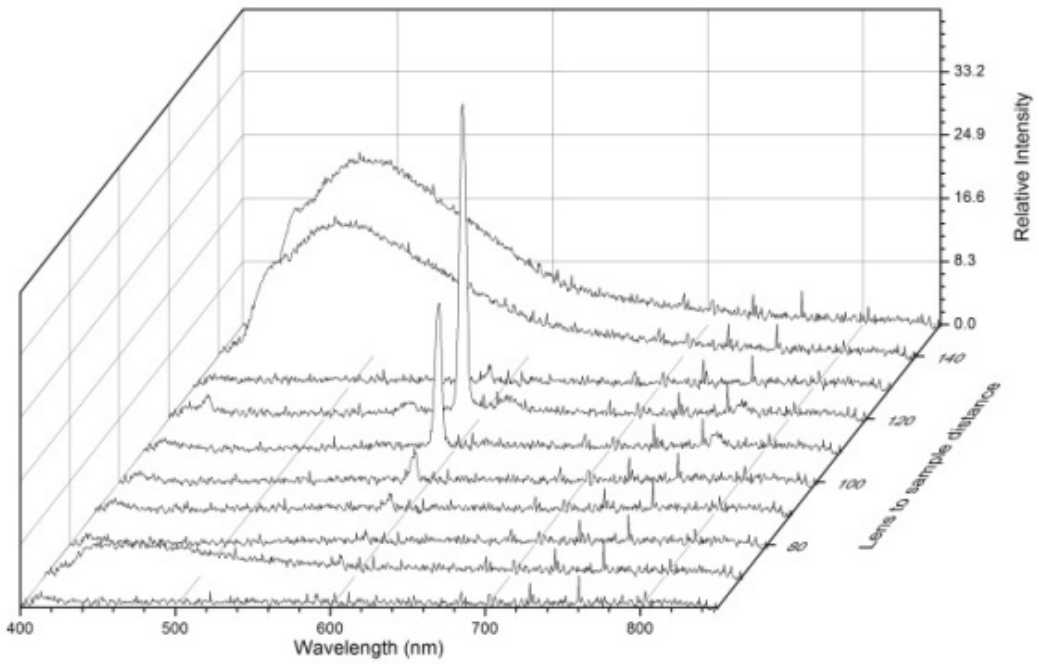

Figure 4.9. Spectroscopic results obtained from an RDX sample

Additional evidence suggesting different mechanisms at different LSDs can be inferred from the emission spectra shown in Figure 4.9. The atomic emission line at 588 nm is likely from the presence of sodium in the RDX sample. Other unidentified ionic and atomic species may be present at other wavelengths. In all of these LSDs, the pits and surrounding material are significantly larger than for laser paper, suggesting that there is another contributing mechanism. If the only mechanism that was taking place was UV ablation, they should be comparable in size with no other additional features present. At this point the intense fluence is removing all of the material present completely. To a larger degree, it is suggested that there is a large plasma plume formed at this stage which is in near contact with the RDX film on the sample surface. The

plume arises either from the ionization of RDX species or from ionization of air in front of the sample surface as shown in Figure 4.6. The reactive species reflected in the emission spectra then could also further react with the RDX film leading to an increased material removal.[34-36] The spectra support the increase in spot size of the RDX films at these distances. This points to the lower threshold of material removal in this sample, and also the fact that the reactive species present from the vaporization lead to spectral lines and are known to react with RDX.[34] This region of fluence on the RDX film is in argument of a different mechanistic removal all together in comparison to the 60 – 70 mm region where only a second order ablation process dominates. Here, the second order process is clearly coupled with a reactive interaction between the plasma plume, and an increase in sublimation due to the hot body as indicated by the large sloped edges and the strong continuum present in the spectra of Figure 4.8.

The last significantly different feature of material removal in RDX was noticed in experiments with an LSD value of 150 mm. Most noticeably, there are large chunks of material that have either re-deposited or were fractured pieces of the film that have not been entirely removed. Here there appears to be somewhat of a central region removed but without clearly defined edges. The multi-photon ablation process is still present as a central portion indicative of the laser spot size is seen, but no evidence for sublimation is observed. The spot size is also significantly smaller than that on the laser paper (Figures 4.4 and 4.5). There are no sloped edges due to a sublimation process, but it appears that some of the edges are actually protruding from the surface. At this point the laser induced plasma of air is approximately 30 mm from the surface. This leads to a portion of the RDX film being removed through the secondary removal mechanism which leaves a portion of the film in a hot state. Arising from all laser induced plasmas are also shock waves[12, 38] at the point at which the air plasma has formed. We assume

that the laser induced shock fronts arising from the air plasma, from approximately 30 mm in front of the film are also well defined.[2] Part of the beam has interacted and ionized a portion of the material, it is in a hot and “prepared” state for removal through a shock mechanism.

4.5 Conclusion

The images of the RDX thin films subject to UV irradiation at different laser fluences, show there are four different mechanisms of material removal that occur. At LSD values of 60 and 70 mm, the most prevalent mechanism is that of the second order ablation process with no evidence of sublimation or additional material removed. Experiments with LSDs of 80 and 90 mm show increasing evidence of the secondary process, but in addition with significant sublimation as evidenced by the sloped edges from the well-defined pits as the diameter is changing. From 100 to 140 mm there is significant removal through second order ablation, a large degree of sublimation, and the presence of reactive plasma species that contribute to the increased material removal through an initiation mechanism. At 150 mm, the second order photoionization presumably thins a center portion where the beam is incident, and shock waves induced from the air plasma are believed to fracture the film.

4.6 References

1. Brech, F.; Cross, L., *Appl. Spectrosc* **1962,** *16*, 59.
2. Gottfried, J. L., *Physical Chemistry Chemical Physics* **2014,** *16*, 21452-21466.
3. Fujimoto, J. G.; Lin, W. Z.; Ippen, E. P.; Puliafito, C. A.; Steinert, R. F., *Investigative Ophthalmology & Visual Science* **1985,** *26*, 1771-1777.
4. Ahmad, N.; Gale, B. C.; Key, M. H., *Proceedings of the Royal Society of London Series a-Mathematical and Physical Sciences* **1969,** *310*.
5. Shearer, J. W.; Barnes, W. S., *Physical Review Letters* **1970,** *24*, 92-&.
6. Kaw, P. K.; Dawson, J. M., *Physics of Fluids* **1969,** *12*, 2586-&.
7. Jellison, G.; Parsons, C. R., *Physics of Fluids* **1981,** *24*, 1787-1790.
8. Gerardo, J. B.; Verdeyen, J. T., *Proceedings of the Ieee* **1964,** *52*, 690-&.
9. Martin, F.; Mawassi, R.; Vidal, F.; Gallimberti, I.; Comtois, D.; Pepin, H.; Kieffer, J. C.; Mercure, H. P., *Applied spectroscopy* **2002,** *56*, 1444-1452.
10. Scott, R. H.; Strashei.A, *Spectrochimica Acta Part B-Atomic Spectroscopy* **1970,** *B 25*, 311.
11. Gregorčič, P.; Diaci, J.; Možina, J., *Applied Physics A* **2013,** *112*, 49-55.
12. Gregorčič, P.; Možina, J., *Optics letters* **2011,** *36*, 2782-2784.
13. Devia, D. M.; Rodriguez-Restrepo, L. V.; Restrepo-Parra, E., *Ingenieria y Ciencia* **2015,** *11*, 239-267.
14. Harilal, S. S.; Bindhu, C. V.; Issac, R. C.; Nampoori, V. P. N.; Vallabhan, C. P. G., *Journal of Applied Physics* **1997,** *82*, 2140-2146.
15. Baig, M. A.; Qamar, A.; Fareed, M. A.; Anwar-ul-Haq, M.; Ali, R., *Physics of Plasmas (1994-present)* **2012,** *19*, 063304.

16. Tognoni, E.; Palleschi, V.; Corsi, M.; Cristoforetti, G., *Spectrochimica Acta Part B: Atomic Spectroscopy* **2002,** *57*, 1115-1130.

17. Zhigilei, L. V., *Applied Physics A* **2003,** *76*, 339-350.

18. De Giacomo, A.; Dell'Aglio, M.; De Pascale, O.; Gaudiuso, R.; Palleschi, V.; Parigger, C.; Woods, A., *Spectrochimica Acta Part B: Atomic Spectroscopy* **2014,** *100*, 180-188.

19. Capitelli, M.; Casavola, A.; Colonna, G.; De Giacomo, A., *Spectrochimica Acta Part B: Atomic Spectroscopy* **2004,** *59*, 271-289.

20. Rezaei, F.; Tavassoli, S. H., *Physics of Plasmas (1994-present)* **2013,** *20*, 013301.

21. De Giacomo, A.; Dell'Aglio, M.; Gaudiuso, R.; Amoruso, S.; De Pascale, O., *Spectrochimica Acta Part B: Atomic Spectroscopy* **2012,** *78*, 1-19.

22. Hiyoshi, R. I.; Brill, T. B., *Propellants Explosives Pyrotechnics* **2002,** *27*, 23-30.

23. Park, H. S.; Nam, S. H.; Park, S. M., *Journal of applied physics* **2005,** *97*, 113103-113103.

24. Wang, Q.; Jander, P.; Fricke-Begemann, C.; Noll, R., *Spectrochimica Acta Part B: Atomic Spectroscopy* **2008,** *63*, 1011-1015.

25. Haas, Y.; Ben-Eliahu, Y.; Welner, S., *Propellants, explosives, pyrotechnics* **1996,** *21*, 258-265.

26. Ma, Q. L.; Motto-Ros, V.; Lei, W. Q.; Wang, X. C.; Boueri, M.; Laye, F.; Zeng, C. Q.; Sausy, M.; Wartelle, A.; Bai, X. S. In *Characteristics of laser-induced plasma as a spectroscopic light emission source*, 2012, p 243.

27. Ahmad, S. R.; Russell, D. A., *Propellants, Explosives, Pyrotechnics* **2005,** *30*, 131-139.

28. Russo, R. E., *Applied Spectroscopy* **1995,** *49*, 14A-28A.

29. Orland, A.; Blumenthal, R., *Journal of Propulsion and Power* **2005,** *21*, 571-573.

30. Casper IV, W.; denHartog, H.; Blumenthal, R., **A Novel Method For The Laser Induced Ignition Of RDX**. In *Proceedings of the 46st JANNAF Combustion Subcommittee Meeting*, CPIAC: Albuquerque, NM, 2014.

31. Rasband, W. S., ImageJ. In U. S. National Institutes of Health: Bethesda, Maryland, USA, 1997-2014; Vol. 1.48.

32. Chen, A.; Jiang, Y.; Liu, H.; Jin, M.; Ding, D., *Physics of Plasmas (1994-present)* **2012,** *19*, 073302.

33. Eltinge, E.; America, K. C. o., Micro Analysis Group. In Casper IV, W., Ed. Auburn, AL, 2015.

34. Valliere, R.; Blumenthal, R., *Journal of Applied Physics* **2006,** *100*, 084904.

35. Blumenthal, R. *Understanding the Plasma-Propellant Interaction through Experimental Modeling*; DTIC Document: 2009.

36. Valliere, R., **2013**.

37. Sun, H.; Blumenthal, R. In *Products Of The Ultraviolet Laser Ablation Of RDX*, *Proceedings of the 43rd JANNAF Combustion Subcommittee Meeting*, 2009; 2009; pp 2009-0105CS.

38. Klimo, O.; Psikal, J.; Tikhonchuk, V. T.; Weber, S., *Plasma Physics and Controlled Fusion* **2014,** *56*, 055010.

Chapter 5

Laser ablation of polycarbonate covered thin films of RDX

5.1 Introduction

5.1.1 Energetic materials ignition

RDX as an energetic material (EM) for military use has been used alone, and in combination with other high explosives (HEs) for over seventy years.[1] Formulations, mixtures of EM and non-EM materials, can help control the sensitivity of RDX (1,3,5-Trinitroperhydro-1,3,5-triazine) by adding various stabilizers and binders.[2] However, this can also alter their performance, as the additive reduces the rate of reaction in the propellant. Secondary explosives have higher rates of combustion and are more stable than primary explosives.[3] Consequently, secondary explosives require a more easily ignitable source to initiate them, this forces primary explosives to still then have a presence as a primer in the detonators for initiation. The primer, being the most sensitive part of the system, becomes a significant safety factor in design of weaponry.[4] Successful initiation is necessary,[5] but a balance must be struck between safety and performance.

Foregoing the use of the primer would be ideal from a safety perspective, but would be impractical due to the energy barrier that is needed to overcome during the initiation of RDX.[6, 7] Igniting the RDX is the main goal which is accomplished by putting enough pressure and heat into the system. One option to a primer could be to use an inert material that could be transformed into a source of ignition at will. This is done in electrothermal chemical ignition (ETC).[8, 9] In ETC, a polymer is capacitively ablated in close proximity to the HE.[10] The ETC process that is taking place is a capacitive discharge of the polymer to a plasma state. One

additional advantage of ETC as seen in Figure 5.1, over traditional primers, is that this method decreases the delay time for ignition and is much more reproducible.[11] The downside is the power supply and capacitor that are required to capacitively ablate the polymer.

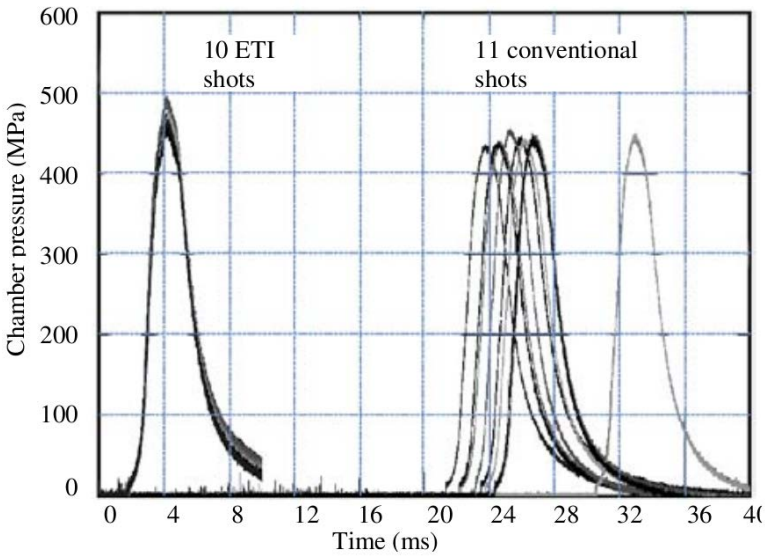

Figure 5.1. Comparison of an electrothermal ignition (ETI, ETC) process versus a traditional primer case[12]

The chemical species in the ETC plasma that were found to be significant have previously been identified using experimental modeling.[13] The species playing the largest role is the H• which implants itself in the RDX crystal, and induces a thermal HONO-like decomposition, resulting in production of six gaseous molecules for every one RDX molecule.[14] The source of these H• in ETC is the plasma resulting from capacitive ablation of a polymer such as polypropylene (PP) that is embedded in the charge itself. Another way to generate energetic plasmas from a polymer is through the process of laser ablation.[15, 16]

5.1.2 Laser ablation

In general, energetic materials cannot be easily ignited with most laser pulses.[17, 18] Therefore the need exists to pair the HE with an inert material that can be converted to a plasma and then in turn ignite the EM. The process of laser ablation has been known for some time and

has many industrial applications in machining, drilling, medicine, spectroscopy, and propulsion. Here, a laser beam interacts with a surface of a material when the high-energy pulse is focused onto it. The light is adsorbed, through an ionization process, resulting in formation of a plasma and finally heating. The resulting temperatures of the plasma can be on the order of $10^3 - 10^4$ K with electron densities $>10^{15}$ cm^{-3}.[19-22] At these temperatures, ionized and neutral atomic species should be all that is present and they would then be free to react with any other material. This process of laser ablation creates an environment similar to that found in an ETC igniter.[23, 24] Furthermore, the species present in the laser induced plasma were found to be similar to those that were deemed responsible for the mechanism of ETC ignition during experimental modeling.[25] Therefore, coupling the knowledge of ETC and laser induced plasmas to a weapons system could provide a safer and more effective weapons system.

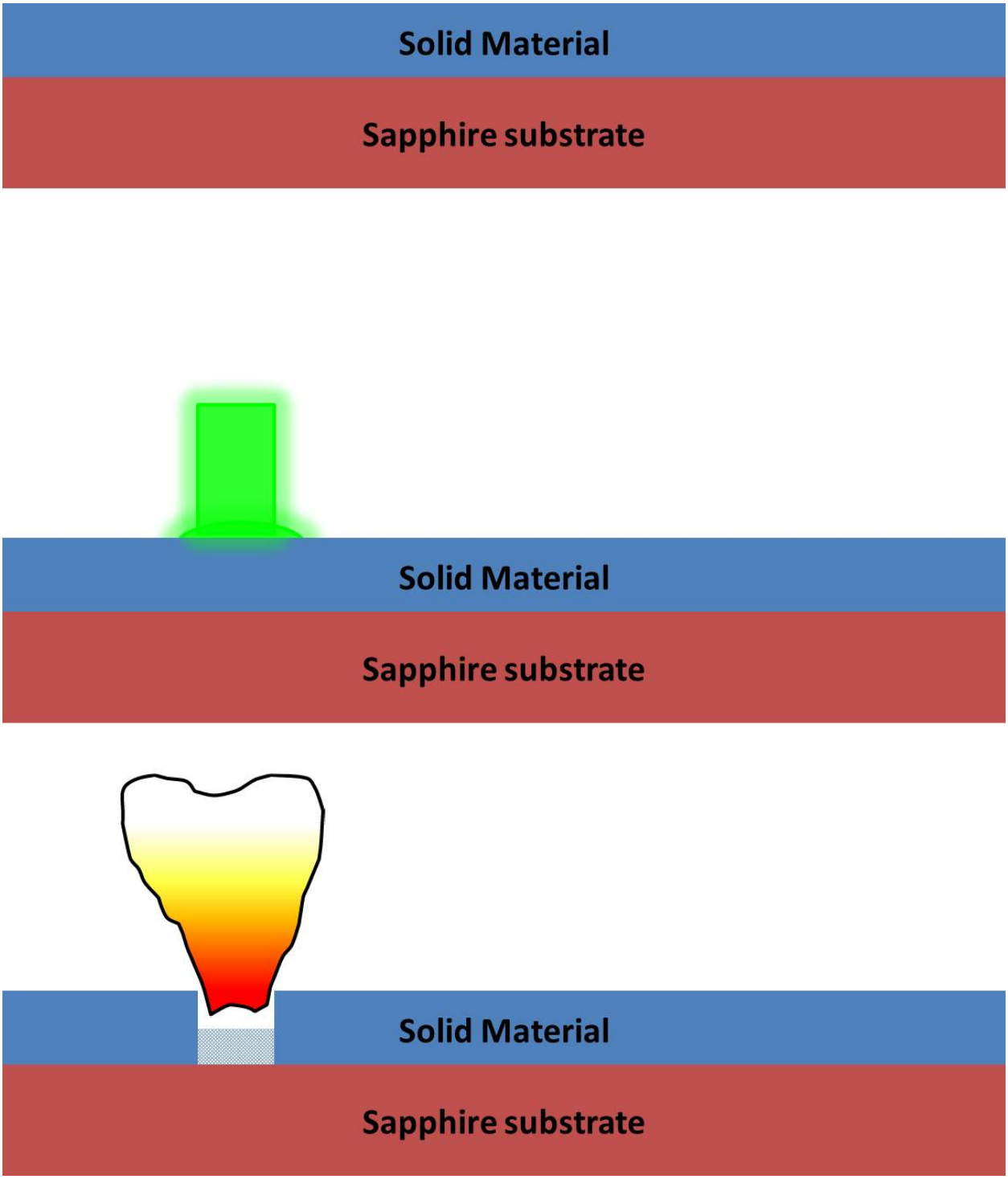

Figure 5.2. Model of laser ablation. From top to bottom, pristine sample substrate (sapphire wafer) with a deposited thin film of solid material, a laser pulse incident upon the material interacting through an adsorption process, and the resulting laser induced plasma and removal of material

The process of laser ablation depicted in Figure 5.2 involves many complex mechanisms[26-28] such as adsorption,[29] ionization,[30] heating,[26, 31] material removal,[32] plasma and shock wave formation[33, 34]. Each of these is dependent upon photon wavelength[35, 36] pulse duration, fluence,[37] as well as the optical properties of the materials.[38] The focus of the discussion herein will be concerned with the UV laser ablation from a 266 nm, 50 mJ, 6.5 ns pulse from a Nd:YAG laser beam, and resulting images of the ablation plume can be seen in Figure 5.3.

For an ionization process to occur, an electron from a bound state of the material must be excited into the continuum. The process of ionization can be a function of the multi-photon adsorption process or direct if one photon is of sufficient energy. In a non-metal, or insulator, that does not have an unlimited number of allowed states, the ionization process occurs through the absorption of a photon to excite an electron to a virtual state. If the next incoming photon is present before the relaxation, i.e. if the photon flux is high enough, the electron will be promoted to a continuum of states. If after the first ionization process there is a second excitation of an electron, a bond can be broken leading to ablation, the removal of the material. Any photon flux not used in the initial ionization will be absorbed by the plasma and heat it. For RDX, no excited state exists 4.66 eV (the energy of the 266 nm photon) above the bound states. Therefore the process must be a multiphoton absorption initially for the ionization to occur. Once formed, the plasma, acting like a metal, will be heated in a first-order linear process.

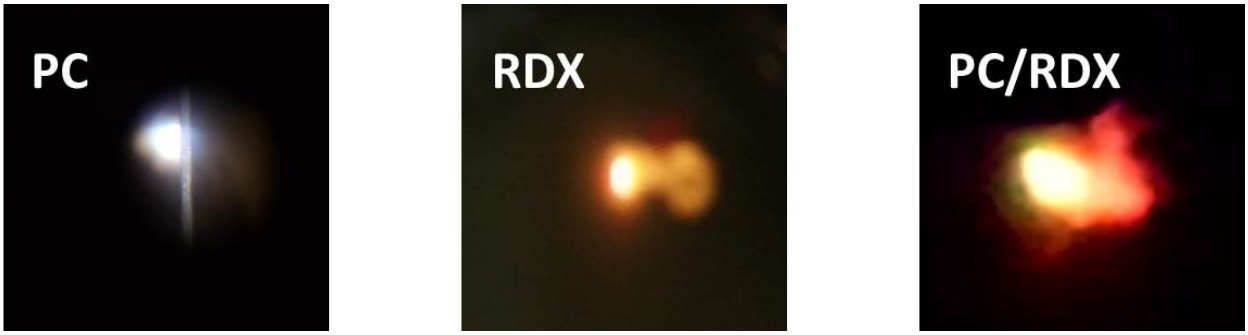

Figure 5.3. Laser induced plasma plume images

When the laser pulse is highly focused (high fluence) the photon density is greater. The fluence dependence therefore also directly affects the amount of material ablated. A tightly focused beam will have a smaller diameter spot size on the material, but the depth at which it will penetrate the material will be greater. A widely focused beam will therefore be spread out farther on the surface and not penetrate as deep. The spot size, pit area, and volume of material removed are directly related to the fluence. When the increase in area is not linear, the $A = \pi r^2$ dependence on the ablation process means that depth will be lost faster than any gain in width.

5.2 Experimental

5.2.1 Sample preparation

Thin films of RDX were prepared by the nebulizing spray technique[39] as depicted in Figure 5.4 and explained in detail in Chapter 2. A 10 mL solution of 5 mg/mL of RDX in acetonitrile was pumped from the syringe at a rate of 1 mL/h through the 32 GA stainless – steel capillary with 20 psi (138 kPa) of Nitrogen as the carrier gas. The capillary to sample distance was set at 41.28 mm for all RDX samples. The RDX solution was sprayed onto 2" sapphire and borosilicate glass wafers either in a dot pattern or one continuous thin film. Wafers with 70 equally spaced dots were sprayed onto a 2" wafer by use of a two axis positioning system. Uniform thin films were prepared by moving the nozzle from the center to the edge over 10 hours in 255 incremental time steps, with the deposition time of each step dependent upon the circumference of the ring at that deposited step. The dot pattern allowed thicker regions of RDX to be deposited over the wafer area with less wasted material in regions between laser shots. Examples of both deposition methods are shown in Figure 5.5.

Thin films of sucrose were prepared as a "blank" molecular solid, as a non-energetic material in comparison to RDX. They were prepared by drop casting a 1:1 solution of table sugar in water onto a wafer and allowed to dry overnight. Polycarbonate films in 25.4 μm thickness were used as received from McMaster-Carr after removing the protective covering.

Polycarbonate (PC) overlays on thin films were prepared by first preparing the RDX film. A PC solution of 30 mg/mL was prepared in dichloromethane (DCM) for spin coating of the RDX films. A 2 mL volume of the PC solution was spread out over the RDX film and spun at 500 rpm for 5 s followed by 1500 rpm for 45s (Figure 5.6). This resulting PC overlayer deposited in this manner was previously determined to be 0.6μm thick.[40]

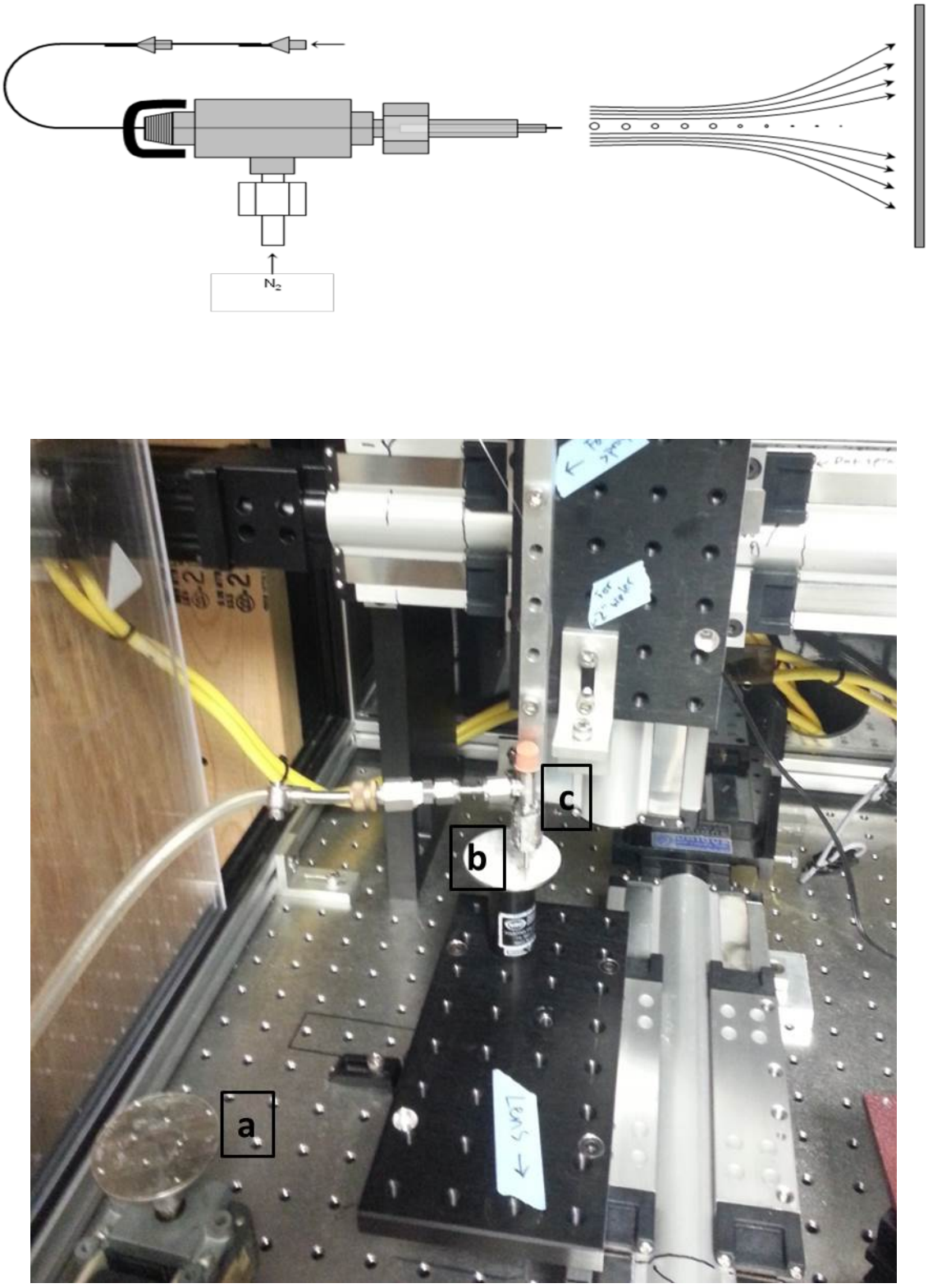

Figure 5.4. Schematic depiction of nebulizing sprayer operation (top) and an image of sprayer in practice (bottom) preparing a thin film with the rotating chuck for uniform films (a), the sample (b), and the sprayer (c)

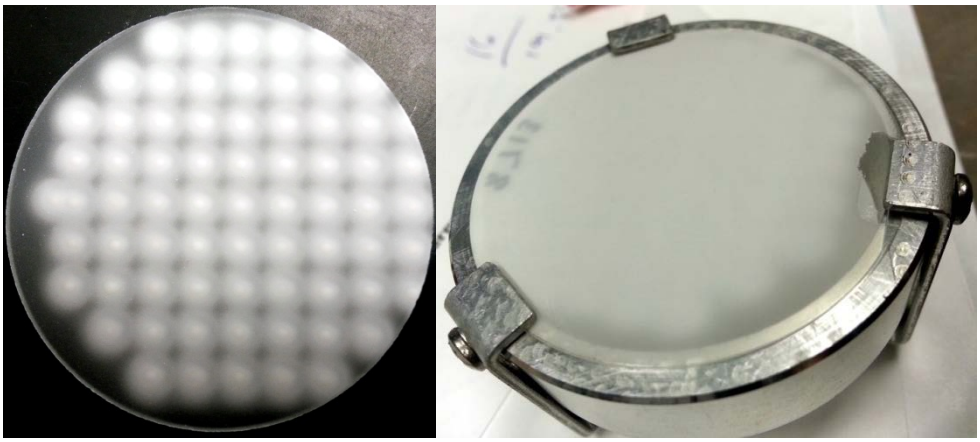

Figure 5.5. As prepared thin films of RDX. Dot pattern (left) and uniform thin film (right)

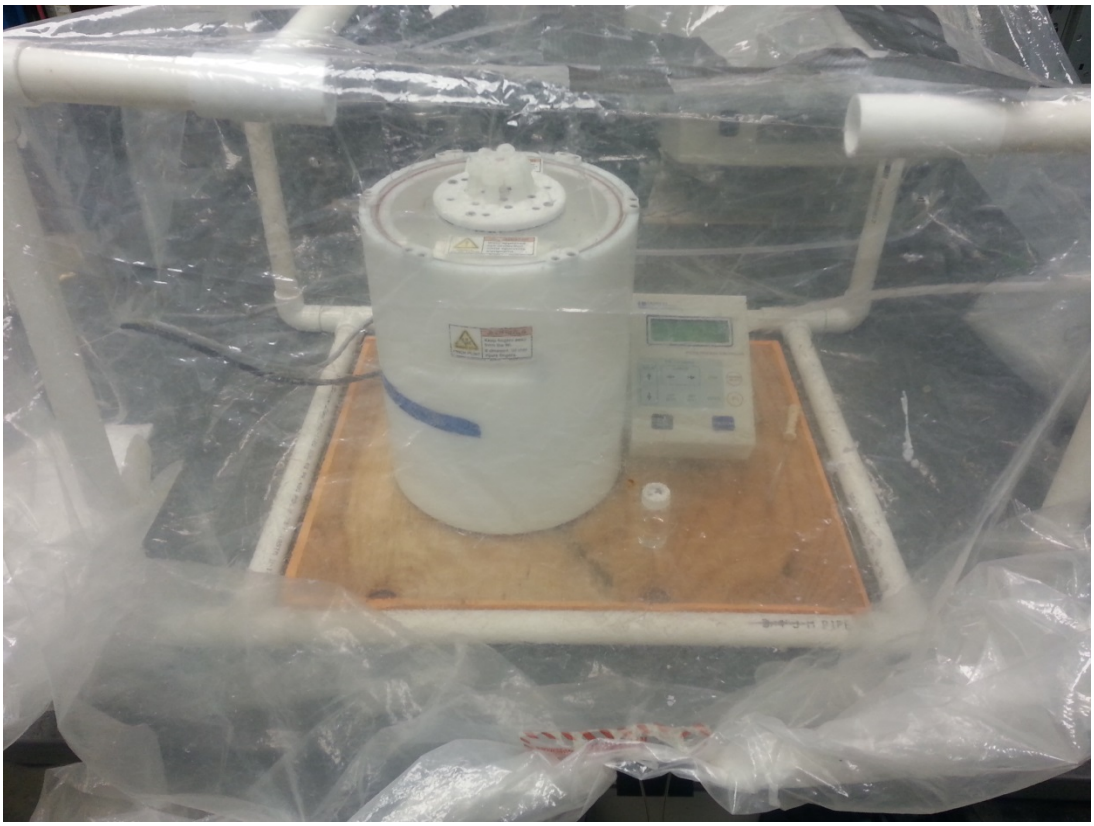

Figure 5.6. Spin-coating apparatus used to produce the polymer overlay on nebulizing sprayed thin films

5.2.2 Thin film diagnostics

Inspection of thin films prior to ablation was done through optical microscopic analysis (Figure 5.7) on the Craic microspectrophotometer to ensure a constant ~50% porosity of the film. Thickness measurements were made using the CRAIC microspectrophotometer for absorbance. The positioning camera on the SEM was used to obtain a high resolution side profile image of an RDX wafer (Figure 5.8) and 3D Laser scanning microscopy[41] (see section 5.3.3). Mass measurements were taken of all films in between spraying of layers, before ablation events, and after the laser ablation experiments.

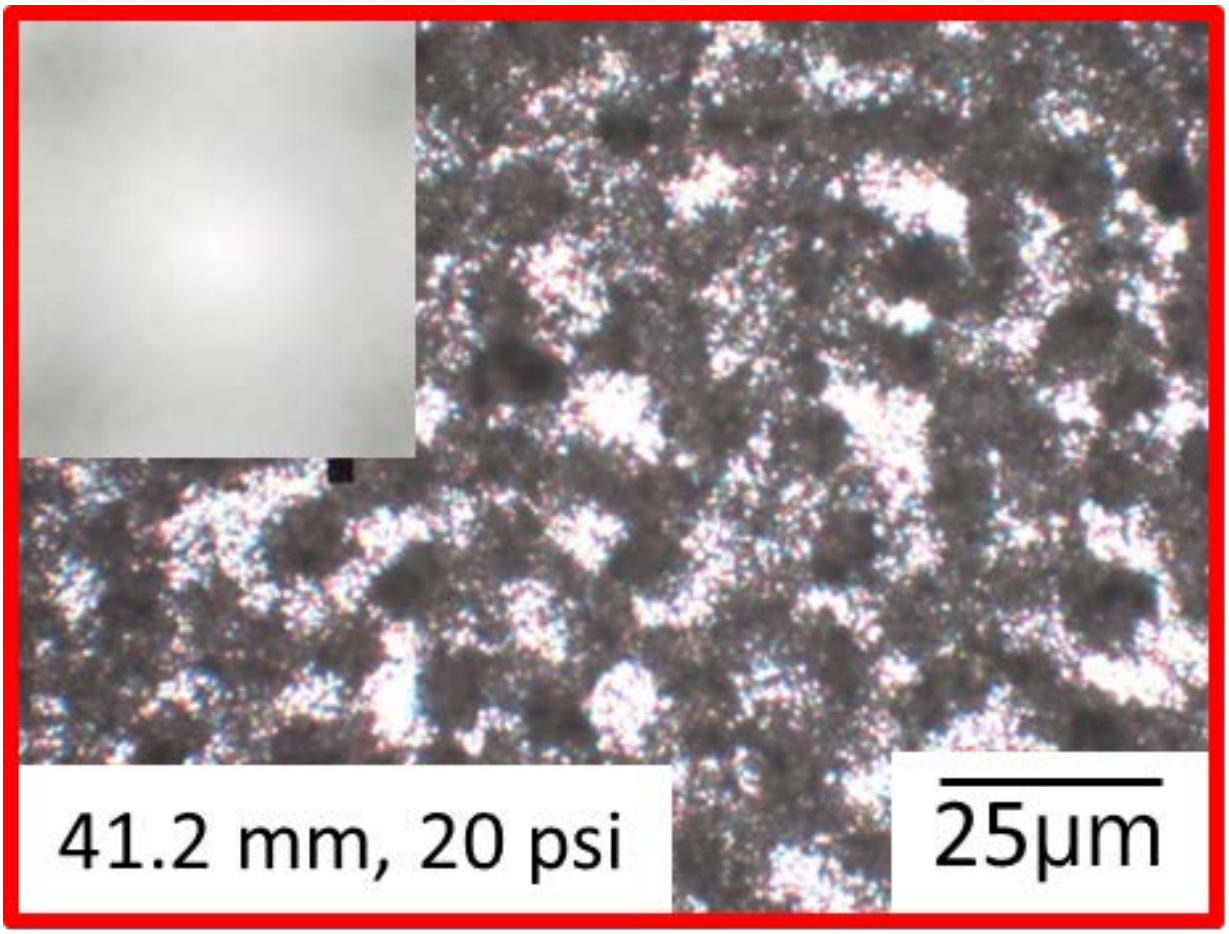

Figure 5.7. Optical microscope image showing approximate 50% porosity in prepared RDX sample

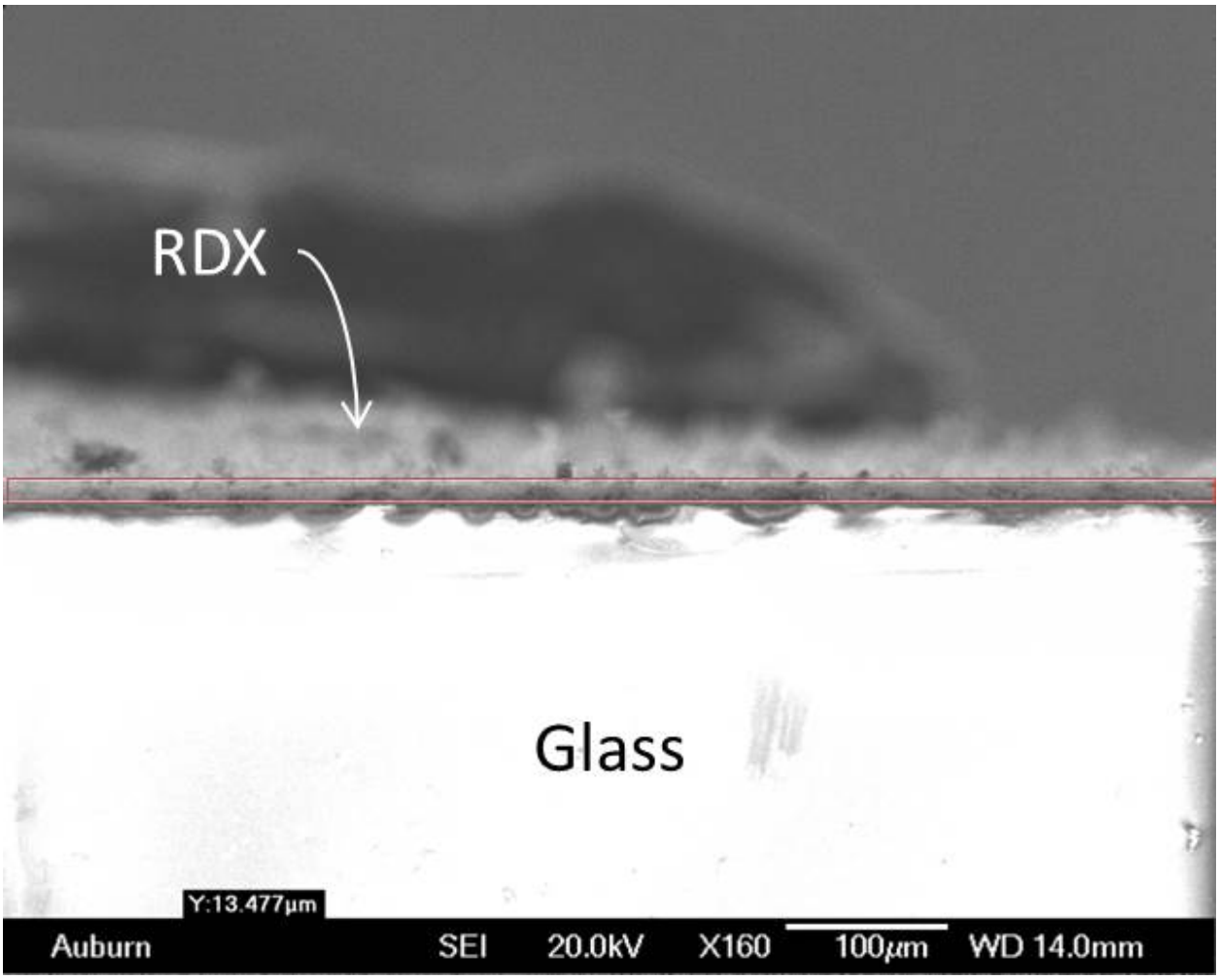

Figure 5.8. Image obtained with SEM camera, the side profile of an RDX wafer showing film thickness of 13.5 µm

5.2.3 Instrumentation

A Nd:YAG Continuum Inlite III-10 laser system, operating on the fourth harmonic at 266 nm, with a 50 mJ, 6.5 ns pulse was used for all ablation events. With a 120mm focal length lens, and a lens to sample distance of 90 mm, the laser pulse was focused to a spot size of 1.25 mm in diameter in all experiments where single shot dosage was required. Control of laser firing was done by externally triggering the pulse either manually or through software to collect all 70 shots on the wafer successively. Sample movement was always controlled using the YZ axes through software for the Parker-Dadaell system. All timing was accomplished through function generators monitored on an oscilloscope. Fluence dependent measurements were made by moving the lens using the x-axis of the Parker-Daedell translation system. The custom written program described in Chapter 2, and detailed in Appendix 1 was used to control all individual software packages and experimental data acquisition. Each wafer was ultimately ablated with 70, evenly spaced (5 mm), laser shots

5.3 Results

5.3.1 Optical images of wafers after laser ablation

Images of the wafers as previously described are shown in Figure 5.9. All wafers were imaged from a constant height on a black background. Ablation pits can be seen where the laser irradiated the surface. The polycarbonate sample shows no evidence of melting between areas of laser irradiation. The edges appear sharp when investigated under a microscope. The only spots visible on the PC are directly where the laser beam hit the surface. The investigation of the optical images of bare RDX and PC/RDX, reveal a noticeable difference in films post ablation. Pits on the PC/RDX sample have a cylindrical shape whereas the bare RDX pits looked crater shaped.

Before irradiation, the RDX film shown in the top right of Figure 5.9 as Bare RDX is completely uniform in nature. After ablation, the bare RDX sample shows pits with additional rings surrounding them where the film appears to be thinned due to heating. After ablation, there is a darkened general region on the center of the bare RDX wafer. This suggests that there are large, thinned, regions where the laser pulse was not incident upon the material. The image shows that the level of transparency of the center area of the wafer is similar to the level of transparency of the exterior pits. On a microscopic level the pits are larger than the beam diameter and crater-like in nature with thinning sloped edges as depicted in Figure 5.9.

Some of the PC coated RDX (PC/RDX) pits in Figure 5.9 are nearly identical in nature, with sharp edges on the microscopic level (Figure 5.10), and no thinning outside of the ablation pit region. Additionally in the PC coated films, 86% show a breakthrough with a complete removal of material, where the laser pulse irradiated the film on the wafer. Aside from two select

cases in the RDX film that the pits may have fractured, the PC/RDX wafer is the only sample where complete removal has taken place in any of the cases.

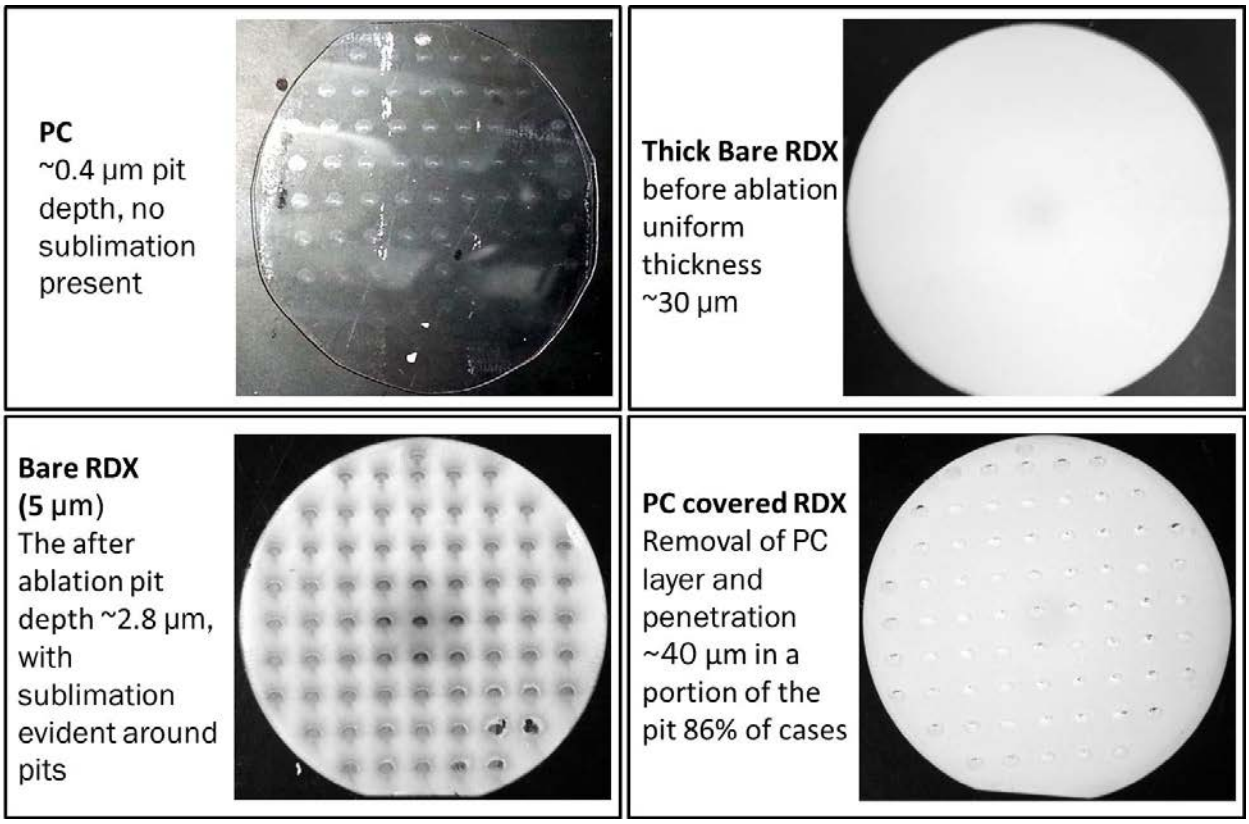

Figure 5.9. Images of samples before and after laser ablation

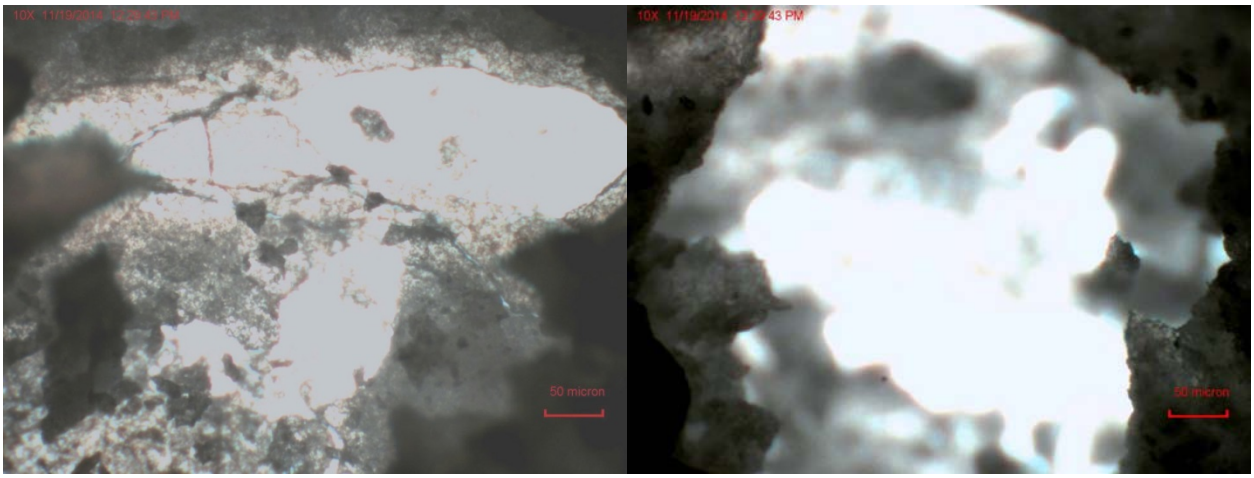

Figure 5.10. Microscope images of RDX crater (left) and PC/RDX pit (right)

5.3.2 Mass loss from laser ablation

As a form of measurement of material removal, measurements of mass before and after laser ablation were made. By assuming uniform mass loss from each ablation shot, the total mass loss from the wafer was divided by 70 shots and is shown in the second column in Table 5.1. The mass of RDX per shot seemed unusually high and per the visual evidence in Figure 5.9, there was evidence of sublimation, so two further estimates were made. Using standard densities, the depth per shot was estimated solely from the calculated mass loss and an assumed pit diameter of 1.25 mm, which is shown in column 3. As was seen in the bare RDX wafer after ablation, the pits were larger and material loss came from outside the area the laser beam irradiated. Therefore, a second estimate shown in column 4 took into account the effects of sublimation. It estimated the depth, excluding sublimation contributions, by attributing only 11% of the material loss to be due to direct laser irradiation rather than induced by the radiation from the plasma plume.[42] RDX was the only sample that showed sublimation and is given a further estimate. The measured masses hint at a discrepancy in material removal that needed to be further investigated.

Table 5.1. Material removed as a function of measured mass loss and standard density

	µg/shot	**µm/shot (based on mass loss)**	**µm/shot (neglecting sublimation)**
Polycarbonate	0.6	0.4	-
Bare RDX	58.7	25.9	2.8 (6.4µg)
PC coated RDX	19.0	7.9	-
PC coated Sucrose	4.9	2.1	-

5.3.3 3D laser scanning microscopy

To further study the pit geometries, depth of ablation, sublimation and material removal, surface measurements and images were taken with 3D laser scanning microscopy (Keyence VKX).[41] The ability of this instrument allowed large scan area measurements to be performed to detail the pit depth, surrounding material deformation, surface perturbation and detailed measurements to be made. The ringed structure seen in the top image in Figure 5.11 of polycarbonate is evidence of portions of the beam that are of sufficient energy to ionize the sample in that region. No significant ablation depth of the PC film has been achieved as evidenced by the small change in the colorimetric scale. The middle image of RDX shows sloped edges due to sublimation, and no breakthrough on a 5 μm thin film of bare RDX. The bottom image of PC/RDX shows a 40 μm film of RDX coated in a 0.6 μm thick PC film. The resulting ablation depth in this film orientation is completely through the 40 μm RDX film and the PC overlayer shown by the large hole in the film. The protruding edges of the pit are due to the reaction blast exiting the pit volume and blistering the edges. There are well defined vertical walls and no evidence of sublimation.

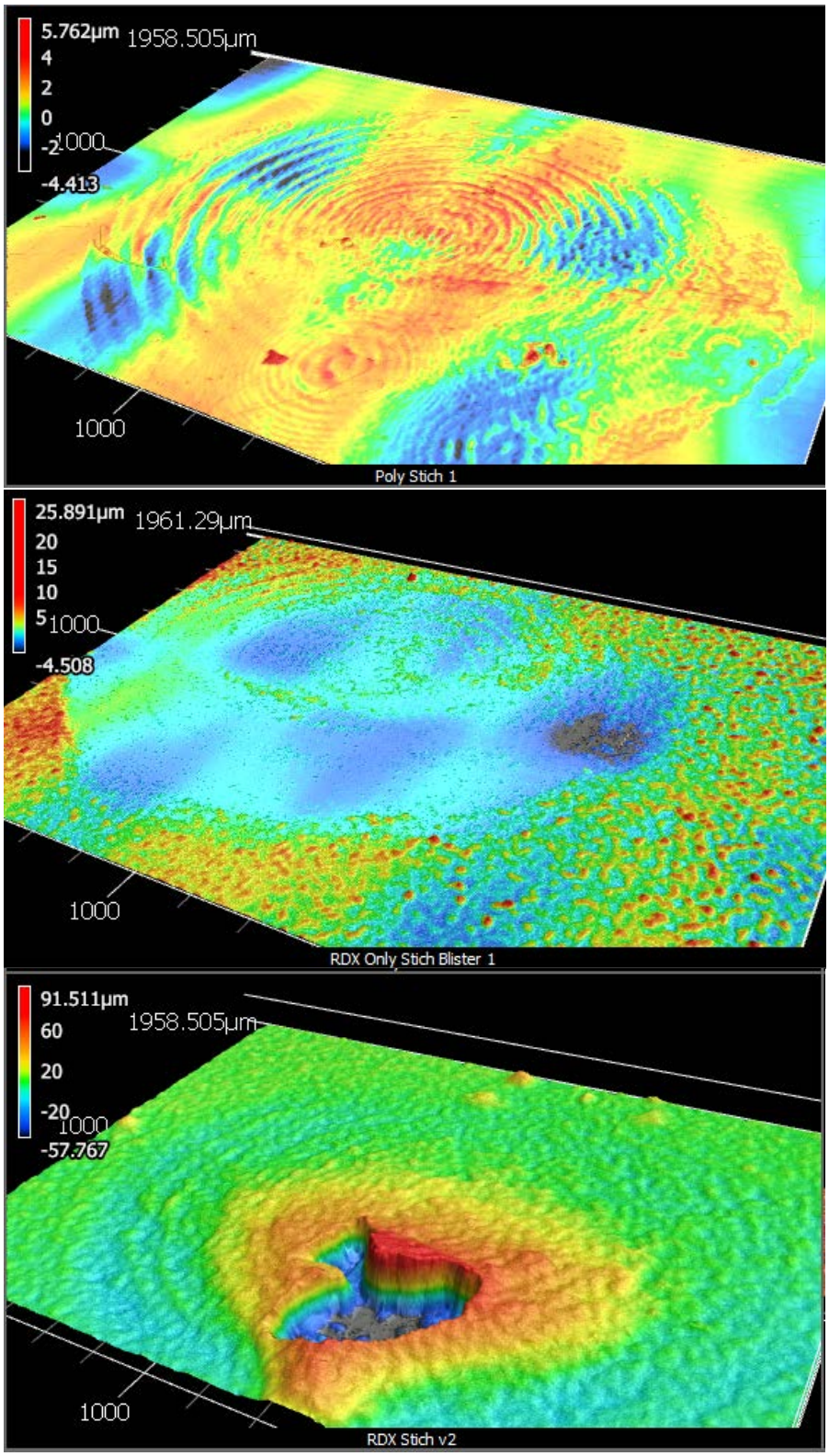

Figure 5.11. Post ablation pits of a sample – wide representation for (top to bottom) PC, RDX, and PC/RDX

Upon further inspection, as is seen in Figures 5.11 and 5.12, there is residual material at the bottom of the pit. This is likely due to sublimation or fragmented portions of the film. The anisotropic edges support the idea that that a chemical reaction propagated with directionality from the surface to the substrate.

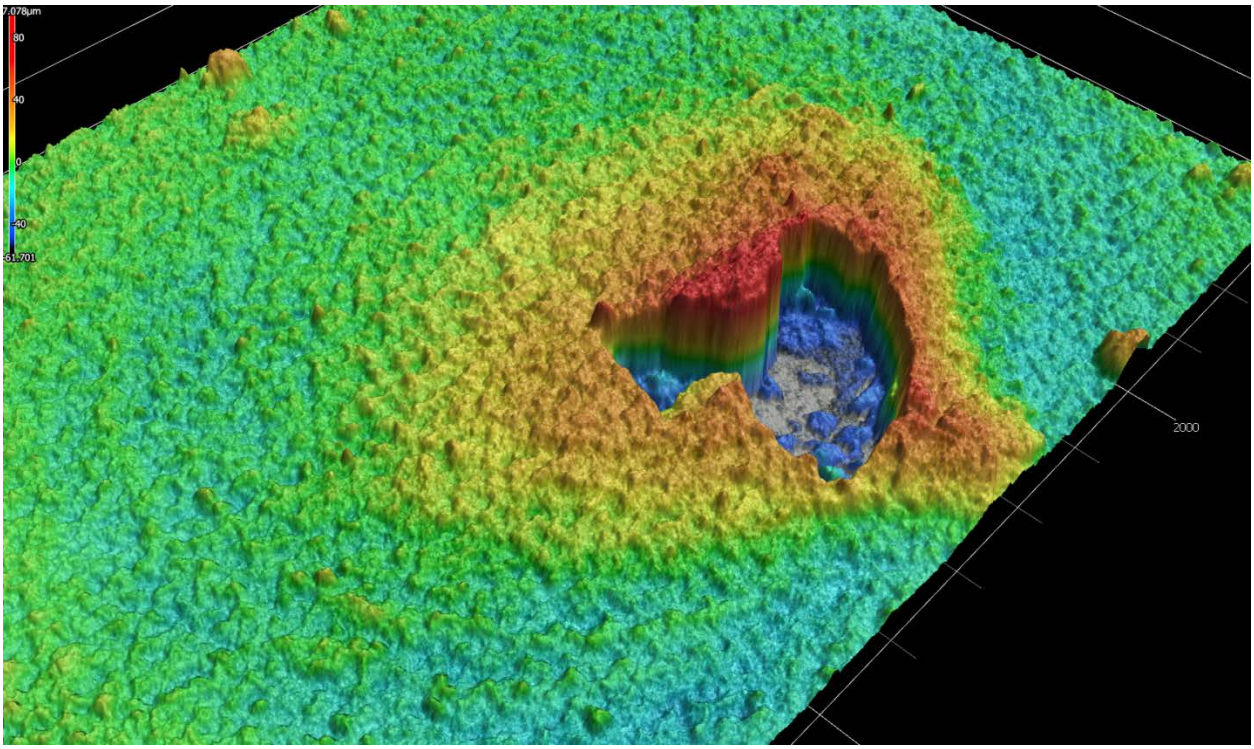

Figure 5.12. Post ablation pit of an PC/RDX film. There is evidence of sharply defined edges, a complete ablation of 40 µm of RDX, and no sublimation

5.4 Discussion

5.4.1 Primary material loss mechanisms

The simplest way one could measure material removal is by determining the changes in mass as the results in Table 5.1 show. As evidenced by these values, the assumptions about the locations and mechanisms of material loss create differing results. The assumption that all of the mass loss comes only from the location of laser irradiation holds true in cases where sublimation does not occur. This assumption fails for the bare RDX sample and various other assumptions to

account for material loss through sublimation have to be made. Two of the most significant mechanistic differences that influence the results are the thickness of the films and resulting pit geometry shown in Figure 5.13. Bare RDX is 4.7 μm thick. The only region where the RDX is completely removed is the centermost portion. The PC/RDX film has a 0.6 μm PC layer that was deposited on top of a 39.5 μm thick RDX layer making it 8x thicker than the bare RDX film. A significant portion of all 70 PC/RDX pit material is removed, with 60 of the shots making a complete breakthrough to the substrate surface.

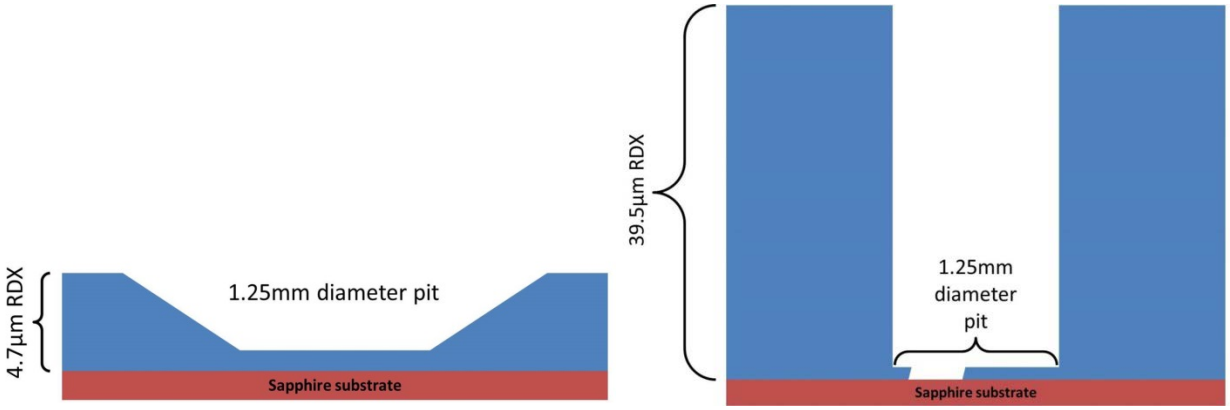

Figure 5.13. Schematic showing differences in ablation geometry between RDX crater (left) and PC/RDX pit (right)

When the laser irradiates the film, the photons directly ionize the material at the surface forming a plasma. Part of the pulse heats the plasma, which shields the material from further laser irradiation. In the case of RDX, the hot radiating plasma that is formed is a few millimeters away from the surface of the material directing heat towards the surface which leads to sublimation. In PC and PC/RDX the polycarbonate is absorbing this radiation and thus does not sublime. Instead the reactive PC plasma propagates through the underlying RDX and chemically contributes to material removal. Mechanistically then, material can be removed through direct laser irradiation, sublimation, or when possible an additional chemical reaction.

5.4.2 Secondary material loss mechanisms

Why these differences occur may be related to the specific mechanisms of removal or due to material differences. If heating is taking place leading to material removal, the melting temperature might be an issue. However, the melting temperatures of RDX and PC are 192° C and 155° C, respectively. Therefore that argument is invalid as RDX has a higher melting point. And considering the high initial plasma temperatures to be around ~10^3 K,[22] those melting temperatures are negligible in comparison. The larger difference is in the molecular structure. The RDX film is a crystalline structure made of small molecular units. The polymeric nature of PC, with long, inter-woven chains and stronger covalent bonds shield the bare RDX from back radiation and any type of sublimation. The radiation from the initial plasma plume radiates visible and infrared radiation in all directions (Chapters 3 and 4), including back onto the surface of the film. The only film that shows evidence of sublimation is RDX with its crater – like pits. This difference can likely be attributed to sublimation on the RDX film, not present on the others, and also attempt to account for the difference in mass loss that is observed.

Using Figure 5.13 as an example of what was occurring in the sublimation of bare RDX, the estimated sublimed material removed from the edges, not the pit, was calculated. The volume of the sloped ring was estimated with the assumption that the interior radius was 1.25 mm, the diameter of the laser pulse. This led to an estimate that the extra material removed from the pit through sublimation was equal to 80% of the initial material mass loss. This difference is then representative of the observed increase in mass loss of RDX films shows in Table 5.1, column 1.

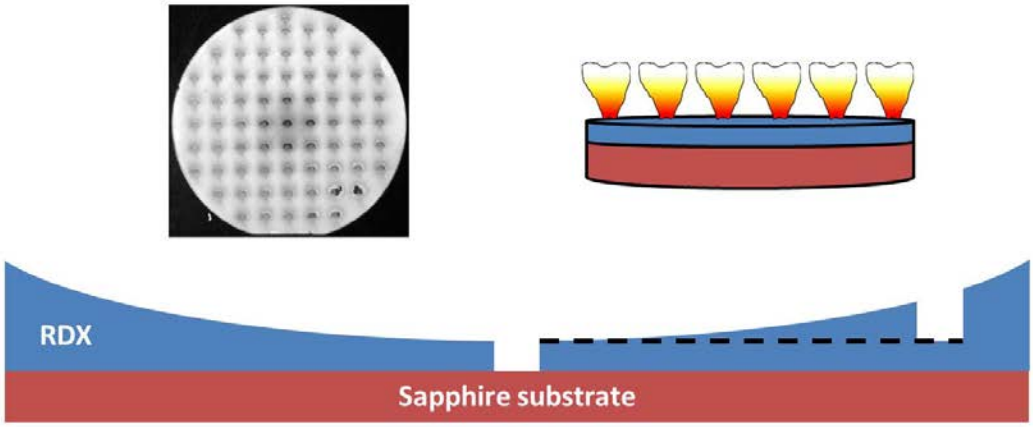

Figure 5.14. Sublimation of RDX as contributed by increased plume radiation over entire sample surface

Examining the RDX wafer as a whole it can be noticed that a thinning is taking place across the entire surface, more significantly in the center than on the edges. The center is also the region of the wafer subject to the greatest amount of laser irradiation during the course of 70 shots. By visually modeling the 70 plumes on the surface of the wafer (Figure 5.14), with each 1.5mm above the surface, they are emitting heat uniformly in all directions. The cumulative effect of this radiation and removal of the material is proportional to the heat flux at each point of a plume. This can be estimated by the following equation:

$$Material\ removed = \sum \left\{ a \times \left[\frac{1}{(x_i - x)^2 + (y_i - y)^2 + (z_i - z)^2} \right] \right\} \quad (5.2)$$

Equation 5.2 shows the fraction of material removed at any point on the wafer in the *x, y, and z* coordinate plane, with x_i, y_i, and z_i being the plume locations. Taking *a*, the proportionality constant to be 1, the amount of material removed from a location can be calculated. Using the distances of the pit locations and the equation above the material removed can be defined as 0.77 for the region between a central pit and one of the four pits surrounding it (point a in Figure 5.15). An estimate of a point in the center of a pit, directly under a plume, on the outermost edge

of the wafer (point b in Figure 5.15) is calculated to be 0.79. Looking only at the effects of sublimation due to additive plume radiation, this model is also in agreement with the observed visible film transparency in the center of the wafer versus the center of the edge pit. Schematically this is represented in Figure 5.15 below, for bare RDX, the thinned centermost region between pits was of the same transparency as the bottom of a pit on the outer edge (Figure 5.9). Incorporating the 4.7 μm known film thickness at the edge of the wafer where the RDX is mostly undisturbed, and an edge to interior (point c to a in Figure 5.15) pit material removal ratio of 0.46/0.79, the interior film thickness has thinned to an estimated 2.9 μm. From Table 5.1, the adjusted sublimation corrected depth per shot was 2.8 μm. These two estimates are then in good agreement considering that most of the material is removed on the centermost laser shots.

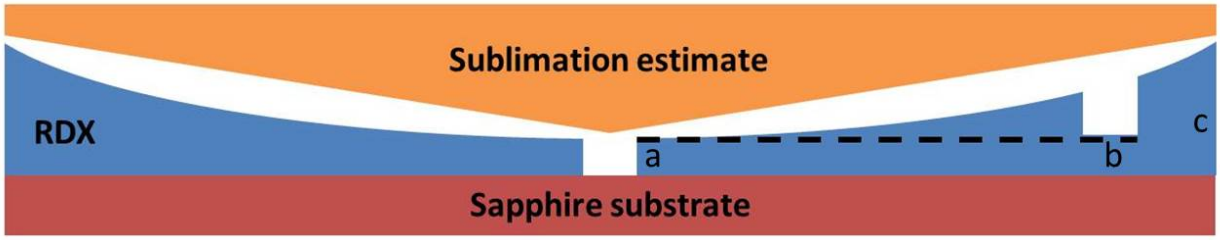

Figure 5.15. Sublimation estimate over surface of entire RDX wafer

Furthermore, the mass losses and adjusted mass loss due to sublimation have an effect on the overall material loss values. Due to these sublimation estimates, the argument for extra RDX material removed can be supported herein in that the majority of RDX is then removed through sublimation rather than a laser ablation process. The total volume of RDX sublimed can be estimated as 1.96×10^{9} μm^{3}, a mass of 3.57 mg. Per the mass measurements of the wafers shown in Table 5.1, 4.11 mg of RDX were lost after all 70 laser shots. These sublimation estimates account for 87% material loss on the entire wafer. This is in agreement with all previous arguments of sublimation versus an ablative process. This RDX ablation phenomena was

investigated in detail by *Sun et. al.*[42] by studying the ablation process in a closed cell, and measuring the acetonitrile rinse with IR spectroscopy revealing that >83% of the molecular RDX was recovered intact. Only 11% of the material removed was attributed to gaseous products from the RDX laser ablation process.

The differences in the pit shape from crater – like to cylindrical in RDX and PC/RDX extend beyond their two-dimensional character. Microscopic images begin to show that the interior of the pits is also different in shape. One of the most significant contributions to this difference is the amount of material present and then removed. The film thickness of RDX is 4.7 μm and PC/RDX is 39.5 μm RDX with a 0.6 μm PC layer deposited on top. Yet as shown in the images of the films and estimated in the sublimation calculations in previous sections of this chapter, hardly any of the bare RDX film is removed through a single ablation shot and 86% of the PC/RDX shots have a complete breakthrough. The film is more than 8x thicker, and in 60 shots, it is all removed for at least some portion of the pit. The PC/RDX film being 8x thicker, also means that the volume is more than 8x greater also, 4.85×10^{-2} μm^3 compared to 5.77×10^{-3} μm^3 for bare RDX. But, laser ablation of bare RDX never has this amount of material removed.

This could suggest that the difference in material removal is due to a chemical process rather than an ablation mechanism. The loss of material in the case of PC/RDX occurs only in the location of laser irradiation. The PC surrounding the pit could be responsible for shielding any further sublimation, but the entirety of material loss 19.0 μg/shot versus 6.4 μg/shot (sublimation adjusted) for bare RDX. This means that of that mass, there is a propagation of removal of the volume of material beneath the irradiated spot of <4.7 μm in RDX whereas in the PC/RDX case, a volume of material removal is propagated for a depth of >39.5 μm. The only sublimation that may be occurring in the PC/RDX is on the sidewalls of the pits or at the bottom.

In all cases of PC/RDX films however, with RDX films that ranged in thickness from 3-39.5 μm, 86% of shots removed a portion of the entire thickness. The increased removal of material with a polymer overlay does not seem to be dependent on material thickness.

The increased material removal with the PC overlay is similar to the positive contributions of ETC ignition. In that case, the hydrogen ion was the important chemical species responsible for the conversion of the RDX molecule into 9 gaseous molecules. For the laser induced plasma event, the difference in ablation may be due to the chemical composition of the plasma as detailed by Table 5.2 below.

Table 5.2. Variation in plasma composition between RDX and Polycarbonate

Bare RDX	**PC coated RDX**
$C_3H_6N_6O_6$	$C_{16}H_{14}O_3$
28% Hydrogen	42% Hydrogen
28% Oxygen	9% Oxygen
6.4 μg converted to plasma	19.0 μg converted to plasma

Here it can be seen that in the PC overlay, there is a fuel to oxidizer level of 4.7:1 versus 1:1 in RDX. This higher concentration of reactive hydrogen species, purely increased by the change in the chemical composition of the plasma could greatly contribute to the higher reactivity of the plasma, increasing the material removed by contributing with a chemical mechanism of a plasma propellant interaction.

5.4.3 Non-energetic sucrose samples

Any time a sample is irradiated with a high energy laser beam, the adsorption process undoubtedly leads to increased pressures and temperatures as the material is ionized.[43] The newly formed gas and plasma are rapidly expanding outwards away from the sample surface. The rate at which they are expanding is on the order of tens of kilometers per second.[44,45] This

compresses the air ahead. These outward expanding forces are coupled with increased back pressures into the sample surface to sustain the strong fronts moving in the opposite direction. When the laser induced plasma and the associated pressure gradients form away from the target, there are back pressures then incident upon the sample (RDX) as well. It is well known that one of the initiation mechanisms of a secondary explosive such as RDX is shock.[46,47] To test against the possibility that the increased removal of RDX when coated with the PC was a shock pressure driven mechanism rather than a chemical mechanism, thin film samples of sucrose (a non-energetic molecular solid) were prepared and coated with PC. When ablated, only a mass of 4.9μg/shot was removed, less than that observed from bare RDX and PC/RDX. This further suggests that it is not a shock induced phenomena that is removing extra material in the PC/RDX case. Despite the increased number of hydrogen atoms present, sucrose, which is not an EM like RDX, does not appear to rapidly decompose under the presence of H•, as is seen in RDX.[13]

5.5 Conclusion

The UV laser induced plasma ablation of thin films of PC, RDX, PC/RDX and PC/Sucrose were investigated in this work. The RDX film shows 2.9 μm pits under laser irradiation. Sublimation plays a significant role in the removal of bare RDX films whereas there is evidence no sublimation is observed in any of the other films including the PC/RDX. The addition of a PC overlayer onto RDX films results in complete removal of a portion of the volume beneath the irradiated spot in 86% of the cases. This is indicative of a chemical process involving the greater reactive PC plasma interacting with the underlying RDX to be responsible for the increased material removal. To rule out mechanisms of shock induced ablation, thin films of sucrose were used as a control to show that the contribution of such processes is negligible. This laser induced plasma propellant interaction could serve as a new approach to military weapons systems.

5.6 References

1. Akhavan, J., *The chemistry of Explosives, Second Edition*. 2004; p 180 pp.
2. Maienschein, J. L. In *Research topics in explosives-a look at explosives behaviors*, 2014, IOP Publishing: p 052027.
3. Fried, L. E.; Ruggiero, A. J., *Journal of Physical Chemistry* **1994,** *98*, 9786-9791.
4. Matyáš, R.; Pachman, J., Introduction to Initiating Substances. In *Primary Explosives*, Springer Berlin Heidelberg: 2013; pp 1-10.
5. Tsiaousis, D.; Munn, R. W., *The Journal of chemical physics* **2005,** *122*, 184708.
6. Kuo, K. K.-y.; Acharya, R., *Applications of turbulent and multi-phase combustion*. John Wiley & Sons: 2012.
7. Behrens Jr, R.; Bulusu, S., *The Journal of Physical Chemistry* **1992,** *96*, 8877-8891.
8. Edwards, C. M.; Bourham, M. A.; Gilligan, J. G., *IEEE Trans. Magn.* **1995,** *31*, 404-9.
9. Muller, G. M.; Moore, D. B.; Bernstein, D., *Journal of Applied Physics* **1961,** *32*, 1065.
10. Chaboki, A.; Zelenak, S.; Isle, B., *Magnetics, IEEE Transactions on* **1997,** *33*, 284-288.
11. Beyer, R.; Pesce-Rodriguez, R. In *The response of propellants to plasma radiation*, 2005, IEEE: pp 273-278.
12. Dyvik, J.; Herbig, J.; Appleton, R.; Reilly, J. O.; Shin, J., *Ieee Transactions on Magnetics* **2007,** *43*, 303-307.
13. Valliere, R.; Blumenthal, R., *Journal of Applied Physics* **2006,** *100*, 084904.
14. Blumenthal, R. *Understanding the Plasma-Propellant Interaction through Experimental Modeling*; DTIC Document: 2009.
15. Voevodin, A. A.; Laube, S. J. P.; Walck, S. D.; Solomon, J. S.; Donley, M. S.; Zabinski, J. S., *Journal of applied physics* **1995,** *78*, 4123-4130.

16. Kemp, A. J.; Fiuza, F.; Debayle, A.; Johzaki, T.; Mori, W. B.; Patel, P. K.; Sentoku, Y.; Silva, L. O., *Nuclear Fusion* **2014,** *54*, 054002.

17. Aluker, E. D.; Krechetov, A. G.; Mitrofanov, A. Y.; Zverev, A. S.; Kuklja, M. M., *The Journal of Physical Chemistry C* **2012,** *116*, 24482-24486.

18. Fang, X.; McLuckie, W. G., *Journal of hazardous materials* **2015,** *285*, 375-382.

19. Zhang, S.; Wang, X.; He, M.; Jiang, Y.; Zhang, B.; Hang, W.; Huang, B., *Spectrochimica Acta Part B: Atomic Spectroscopy* **2014,** *97*, 13-33.

20. Maynard, G.; Lambert, F.; Andreev, N.; Robillar, B.; Boudaa, A.; Clerouin, J.; Cros, B.; Lenglet, A.; Mocek, T.; Sebban, S., *Contributions to Plasma Physics* **2007,** *47*, 352-359.

21. Harilal, S. S.; Bindhu, C. V.; Issac, R. C.; Nampoori, V. P. N.; Vallabhan, C. P. G., *Journal of Applied Physics* **1997,** *82*, 2140-2146.

22. Nagayama, K.; Inou, K.; Nakahara, M.; Chiba, A.; Tanimura, S.; Hokamoto, K., *Impact Engineering and Application* **2001,** *1*, 515-519.

23. Farooq, W. A.; Tawfik, W.; Alahmed, Z. A.; Ahmad, K.; Singh, J. P., *Journal of Russian Laser Research* **2014,** *35*, 252-262.

24. Boueri, M.; Baudelet, M.; Yu, J.; Mao, X. L.; Mao, S. S.; Russo, R., *Applied Surface Science* **2009,** *255*, 9566-9571.

25. Boueri, M.; Motto-Ros, V.; Lei, W. Q.; Ma, Q. L.; Zheng, L. J.; Zeng, H. P.; Yu, J., *Applied Spectroscopy* **2011,** *65*, 307-314.

26. Shearer, J. W.; Barnes, W. S., *Physical Review Letters* **1970,** *24*, 92-&.

27. Capitelli, M.; Casavola, A.; Colonna, G.; De Giacomo, A., *Spectrochimica Acta Part B: Atomic Spectroscopy* **2004,** *59*, 271-289.

28. Dong, M.; Chan, G. C. Y.; Mao, X.; Gonzalez, J. J.; Lu, J.; Russo, R. E., *Spectrochimica Acta Part B: Atomic Spectroscopy* **2014,** *100*, 62-69.

29. Baravian, G.; Godart, J.; Sultan, G., *Applied Physics Letters* **1980,** *36*, 415-416.

30. Tozer, B. A., *Physical Review* **1965,** *137*, A1665.

31. Kaw, P. K.; Dawson, J. M., *Physics of Fluids* **1969,** *12*, 2586-&.

32. Cui, Y.; Moore, J. F.; Milasinovic, S.; Liu, Y.; Gordon, R. J.; Hanley, L., *Review of Scientific Instruments* **2012,** *83*, 093702.

33. Rezaei, F.; Tavassoli, S. H., *Physics of Plasmas (1994-present)* **2013,** *20*, 013301.

34. De Giacomo, A.; Dell'Aglio, M.; De Pascale, O.; Gaudiuso, R.; Palleschi, V.; Parigger, C.; Woods, A., *Spectrochimica Acta Part B: Atomic Spectroscopy* **2014,** *100*, 180-188.

35. Ahmad, S. R.; Russell, D. A., *Propellants, Explosives, Pyrotechnics* **2005,** *30*, 131-139.

36. Haas, Y.; Ben-Eliahu, Y.; Welner, S., *Propellants, explosives, pyrotechnics* **1996,** *21*, 258-265.

37. López-Claros, M.; Vadillo, J. M.; Laserna, J. J., *Journal of Analytical Atomic Spectrometry* **2015**.

38. Aluker, E. D.; Krechetov, A. G.; Mitrofanov, A. Y.; Nurmukhametov, D. R.; Kuklja, M. M., *The Journal of Physical Chemistry C* **2011,** *115*, 6893-6901.

39. Orland, A.; Blumenthal, R., *Journal of Propulsion and Power* **2005,** *21*, 571-573.

40. Sun, H., **2011**.

41. Eltinge, E.; America, K. C. o., Micro Analysis Group. In Casper IV, W., Ed. Auburn, AL, 2015.

42. Sun, H.; Blumenthal, R. In *Products Of The Ultraviolet Laser Ablation Of RDX*, *Proceedings of the 43rd JANNAF Combustion Subcommittee Meeting*, 2009; 2009; pp 2009-0105CS.

43. Li, C.; Wang, J.; Wang, X., *Physics Letters A* **2014,** *378*, 3319-3325.

44. Gregorčič, P.; Možina, J., *Optics letters* **2011,** *36*, 2782-2784.

45. Gottfried, J. L., *Physical Chemistry Chemical Physics* **2014,** *16*, 21452-21466.

46. Hua, C.; Zhang, P. J.; Lu, X. J.; Huang, M.; Dai, B.; Fu, H., *Propellants, Explosives, Pyrotechnics* **2013,** *38*, 775-780.

47. Li, T.; Hua, C.; Li, Q., *Propellants, Explosives, Pyrotechnics* **2013,** *38*, 770-774.

Chapter 6

Summary and Conclusions

6.1 A more complete understanding of the laser induced plasma plume expansion process

The mechanisms of formation of ultraviolet laser induced plasmas are extremely convoluted.[1] An overly simplified model used most often is that the high energy pulse of light hits a sample surface and turns that solid into a plasma on the timescale of the laser pulse. In reality there are numerous fundamental processes that occur following expansion of the plasma. Figure 6.1 attempts to give a rough timeline of the main observed events, and the work described herein has contributed to unravel several phenomena not previously described.

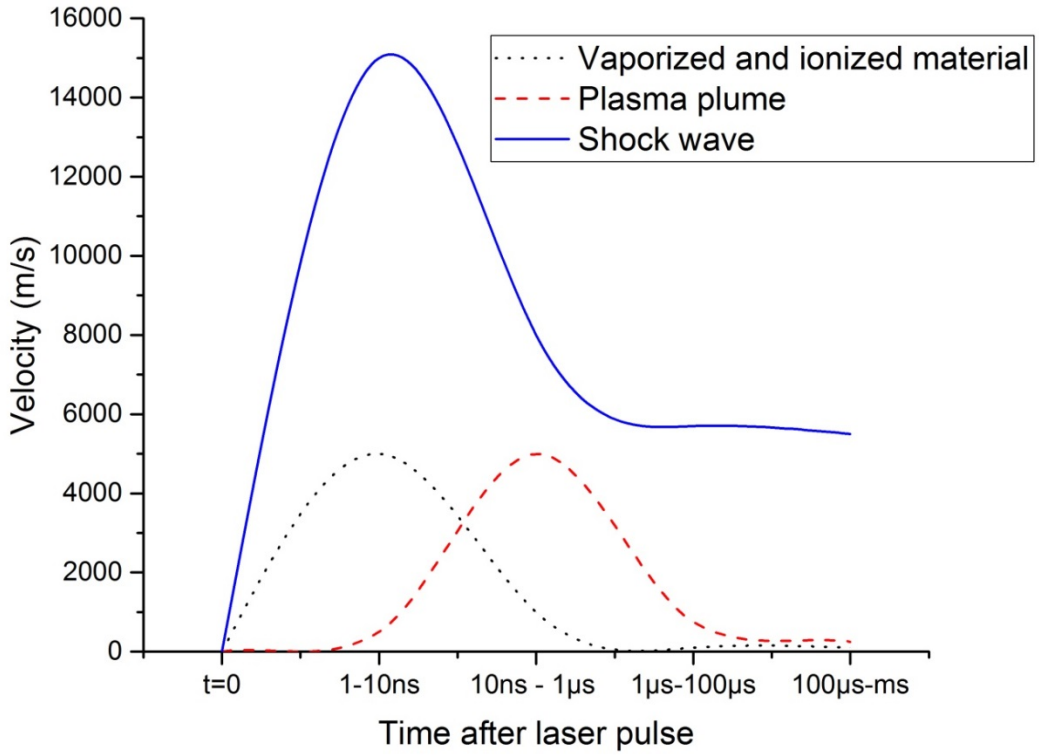

Figure 6.1. LIP expansion timeline

The absorption of the laser pulse is the first step. For a non-metallic solid, such as a polymer or RDX, during the first few nanoseconds of the laser pulse, the excitation process begins. Electrons in the material are promoted to virtual states, and at sufficiently high fluence, a secondary photon further excites electrons into a continuum of states. In these first few nanoseconds, this leads to a localized bond breaking in the material.

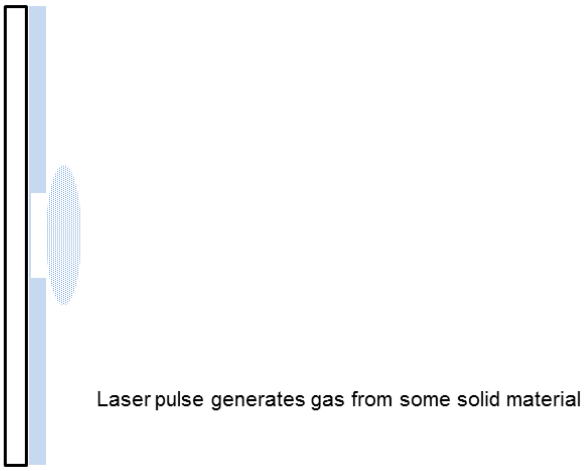

Figure 6.2. Vaporized material generated from laser pulse

The gaseous material is still under illumination which induces further ionization and heating. This rapid gaseous expansion due to the increased pressure proceeds at km/s velocities away from the sample surface creating a shock front in the now compressed ambient gas in front of it. [2-4] The shock is launched from the point of fastest expansion of the plume.

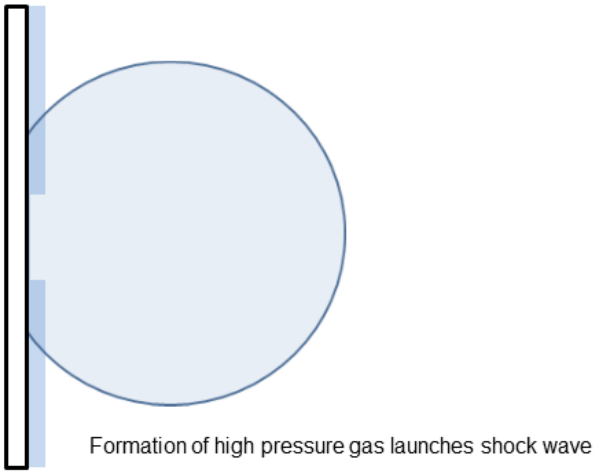

Figure 6.3. High pressure gas due to increased pressure from solid to gaseous material expansion

The vaporized material is still present in front of the laser pulse. Further ionization and heating by photon absorption brings this portion of the material to an opaque plasma state. This initial plasma formation takes place and continues for the duration of the laser pulse as it is continually heated. The remaining radiation from the laser is absorbed almost completely by a first-order heating of the now metal – like plasma. The linear absorption process is much more efficient than the second order ionization of a solid. As the shock is accelerating from the surface, its maximum velocity is that of the plume. The plume eventually stops expanding, but the shock wave continues to move at this initial plasma expansion rate.

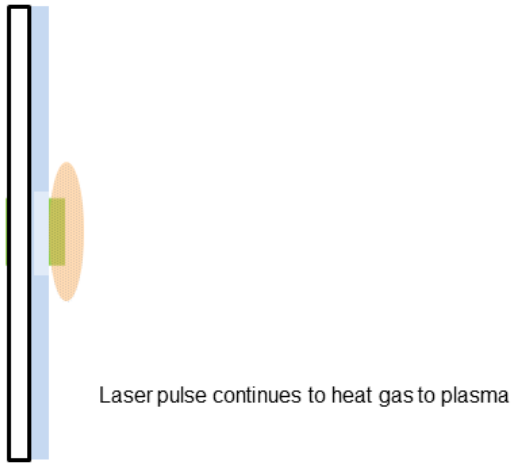

Figure 6.4. Laser heating to and of plasma

As this process is still occurring, the hot plasma radiates heat. As the plasma continues to heat, to ~10^5 K and expand at supersonic velocities, it is emitting light in all directions. The back radiation that is observed from the hot plasma can have strong effects on the materials as was seen in the case of RDX. The ablation process becomes dependent upon the plasma formation, and is driven by different mechanisms in different materials. Sublimation plays no role in any material removal from the polymer samples studied, only the molecular solid, RDX.

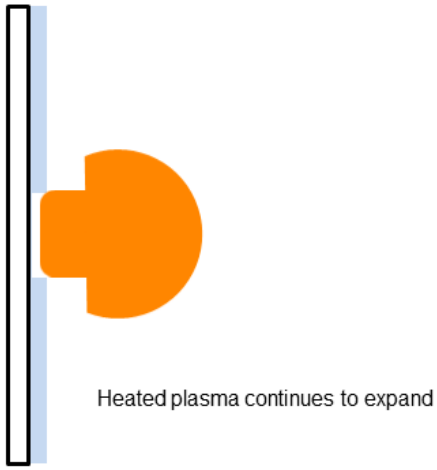

Figure 6.5. Plasma heating and expansion

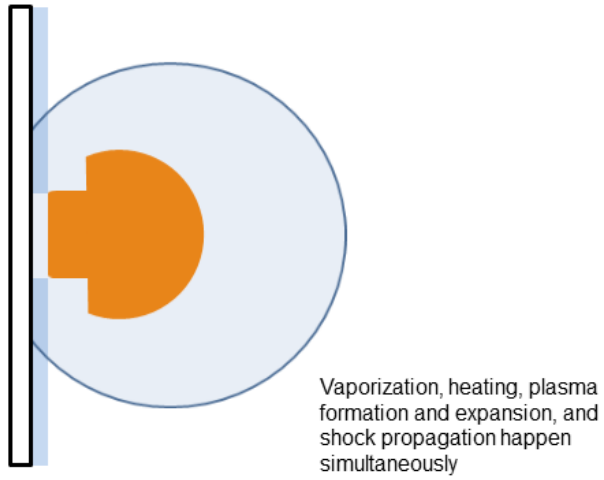

Figure 6.6. The final state of the laser induced plasma formation before cooling begins

6.2 Optically dense plasma phase transition

Within the optically dense plasma is a high density of free electrons, most likely for a UV laser pulse on the order of 10^{16} cm^{-3}. Also, there are initially a large degree of ions and atomic species present. With enough energy from the laser pulse these species will continue to form. After the ns laser pulse has ended, the plasma has expanded to a few cubic millimeters in volume. Expansion ensues with a rapid cooling, and these excited species begin to combine via various recombination and combustion reactions. The plasma is not homogeneous on this time scale. The inhomogeneity is due to the local core of the plasma being the origination point from the vaporized material conversion and its hottest point. This contraction of the hot core leads to a cooler optically thick skin surrounded by a gaseous region. The radiative cooling processes are fast, whereas the expansion is slow. As the expansion takes place, the optically dense outer skin of the plume is the layer that is observed during spectroscopic measurement. The collapsing plasma plume can be observed spectroscopically. As the plasma cools, it reaches a steady-state temperature at the point of maximum expansion. At some point in time, it has lost enough energy

to the surroundings, decreased in electron density, and has been observed to undergo a collapse. At this point, the plasma to gas phase transition is observed.

6.3 Fluence dependent material removal

When focusing the laser light through the lens, the relationship of the distance between the focal point and the sample was deemed to be an important factor in the ablation process. For energetic materials like RDX, the mechanisms of material removal were highly dependent upon this lens to sample distance. At close distances (60 – 70 mm), the material removal process was through only a multi-photon ablation process. Moving the sample closer to the focal point of the lens (80 – 90 mm) allowed the resulting plasma to be heated to a higher degree, and sublimation contributed to the ablation process. For distances near the focal point of the lens (100 – 140 mm) the processes of ablation and sublimation were dominant. However, there was also spectroscopic evidence of reactive plasma species possibly contributing through a chemical interaction. Finally, at 150 mm, past the focal point of the lens, the ablation process still took place, but the air plasma that formed in front of the sample contributed to material removal with the presence of a well – defined shock wave impinging on the surface. These four distinct mechanisms of material removal as a function of fluence are unique to RDX.

6.4 Using laser induced plasmas as an energetic material initiation source

Having an understanding of the laser induced plasma formation, decay, and fluence dependent mechanisms on material removal helped in using this LIP to initiate energetic materials. Using the well-known mechanism of plasma propellant interactions, a polymer overlayer was deposited on top of an RDX thin film. Irradiating the PC film allowed the reactive plasma species to then propagate through the underlying RDX film. Bare RDX when irradiated with a UV laser pulse resulted in a thickness of less than 3 μm of material being ablated.

However, once the PC film was present on top of the RDX, a 40 μm film of RDX was able to be removed in 86% of the cases. This orientation allows the plasma propellant interaction to take place in the initiation of RDX.

6.5 Conclusions

This work provides a better understanding of the laser induced plasma interaction with various materials. An experimental set-up was designed and constructed, allowing laser induced plasmas to be probed on a microsecond time scale with a custom built ultra-fast optical emission spectrometer. The nebulizing spraying technique was expanded upon to coat large area thin films of RDX. The spectroscopic evolution of a decaying plasma plume was observed and involved a phase transition from a plasma to a gas. An understanding of the laser ablation process of removal of material from RDX was established as having four separate dominating mechanisms that were dependent upon the lens to sample distance. An alternative ignition method resembling ETC ignition was suggested by creating an overlay of polycarbonate on RDX resulting in a complete removal 86% of the time.

6.6 Future work

This work would benefit from future studies on a wider variety of samples to obtain a more complete understanding of perhaps what specific molecular contributions are responsible for the continuum radiation that was observed spectroscopically. To increase the spectroscopic understanding of the LIP and the laser ablation process, studying more specific spectral regions with increased resolution could be helpful. Doping materials with salts such as sodium that give intense atomic emission lines could provide an internal atomic probe of electron densities and temperatures to help the understanding about mechanisms of radiation. Finally, the interaction between different polymers and different energetic materials should be further probed to

understand what specific ratios of or which polymers would be optimal for ignition with a laser induced plasma.

6.7 References

1. Motto-Ros, V.; Ma, Q. L.; Grégoire, S.; Lei, W. Q.; Wang, X. C.; Pelascini, F.; Surma, F.; Detalle, V.; Yu, J., *Spectrochimica Acta Part B: Atomic Spectroscopy* **2012,** *74*, 11-17.
2. Li, C.; Wang, J.; Wang, X., *Physics Letters A* **2014,** *378*, 3319-3325.
3. Chen, A.; Jiang, Y.; Liu, H.; Jin, M.; Ding, D., *Physics of Plasmas (1994-present)* **2012,** *19*, 073302.
4. LaHaye, N. L.; Harilal, S. S.; Diwakar, P. K.; Hassanein, A., *Journal of Analytical Atomic Spectrometry* **2014,** *29*, 2267-2274.

Appendix 1

AutoIt code to collect spectra

```
Sleep(10000)
$svar= "PC_060215_20usw_"
;sample name
$svar1="100_"
;delay
  For $i = 1 To 5
          ;number of instances
           WinActivate("SeriCon - New")
           WinWaitActive("SeriCon - New", "Send")
           Send("{ENTER}")
           ;fire laser
           Sleep(20000)
           WinActivate("SonyIIDC - [No Sony camera in system]")
           WinWaitActive("SonyIIDC - [No Sony camera in system]")
           Sleep(2500)
           ControlClick("SonyIIDC - [No Sony camera in system]", "SAVE", 1170)
           WinWaitActive("Save As")
           Sleep(2500)
           Send($svar & $svar1 & $i)
           Sleep(2500)
           Send("{ENTER}")
           ;save *.bmp image of spectra
           Sleep(5000)
  Next
  ;repeat for $i
```

AutoIt code to collect photodiode trace and spectra at various LSD

```
Sleep(10000)
$svar= "AN_060315_"
;sample name
$svar1 = "DMC Smart Terminal - [70 shot RDX wafer.dmc]"
;Name of motion control expt
$j = 60
;x axis position start
$k = 150
;x axis position end
Do
   WinActivate($svar1)
   WinWaitActive($svar1)
   ControlSend($svar1, "", "[Class:RichEdit20A; Instance:1]", "PAX=(" & $j & "*400)")
   Send("{ENTER}")
   ;define lens position
   Sleep(1000)
   ControlSend($svar1, "", "[Class:RichEdit20A; Instance:1]", "BGX")
   Sleep(1000)
   Send("{ENTER}")
   ;move lens to position
   Sleep(1000)
  For $i = 1 To 7
         ;number of instances
           WinActivate("SeriCon - New")
           WinWaitActive("SeriCon - New", "Send")
           Send("{ENTER}")
           ;fire laser
           Sleep(20000)
           WinActivate("SonyIIDC - [No Sony camera in system]")
           WinWaitActive("SonyIIDC - [No Sony camera in system]")
           Sleep(2500)
           ControlClick("SonyIIDC - [No Sony camera in system]", "SAVE", 1170)
           WinWaitActive("Save As")
           Sleep(2500)
           Send($j & "mm_" & $svar & $i)
           Sleep(2500)
           Send("{ENTER}")
           ;save *.bmp image of collected spectra
           Sleep(5000)
           WinActivate("OpenChoice Desktop")
           WinWaitActive("OpenChoice Desktop")
           Send("^g")
           ;"get" data from scope
           Sleep(5000)
```

```
        WinActivate("OpenChoice Desktop")
        WinWaitActive("OpenChoice Desktop")
        Send("^s")
        WinWaitActive("Save As")
        Sleep(1000)
        Send($j & "mm_" & $svar & $i)
        Sleep(1000)
        ControlClick("Save As", "", "[CLASS:Button; INSTANCE:2]")
        Sleep(5000)
        ;save data from scope
  Next
$j = $j + 10
Until $j = $k + 10
;move lens as per j and k above
```

AutoIt code to save spectra from bitmap image and paste pixel/intensity values to Excel file

```
$svar = "Spectra"
;name of imajeJ stack
$svar1 = " (75%)"
;window size
$svar2 = "Microsoft Excel - AN fluence spectra"
;Name of excel workbook
$svar5 = "70"
;number of images in stack

WinActivate($svar & $svar1)
Sleep(0500)
WinWaitActive($svar & $svar1)
Sleep(1000)
WinActivate("ImageJ")
Sleep(0500)
WinWaitActive("ImageJ")
Sleep(2500)
Send("{ALTDOWN}")
Sleep(0050)
SEND("{ALTUP}")
Sleep(0050)
Send("{RIGHT}")
Sleep(0050)
Send("{DOWN 12}")
Sleep(0050)
Send("{RIGHT}")
Sleep(0050)
Send("{DOWN 16}")
Sleep(0050)
Send("{ENTER}")
;pointing to: edit>selection>specify
Sleep(1000)
Send("1280")
Sleep(0500)
Send("{TAB}")
Send("43")
Sleep(0500)
Send("{TAB}")
Send("0")
Sleep(0500)
Send("{TAB}")
Send("469")
Sleep(0500)
Send("{ENTER}")
```

```
  Sleep(1000)
  ;defined region of interest

  For $i = 1 To $svar5
  Sleep (0500)
  Send("^k")
  ;plot profile
  WinActivate("Plot of " & $svar)
  WinWaitActive("Plot of " & $svar)
  Sleep(0500)
  ControlClick("Plot of " & $svar,"",3)
  Send("{Space}")
  Sleep(0500)
  ;copy intensity at pixel values
  WinActivate($svar2)
  WinWaitActive($svar2)
  Send("^v")
  ;paste values into excel file
  Sleep(0500)
  Send("{RIGHT}")
  Send("{RIGHT}")
  WinClose("Plot of " & $svar)
  WinActivate($svar & $svar1)
  WinWaitActive($svar & $svar1)
  Send("+{RIGHT}")
  ;next image to save spectra and copy to excel
Next
```

Motion control code for 70 shots spread out at nominal distance on 2” wafer

```
#WAFER2

PAY=0;
PAZ=0;
BGY;
BGZ;
AMY;
AMZ;
PRZ=2000;
PRY=-4000;
BGY;
BGZ;
AI-5;
AMY;
AMZ;
PAY=0;
PAZ=0;
BGY;
BGZ;
AMY;
AMZ;

#MOVE1
i=0;
#LOOP1;
PRY=-2000;
AI-5;
BG Y;
AM Y;
i= i+1;
JP #LOOP1,i<5;
PRZ=-4000;
BGZ;
MG "Line 1 complete";

#MOVE2
i=0;
#LOOP2;
AMY;
AMZ;
PRY=2000;
AI-5;
BG Y;
AM Y;
```

```
i= i+1;
JP #LOOP2,i<7;
PRZ=-4000;
BGZ;
MG "Line 2 complete";

#MOVE3
i=0;
#LOOP3;
AMY;
AMZ;
PRY=-2000;
AI-5;
BG Y;
AM Y;
i= i+1;
JP #LOOP3,i<9;
PRZ=-4000;
PRY=2000;
BGZ;
BGY;
MG "Line 3 complete";

#MOVE4
i=0;
#LOOP4;
AMY;
AMZ;
PRY=2000;
AI-5;
BG Y;
AM Y;
i= i+1;
JP #LOOP4,i<9;
PRZ=-4000;
PRY=-2000;
BGY;
BGZ;
MG "Line 4 complete";

#MOVE5
i=0;
#LOOP5;
AMY;
AMZ;
PRY=-2000;
```

```
AI-5;
BG Y;
AM Y;
i= i+1;
JP #LOOP5,i<9;
PRZ=-4000;
PRY=2000;
BGY;
BGZ;
MG "Line 5 complete";

#MOVE6
i=0;
#LOOP6;
AMY;
AMZ;
PRY=2000;
AI-5;
BG Y;
AM Y;
i= i+1;
JP #LOOP6,i<9;
PRY=-2000;
PRZ=-4000;
BGY;
BGZ;
MG "Line 6 complete";

#MOVE7
i=0;
#LOOP7;
AMY;
AMZ;
PRY=-2000;
AI-5;
BG Y;
AM Y;
i= i+1;
JP #LOOP7,i<9;
PRY=4000;
PRZ=-4000;
BGY;
BGZ;
MG "Line 7 complete";

#MOVE8
```

```
i=0;
#LOOP8;
AMY;
AMZ;
PRY=2000;
AI-5;
BG Y;
AM Y;
i= i+1;
JP #LOOP8,i<7;
PRY=-4000;
PRZ=-4000;
BGY;
BGZ;
MG "Line 8 complete";

#MOVE9
i=0;
#LOOP9;
AMY;
AMZ;
PRY=-2000;
AI-5;
BG Y;
AM Y;
i= i+1;
JP #LOOP9,i<5;
MG "Line 9 complete";



MG "Wafer Complete";

EN;
```

Motion control code for spraying a 2” wafer with 10mL of RDX

#SPRAY2
PAY=0; BGY; AMY; WT 55.6;
PAY=40; BGY; AMY; WT 1111.6;
PAY=80; BGY; AMY; WT 2223.2;
PAY=120; BGY; AMY; WT 3334.9;
PAY=160; BGY; AMY; WT 4446.5;
PAY=200; BGY; AMY; WT 5558.1;
PAY=240; BGY; AMY; WT 6669.7;
PAY=280; BGY; AMY; WT 7781.4;
PAY=320; BGY; AMY; WT 8893;
PAY=360; BGY; AMY; WT 10004.6;
PAY=400; BGY; AMY; WT 11116.2;
PAY=440; BGY; AMY; WT 12227.9;
PAY=480; BGY; AMY; WT 13339.5;
PAY=520; BGY; AMY; WT 14451.1;
PAY=560; BGY; AMY; WT 15562.7;
PAY=600; BGY; AMY; WT 16674.4;
PAY=640; BGY; AMY; WT 17786;
PAY=680; BGY; AMY; WT 18897.6;
PAY=720; BGY; AMY; WT 20009.2;
PAY=760; BGY; AMY; WT 21120.9;
PAY=800; BGY; AMY; WT 22232.5;
PAY=840; BGY; AMY; WT 23344.1;
PAY=880; BGY; AMY; WT 24455.7;
PAY=920; BGY; AMY; WT 25567.4;
PAY=960; BGY; AMY; WT 26679;
PAY=1000; BGY; AMY; WT 27790.6;
PAY=1040; BGY; AMY; WT 28902.2;
PAY=1080; BGY; AMY; WT 30013.8;
PAY=1120; BGY; AMY; WT 31125.5;
PAY=1160; BGY; AMY; WT 32237.1;
PAY=1200; BGY; AMY; WT 33348.7;
PAY=1240; BGY; AMY; WT 34460.3;
PAY=1280; BGY; AMY; WT 35572;
PAY=1320; BGY; AMY; WT 36683.6;
PAY=1360; BGY; AMY; WT 37795.2;
PAY=1400; BGY; AMY; WT 38906.8;
PAY=1440; BGY; AMY; WT 40018.5;
PAY=1480; BGY; AMY; WT 41130.1;
PAY=1520; BGY; AMY; WT 42241.7;
PAY=1560; BGY; AMY; WT 43353.3;
PAY=1600; BGY; AMY; WT 44465;
PAY=1640; BGY; AMY; WT 45576.6;
PAY=1680; BGY; AMY; WT 46688.2;

PAY=1720; BGY; AMY; WT 47799.8;
PAY=1760; BGY; AMY; WT 48911.5;
PAY=1800; BGY; AMY; WT 50023.1;
PAY=1840; BGY; AMY; WT 51134.7;
PAY=1880; BGY; AMY; WT 52246.3;
PAY=1920; BGY; AMY; WT 53358;
PAY=1960; BGY; AMY; WT 54469.6;
PAY=2000; BGY; AMY; WT 55581.2;
PAY=2040; BGY; AMY; WT 56692.8;
PAY=2080; BGY; AMY; WT 57804.4;
PAY=2120; BGY; AMY; WT 58916.1;
PAY=2160; BGY; AMY; WT 60027.7;
PAY=2200; BGY; AMY; WT 61139.3;
PAY=2240; BGY; AMY; WT 62250.9;
PAY=2280; BGY; AMY; WT 63362.6;
PAY=2320; BGY; AMY; WT 64474.2;
PAY=2360; BGY; AMY; WT 65585.8;
PAY=2400; BGY; AMY; WT 66697.4;
PAY=2440; BGY; AMY; WT 67809.1;
PAY=2480; BGY; AMY; WT 68920.7;
PAY=2520; BGY; AMY; WT 70032.3;
PAY=2560; BGY; AMY; WT 71143.9;
PAY=2600; BGY; AMY; WT 72255.6;
PAY=2640; BGY; AMY; WT 73367.2;
PAY=2680; BGY; AMY; WT 74478.8;
PAY=2720; BGY; AMY; WT 75590.4;
PAY=2760; BGY; AMY; WT 76702.1;
PAY=2800; BGY; AMY; WT 77813.7;
PAY=2840; BGY; AMY; WT 78925.3;
PAY=2880; BGY; AMY; WT 80036.9;
PAY=2920; BGY; AMY; WT 81148.6;
PAY=2960; BGY; AMY; WT 82260.2;
PAY=3000; BGY; AMY; WT 83371.8;
PAY=3040; BGY; AMY; WT 84483.4;
PAY=3080; BGY; AMY; WT 85595.1;
PAY=3120; BGY; AMY; WT 86706.7;
PAY=3160; BGY; AMY; WT 87818.3;
PAY=3200; BGY; AMY; WT 88929.9;
PAY=3240; BGY; AMY; WT 90041.5;
PAY=3280; BGY; AMY; WT 91153.2;
PAY=3320; BGY; AMY; WT 92264.8;
PAY=3360; BGY; AMY; WT 93376.4;
PAY=3400; BGY; AMY; WT 94488;
PAY=3440; BGY; AMY; WT 95599.7;
PAY=3480; BGY; AMY; WT 96711.3;
PAY=3520; BGY; AMY; WT 97822.9;

PAY=3560; BGY; AMY; WT 98934.5;
PAY=3600; BGY; AMY; WT 100046.2;
PAY=3640; BGY; AMY; WT 101157.8;
PAY=3680; BGY; AMY; WT 102269.4;
PAY=3720; BGY; AMY; WT 103381;
PAY=3760; BGY; AMY; WT 104492.7;
PAY=3800; BGY; AMY; WT 105604.3;
PAY=3840; BGY; AMY; WT 106715.9;
PAY=3880; BGY; AMY; WT 107827.5;
PAY=3920; BGY; AMY; WT 108939.2;
PAY=3960; BGY; AMY; WT 110050.8;
PAY=4000; BGY; AMY; WT 111162.4;
PAY=4040; BGY; AMY; WT 112274;
PAY=4080; BGY; AMY; WT 113385.7;
PAY=4120; BGY; AMY; WT 114497.3;
PAY=4160; BGY; AMY; WT 115608.9;
PAY=4200; BGY; AMY; WT 116720.5;
PAY=4240; BGY; AMY; WT 117832.1;
PAY=4280; BGY; AMY; WT 118943.8;
PAY=4320; BGY; AMY; WT 120055.4;
PAY=4360; BGY; AMY; WT 121167;
PAY=4400; BGY; AMY; WT 122278.6;
PAY=4440; BGY; AMY; WT 123390.3;
PAY=4480; BGY; AMY; WT 124501.9;
PAY=4520; BGY; AMY; WT 125613.5;
PAY=4560; BGY; AMY; WT 126725.1;
PAY=4600; BGY; AMY; WT 127836.8;
PAY=4640; BGY; AMY; WT 128948.4;
PAY=4680; BGY; AMY; WT 130060;
PAY=4720; BGY; AMY; WT 131171.6;
PAY=4760; BGY; AMY; WT 132283.3;
PAY=4800; BGY; AMY; WT 133394.9;
PAY=4840; BGY; AMY; WT 134506.5;
PAY=4880; BGY; AMY; WT 135618.1;
PAY=4920; BGY; AMY; WT 136729.8;
PAY=4960; BGY; AMY; WT 137841.4;
PAY=5000; BGY; AMY; WT 138953;
PAY=5040; BGY; AMY; WT 140064.6;
PAY=5080; BGY; AMY; WT 141176.3;
PAY=5120; BGY; AMY; WT 142287.9;
PAY=5160; BGY; AMY; WT 143399.5;
PAY=5200; BGY; AMY; WT 144511.1;
PAY=5240; BGY; AMY; WT 145622.7;
PAY=5280; BGY; AMY; WT 146734.4;
PAY=5320; BGY; AMY; WT 147846;
PAY=5360; BGY; AMY; WT 148957.6;

PAY=5400; BGY; AMY; WT 150069.2;
PAY=5440; BGY; AMY; WT 151180.9;
PAY=5480; BGY; AMY; WT 152292.5;
PAY=5520; BGY; AMY; WT 153404.1;
PAY=5560; BGY; AMY; WT 154515.7;
PAY=5600; BGY; AMY; WT 155627.4;
PAY=5640; BGY; AMY; WT 156739;
PAY=5680; BGY; AMY; WT 157850.6;
PAY=5720; BGY; AMY; WT 158962.2;
PAY=5760; BGY; AMY; WT 160073.9;
PAY=5800; BGY; AMY; WT 161185.5;
PAY=5840; BGY; AMY; WT 162297.1;
PAY=5880; BGY; AMY; WT 163408.7;
PAY=5920; BGY; AMY; WT 164520.4;
PAY=5960; BGY; AMY; WT 165632;
PAY=6000; BGY; AMY; WT 166743.6;
PAY=6040; BGY; AMY; WT 167855.2;
PAY=6080; BGY; AMY; WT 168966.9;
PAY=6120; BGY; AMY; WT 170078.5;
PAY=6160; BGY; AMY; WT 171190.1;
PAY=6200; BGY; AMY; WT 172301.7;
PAY=6240; BGY; AMY; WT 173413.3;
PAY=6280; BGY; AMY; WT 174525;
PAY=6320; BGY; AMY; WT 175636.6;
PAY=6360; BGY; AMY; WT 176748.2;
PAY=6400; BGY; AMY; WT 177859.8;
PAY=6440; BGY; AMY; WT 178971.5;
PAY=6480; BGY; AMY; WT 180083.1;
PAY=6520; BGY; AMY; WT 181194.7;
PAY=6560; BGY; AMY; WT 182306.3;
PAY=6600; BGY; AMY; WT 183418;
PAY=6640; BGY; AMY; WT 184529.6;
PAY=6680; BGY; AMY; WT 185641.2;
PAY=6720; BGY; AMY; WT 186752.8;
PAY=6760; BGY; AMY; WT 187864.5;
PAY=6800; BGY; AMY; WT 188976.1;
PAY=6840; BGY; AMY; WT 190087.7;
PAY=6880; BGY; AMY; WT 191199.3;
PAY=6920; BGY; AMY; WT 192311;
PAY=6960; BGY; AMY; WT 193422.6;
PAY=7000; BGY; AMY; WT 194534.2;
PAY=7040; BGY; AMY; WT 195645.8;
PAY=7080; BGY; AMY; WT 196757.5;
PAY=7120; BGY; AMY; WT 197869.1;
PAY=7160; BGY; AMY; WT 198980.7;
PAY=7200; BGY; AMY; WT 200092.3;

PAY=7240; BGY; AMY; WT 201204;
PAY=7280; BGY; AMY; WT 202315.6;
PAY=7320; BGY; AMY; WT 203427.2;
PAY=7360; BGY; AMY; WT 204538.8;
PAY=7400; BGY; AMY; WT 205650.4;
PAY=7440; BGY; AMY; WT 206762.1;
PAY=7480; BGY; AMY; WT 207873.7;
PAY=7520; BGY; AMY; WT 208985.3;
PAY=7560; BGY; AMY; WT 210096.9;
PAY=7600; BGY; AMY; WT 211208.6;
PAY=7640; BGY; AMY; WT 212320.2;
PAY=7680; BGY; AMY; WT 213431.8;
PAY=7720; BGY; AMY; WT 214543.4;
PAY=7760; BGY; AMY; WT 215655.1;
PAY=7800; BGY; AMY; WT 216766.7;
PAY=7840; BGY; AMY; WT 217878.3;
PAY=7880; BGY; AMY; WT 218989.9;
PAY=7920; BGY; AMY; WT 220101.6;
PAY=7960; BGY; AMY; WT 221213.2;
PAY=8000; BGY; AMY; WT 222324.8;
PAY=8040; BGY; AMY; WT 223436.4;
PAY=8080; BGY; AMY; WT 224548.1;
PAY=8120; BGY; AMY; WT 225659.7;
PAY=8160; BGY; AMY; WT 226771.3;
PAY=8200; BGY; AMY; WT 227882.9;
PAY=8240; BGY; AMY; WT 228994.6;
PAY=8280; BGY; AMY; WT 230106.2;
PAY=8320; BGY; AMY; WT 231217.8;
PAY=8360; BGY; AMY; WT 232329.4;
PAY=8400; BGY; AMY; WT 233441;
PAY=8440; BGY; AMY; WT 234552.7;
PAY=8480; BGY; AMY; WT 235664.3;
PAY=8520; BGY; AMY; WT 236775.9;
PAY=8560; BGY; AMY; WT 237887.5;
PAY=8600; BGY; AMY; WT 238999.2;
PAY=8640; BGY; AMY; WT 240110.8;
PAY=8680; BGY; AMY; WT 241222.4;
PAY=8720; BGY; AMY; WT 242334;
PAY=8760; BGY; AMY; WT 243445.7;
PAY=8800; BGY; AMY; WT 244557.3;
PAY=8840; BGY; AMY; WT 245668.9;
PAY=8880; BGY; AMY; WT 246780.5;
PAY=8920; BGY; AMY; WT 247892.2;
PAY=8960; BGY; AMY; WT 249003.8;
PAY=9000; BGY; AMY; WT 250115.4;
PAY=9040; BGY; AMY; WT 251227;

PAY=9080; BGY; AMY; WT 252338.7;
PAY=9120; BGY; AMY; WT 253450.3;
PAY=9160; BGY; AMY; WT 254561.9;
PAY=9200; BGY; AMY; WT 255673.5;
PAY=9240; BGY; AMY; WT 256785.2;
PAY=9280; BGY; AMY; WT 257896.8;
PAY=9320; BGY; AMY; WT 259008.4;
PAY=9360; BGY; AMY; WT 260120;
PAY=9400; BGY; AMY; WT 261231.6;
PAY=9440; BGY; AMY; WT 262343.3;
PAY=9480; BGY; AMY; WT 263454.9;
PAY=9520; BGY; AMY; WT 264566.5;
PAY=9560; BGY; AMY; WT 265678.1;
PAY=9600; BGY; AMY; WT 266789.8;
PAY=9640; BGY; AMY; WT 267901.4;
PAY=9680; BGY; AMY; WT 269013;
PAY=9720; BGY; AMY; WT 270124.6;
PAY=9760; BGY; AMY; WT 271236.3;
PAY=9800; BGY; AMY; WT 272347.9;
PAY=9840; BGY; AMY; WT 273459.5;
PAY=9880; BGY; AMY; WT 274571.1;
PAY=9920; BGY; AMY; WT 275682.8;
PAY=9960; BGY; AMY; WT 276794.4;
PAY=10000; BGY; AMY; WT 277906;
PAY=10040; BGY; AMY; WT 279017.6;
PAY=10080; BGY; AMY; WT 280129.3;
PAY=10120; BGY; AMY; WT 281240.9;
PAY=10160; BGY; AMY; WT 282352.5;